HIGH ENERGY EMISSION FROM "DEAD" STARS

by

Pavan R. Hebbar

A thesis submitted in partial fulfillment of the requirements for the degree of

Master of Science

Department of Physics

University of Alberta

Abstract

Massive stars end their life through explosive supernovae, leaving behind supernova remnants (SNRs) and forming neutron stars (NSs) or black holes (BHs). Studying the X-rays emitted from BHs, NSs, and SNRs allows us to investigate the high energy processes producing this radiation. However, challenges because of low photon counts, the response of instruments and background radiation can lead to confusion in the analysis. In this thesis, I investigate the X-ray emission of four systems using the *Chandra X-ray Observatory* to determine the properties of each system. I use two *Chandra* observations of an eclipsing binary millisecond pulsar, 47 Tuc W, to check the continued presence of dips in the X-ray light curve. I show that higher energy X-rays show a more prominent dip in the light curve, explaining the failure to detect eclipses in a data set taken with a detector sensitive principally to low-energy X-rays. Through the analysis of candidate active galactic nuclei (AGN) in two dwarf bulgeless galaxies, Henize 2-10 and NGC 4178, I introduce a novel method to identify which candidate AGN are likely young SNRs. I also provide evidence for a NS in SNR 1E 0102.2-7219, and model its X-ray spectrum to constrain its properties and determine the type of NS.

Preface

This thesis is an original work by Pavan R. Hebbar under the supervision of Prof. Craig O. Heinke. All data used are publicly available.

In Chapter 2 (to be submitted to MNRAS), I analyzed the X-ray light curves and X-ray spectra to establish the presence of a variable hard X-ray source and a constant soft source, with the guidance of Prof. Craig O. Heinke. D. Kandel and Prof. Roger W. Romani modelled the intra-binary shock (IBS) in the eclipsing binary system using a module developed by Romani and Sanchez (2016), Sanchez and Romani (2017), and Kandel et al. (2019) in ICARUS software (Breton et al. 2013).

I have published the content of Chapter 3 in Hebbar et al. (2019). I reduced the *Chandra* observations and analyzed the data. Co-authors Craig O. Heinke, Gregory R. Sivakoff and Aarran W. Shaw helped me interpret the statistical significance of the results and their theoretical implications.

In Chapter 4 (submitted to MNRAS), I reduced the *Chandra* data and modelled the X-ray spectra of the compact object. Prof. Wynn C. G. Ho provided the neutron star cooling curves to compare with the luminosity and age of our NS. Prof. Craig O. Heinke and Prof. Wynn C. G. Ho also assisted me in understanding the physical relevance of the spectral fits and the high thermal luminosity of our neutron star.

"In some strange way, any new fact or insight that I may have found has not seemed to me as a 'discovery' of mine, but rather something that had always been there and that I had chanced to pick up."

Subrahmanyan Chandrashekar

Acknowledgements

I am incredibly grateful to Prof. Craig O. Heinke for his continuous guidance and support, without which this thesis wouldn't be possible. I am also thankful to Prof. Gregory R. Sivakoff and Dr. Aarran W. Shaw for assisting me in analyzing the data and giving a deeper conceptual understanding of the results. I would also like to thank fellow graduate students working under Prof. Heinke — Yue Zhao and Asma Hattawi for their constant support throughout my master's program. I am also grateful to the other members of the University of Alberta astrophysics group for helping me get a broader knowledge in astrophysics and understand the implication of my research on other sub-fields in astrophysics.

Contents

List of Tables

List of Figures

Acronyms

AGN	Active Galactic Nucleus.
BB	Black Body.
ACIS	Advanced CCD Imaging Spectrometer.
AIC	Akaike Information Criterion.
AICc	Akaike Information Criterion with correction.
APR	Akmal, Pandharipande, and Ravenhall.
ARF	Auxiliary Response Function.
ATNF	Australia Telescope National Facility.
BH	Black Hole.
CALDB	CALibration DataBase.
CCD	Charge-Coupled Device.
CCO	Central Compact Object.
ChaSeR	Chandra Search and Retrieval.
CIAO	Chandra Interactive Analysis of Observations.
CIE	Collisional Ionization Equilibrium.
CvM	Cramér-von-Mises.
CXO	Chandra X-ray Observatory.
d.o.f	Degrees Of Freedom.

EDSER Energy Dependent Subpixel Event Repositioning.

FWHM Full Width at Half Maximum.

GC Globular Cluster.

HETG High Energy Transmission Grating.
HMXB High Mass X-ray Binary.
HRC High Resolution Camera.
HRMA High Resolution Mirror Assembly.
HST Hubble Space Telescope.

IBS Intra-Binary Shock.
IC Inverse Compton.
IMBH Intermediate Mass Black Hole.

LETG Low Energy Transmission Grating.
LMXB Low Mass X-ray Binary.

MJD Modified Julian Date.
MSP Milli-Second Pulsar.

NEI Non-Equilibrium Ionization.
NS Neutron Star.

PHA Pulse Height Amplitude.
PIMMS Portable, Interactive Multi-Mission Simulator.

PL Power-Law.

PSD Power Spectral Density.

RMF Response Matrix Function.

SMBH Super-Massive Black Hole.

SMC Small Magellanic Clouds.

SNR SuperNova Remnant.

SSC Synchrotron Self Compton.

TE Timed Exposure.

UV Ultra-Violet.

WISE Wide-field Infrared Survey Explorer.

Chapter 1

Introduction

Since the birth of X-ray astronomy with the detection of Scorpius X-1 (Giacconi et al. 1962), we have come a long way in understanding the X-ray sky (see Santangelo and Madonia 2014, for a broad review). Today, X-ray observatories such as *Chandra* (Weisskopf et al. 2000), *XMM-Newton* (Jansen et al. 2001), *NuSTAR* (Harrison et al. 2013), and *Swift* (Burrows et al. 2004) allow us to study the entire range of X-ray energies ($0.1 - 100$ keV) with great spectral, temporal and angular resolution (see Paerels and Kahn 2003, for example). Explaining the physical processes that emit in high energies has given us considerable insights into the properties of neutron stars (NSs), black holes (BHs), supernova remnants (SNRs), active stars, and many other sources.

However, X-ray astronomy faces several challenges. The high energy of individual photons and the smaller effective areas of X-ray observatories (with respect to the optical) lead to low photon count rates even for moderately bright sources. The Poisson noise (Poisson 1837) due to the lower number of photons coupled with the response of detectors and the background radiation (both astrophysical and instrument noise) can lead to incorrect modelling of the radiative phenomenon. Thus, it is important to study these effects that affect the quality of the data, and understand the X-ray emitting mechanisms, to properly interpret the X-ray observations.

1.1 X-ray emission processes

Acceleration of charged particles can produce electromagnetic radiation across all frequencies (Thomson 1881; Larmor 1897). Here, I give a brief overview of a few mechanisms that produce radiation that are relevant to this thesis (refer to Rybicki and Lightman 1986; Ghisellini 2013; Bradt 2014, etc. for details), placing an emphasis on their broadband spectra.

1.1.1 Thermal bremsstrahlung radiation

Derived from the German word *bremsstrahlung* meaning "braking", this radiation is produced due to the deceleration of electrons by ions. The Coulomb collisions are free-free in this case, i.e. the positive ions do not capture the electrons. Assuming that the plasma is isothermal, the electrons are non-relativistic (relativistic corrections are required for $kT \gtrsim m_e c^2$) and follow Maxwell-Boltzmann distribution (Maxwell 1860a,b; Boltzmann 1872; note that non-thermal distibution of electrons can also produce bremsstrahlung emission, but I do not consider it in this text), and the emitted photons aren't self-absorbed (self-absorption of the radiation is important when the brightness temperature $T_b (= c^2 I_\nu / 2k\nu^2)$ tends towards the electron temperature T_e), the specific intensity,

$$I_\nu(\nu, T) \propto \frac{e^{-h\nu/kT}}{T^{1/2}} \int_0^R n_e n_i \mathrm{d}r \quad \mathrm{ergs\,cm^{-2}\,s^{-1}\,Hz^{-1}\,sr^{-1}}, \tag{1.1}$$

where the integration is over line-of-sight thickness of the plasma. For point sources, we integrate Eq. 1.1 over the solid angle subtended by the source to get the spectral flux density,

$$S_\nu(\nu, T) \propto \frac{e^{-h\nu/kT}}{r^2 T^{1/2}} \int_V n_e n_i \mathrm{d}V \quad \mathrm{ergs\,cm^{-2}\,s^{-1}\,Hz^{-1}}, \tag{1.2}$$

if distance to the source to be much larger than its thickness. The quantity $\int_V n_e n_i \mathrm{d}V$ is called the emission measure.

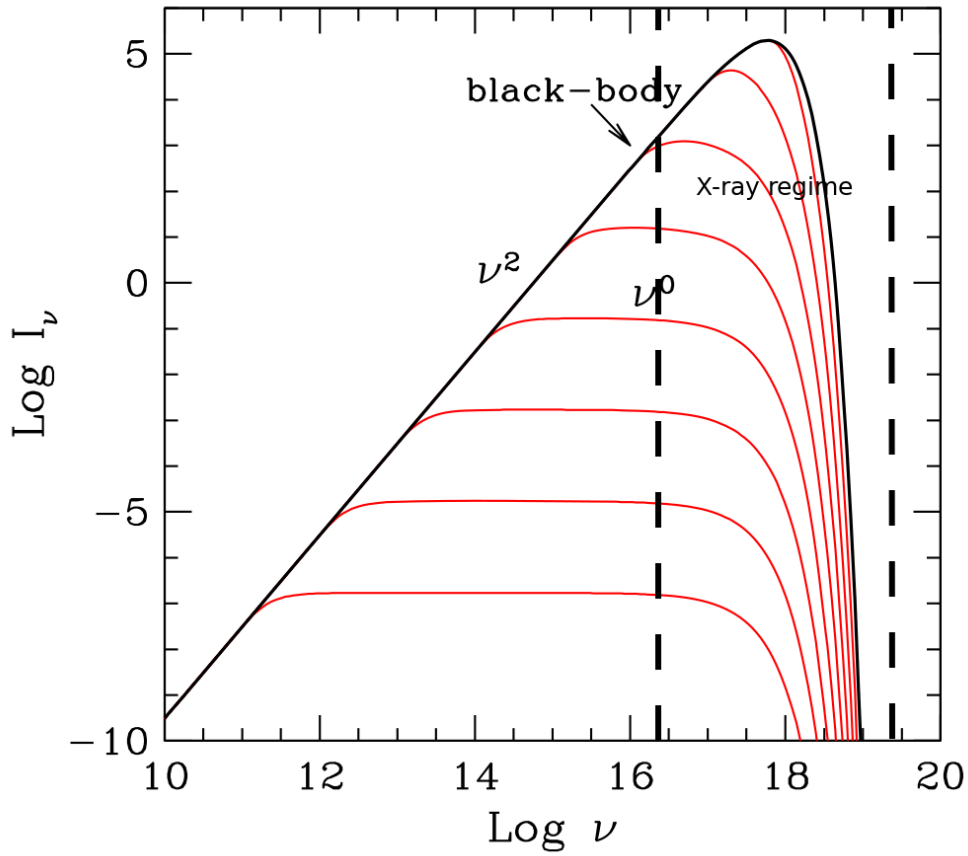

Figure 1.1: Bremsstrahlung intensity (red) of a plasma of temperature, $T = 10^7$ K and thickness, $R = 10^{15}$ cm. The number density of electrons and ions are gradually increased from 10^{10} cm^{-3} to 10^{17} cm^{-3} in factors of 10. Free-free self-absorption by the electrons in the plasma results in the low-energy cut-off. We do not include the effects of Gaunt factor, $g_{\rm ff}$. Including $g_{\rm ff}$ will lead to a gradual increase towards the lower energies. Image credit: Ghisellini (2013).

1.1.2 Blackbody radiation

Blackbody (BB) radiation, one of the most prevalent radiative mechanism in astrophysics, is emitted by optically thick sources where the photons are in thermal equilibrium with the surrounding medium. The Planck function (Planck 1900; Planck and Masius 1914) gives the specific intensity of such a medium at temperature T as,

$$I_\nu(\nu, T) = \frac{2h\nu^3}{c^2} \frac{1}{e^{h\nu/kT} - 1} \quad [\mathrm{ergs\,cm^{-2}\,s^{-1}\,Hz^{-1}\,sr^{-1}}] \tag{1.3}$$

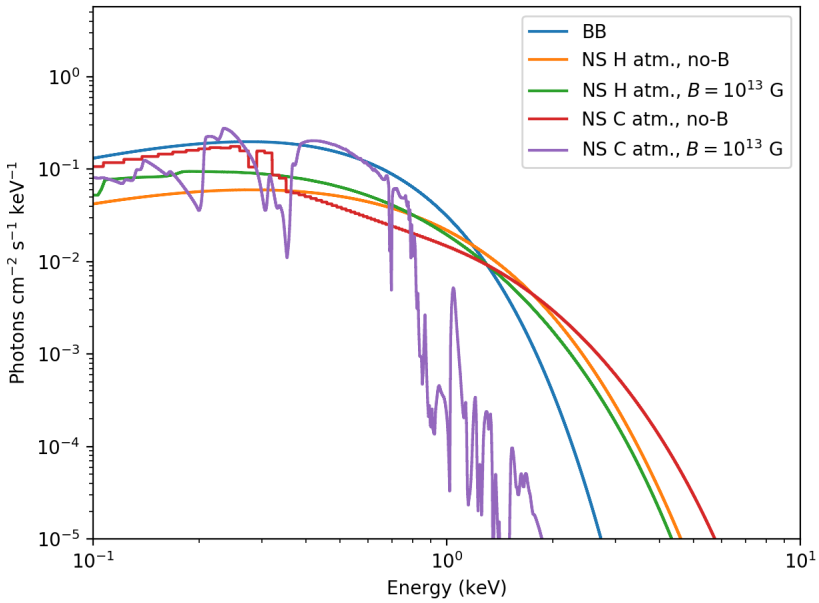

Figure 1.2: NS atmosphere models for a canonical NS with mass 1.4 $M_\odot$, radius 10 km and effective temperature 2×10^6 K emitting from its entire surface, at a distance of 1 kpc. XSPEC models `bbodyrad`, `nsatmos` (Heinke et al. 2006), `carbatm` (Suleimanov et al. 2014) and `nsmaxg` (Ho et al. 2008; Mori and Ho 2007) have been used to create spectra of non-magnetic hydrogen, carbon and magnetic atmospheres respectively. We see that NS H atmosphere emission are harder than BB emission and become softer with increasing magnetic fields. NS with carbon atmosphere shows prominent spectral features at $B = 10^{13}$ G.

The spectrum peaks at $h\nu = 2.82kT$. At higher frequencies ($h\nu >> kT$), Wein's approximation gives $I_\nu(\nu, T) \approx (2h\nu^3/c^2)e^{-h\nu/kT}$ (Wien 1897).

The above two radiative processes are referred to as "thermal" emission as they can be described by a single temperature and we assume the medium to be in thermal equilibrium. In general, as we add more particles to the optically thin thermal plasma, its emission approaches that of a BB (shown in Fig. 1.1).

1.1.3 Thermal emission from neutron stars

The observed thermal radiation from the NS are produced from the superficial layers of NS atmosphere which is ∼0.1–10 cm thick (refer Becker 2009; Potekhin et al. 2014, etc. for reviews). The state of the NS atmosphere depends on its

composition, temperature, surface gravity and magnetic field, thus effecting the properties of the emitted radiation.

Non-magnetic atmosphere models (applicable when $B \lesssim 10^9$ G) for hydrogen atmosphere) use the equations of hydrostatic and radiative equilibrium along with 1D radiative transfer equation and equation of state to solve for the properties of the atmosphere. Radiative opacities from free-free, bound-free, and bound-bound transitions and changing fractions of ions with temperature can lead to deviations from a simple BB spectra (Potekhin et al. 2014). In general we notice that emission from NS atmospheres is harder than BB (i.e NS atmospheres have a a power-law tail as compared to the exponential tail of BB), since the high energy radiation is from deeper and hotter layers. The spectra of heavy-element atmospheres also show spectral lines and photoionization edges (e.g. Ho and Heinke 2009; Suleimanov et al. 2014, etc.). Strong limb-darkening effects also need to be considered for a non-uniform NS surface.

Presence of magnetic fields effect the energy of bound states, polarize the radiation and produce electron and proton cyclotron lines. Vacuum polarization from high magnetic fields also suppresses the spectral features from bound species and affects the cyclotron lines thus leading to featureless spectra in magnetars. Magnetic atmospheres produces harder X-ray emission than BB but are softer than non-magnetic NS atmosphere emission (because opacities decrease more gradually with energy for magnetized plasma as compared to unmagnetized plasma). The radiation from magnetic NSs is strongly anisotropic. Check Fig. 1.2 for comparison of different NS atmosphere models with that of the BB emission at the same temperature and radius.

1.1.4 Non-thermal emission

Energetic processes like gamma-ray bursts (e.g. Kumar and Zhang 2015), active galactic nuclei (AGN; e.g. Padovani et al. 2017) and NS magnetospheres (Gaensler and Slane 2006; Kaspi et al. 2006; Li et al. 2008) can create a non-

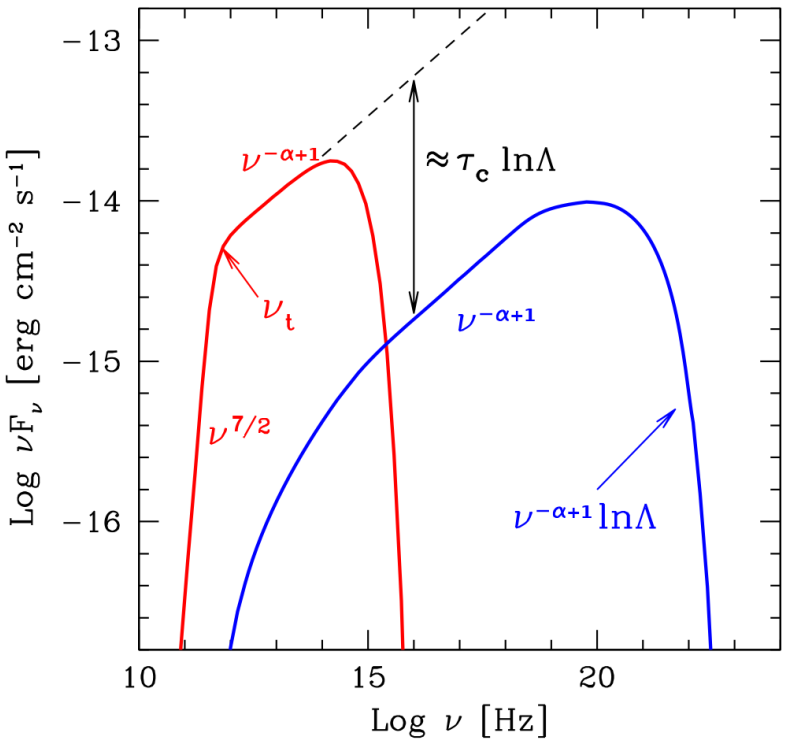

Figure 1.3: Broadband spectra of synchrotron and SSC radiation. Lower and higher energy cut-offs for synchrotron emission are set by scattering due to synchrotron self-absorption and IC effect. τ_c is the optical depth due to IC scattering. Λ is the ratio of minimum and maximum frequency of the seed photons that can be scattered to given energy. Synchrotron and SSC flux have the same slope in general. However seed photons cannot be excited to extremely high energies due to the limits on the energy of electrons. The Compton flux decreases at a steeper rate at these energies (i.e. Λ depends on maximum energy of the electron and ν). Image credit: Ghisellini (2013).

thermal distribution of electrons at relativistic energies. These electrons can cool through acceleration around magnetic fields (i.e. synchrotron radiation; Elder et al. 1947) or by getting scattered by a lower energy photon (inverse Compton (IC) effect; Compton 1923). Both these emissions can be characterized by a power-law model (i.e. $I_\nu \propto \nu^{-\alpha}$, where ν is the frequency of radiation and I_ν is the specific intensity i.e. flux per unit solid angle per unit frequency interval at frequency ν) if the underlying electron distribution is power-law with respect to energy (i.e. $n(E) \propto E^{-p}$; $\alpha = (p-1)/2$). The ratio of power radiated by synchrotron versus IC processes is equal to the ratio of the magnetic

to the photon energy density in the medium. Electrons in spinning NSs can also emit through coherent curvature radiation when they are guided along "curved" magnetic field lines (Radhakrishnan and Cooke 1969; Ruderman and Sutherland 1975, etc.). A particularly interesting case of non-thermal radiation is when the synchrotron emission of electrons produces seed photons that are accelerated to even higher energies through IC scattering. Fig. 1.3 shows such a self-synchrotron Compton (SSC) spectra along with the seed synchrotron spectra. The lower energy and higher energy cut-off for synchrotron radiation are due to self-absorption and IC scattering by electrons respectively. The decrease in SSC flux at higher energies is due to the limit on the maximum energy of the electron distribution. This results in a lower limit for the energy of the seed photons that can be scattered to the given higher energy value.

1.1.5 Line emission

Atoms, ions and molecules can collide to get excited/de-excited (bound-bound transitions), thus emitting/absorbing photons at discrete energies (Ångström 1853; Kirchhoff and Bunsen 1860). The ionization of atoms (bound-free) and capture of electrons by ions (free-bound transition) can also lead to absorption edges and recombination features corresponding to ionization energies of the atoms/ions (Moseley 1913, 1914). The density, temperature, and abundance of different elements in the plasma affect the strength of these features. If the population of the different states of ions and atoms does not change with time, the plasma is said to have reached collisional ionization equilibrium (CIE), else the plasma is said to be in non-equilibrium ionization (NEI). Fig. 1.4 shows the X-ray spectra of a 10^7 K plasma generated using PyAtomDB[1] package (Foster et al. 2012, this package has also been implemented in the XSPEC X-ray spectral analysis package through the models `apec, vapec and vvapec`).

[1] http://www.atomdb.org/index.php, https://atomdb.readthedocs.io/en/master

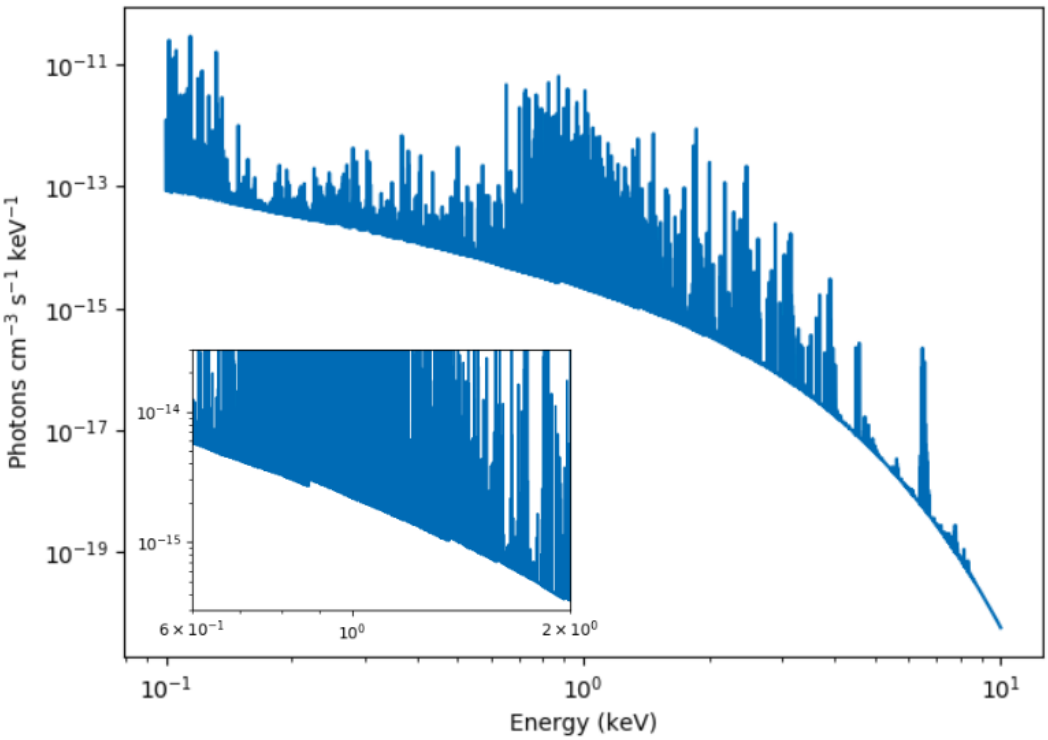

Figure 1.4: Spectra of plasma at temperature $T = 10^7$K and $n_e = 1$ cm^{-3} using Anders and Grevesse abundances for the elements, constructed using PyAtomDB. The inset between $0.6 - 2.0$ keV shows the recombination features of O VIII, Ne X and Mg XI (Verner et al. 1996).

1.2 *Chandra X-ray observatory*

The *Chandra X-ray Observatory* (CXO or *Chandra* for short)[2] is a flagship NASA mission that was launched on July 23, 1999. It has currently the highest angular resolution ($< 1''$) among all X-ray observatories (*The Chandra Proposers' Observatory Guide* 2018). *Chandra* hosts two X-ray detectors — Advanced CCD Imaging Spectrometer (ACIS; Garmire et al. 2003) and High Resolution Camera (HRC). In addition to these, there are two sets of grating spectrometers — High Energy Transmission Grating (HETG) sensitive to $0.4 - 10.0$ keV photons and Low Energy Transmission Grating (LETG) sensitive in the $0.07 - 0.2$ keV energy band. Use of gratings increases the spectral resolution ($E/\Delta E \sim 200 - 1000$) at

[2] http://cxc.harvard.edu/index.html

the expense of reduced effective area. The high angular resolution of *Chandra* and the ability to have a high spectral resolution in 0.1–10 keV has enabled detailed studies of compact objects in bright environments like globular clusters, centres of galaxies, SNRs, etc.

1.2.1 Advanced CCD imaging spectrometer

The ACIS instrument[3] consists of a set of ten 1024×1024 pixel charge coupled devices (CCDs) arranged in two configurations: four ACIS-I CCDs arranged as a 2×2 array and used for imaging; and six ACIS-S CCDs arranged in 6×1 array that can be used for imaging or readout of the grating instruments (HETG and LETG). Two of the CCDs (S1 and S3) in the ACIS-S are back-illuminated increasing their sensitivity to low energy photons with respect to the rest of the CCDs that are front-illuminated. Interaction with an X-ray photon liberates a proportional number of electrons from the pixel of the semiconductor chip. The charge of these electrons are collected for the interval of the frame time (3.2s, by default) and then transferred to the read-out electronics.

ACIS has an angular resolution $\sim 0\farcs492$ (limited by the pixel size, 24µm). Encircled energy plots show that 90% of the energy can be extracted from regions of $2''$ and $2\farcs5$ radii at 1.49 and 6.4 keV respectively. ACIS provides a spectral resolution of $\sim$ 100–200 eV depending on the energy of the X-ray photon (higher spectral resolution at lower energies). Fig. 1.5 shows the effective area plot of ACIS for an on-axis point source extracted with a $20''$-diameter region for *Chandra* Cycle 21. We see that currently the ACIS instrument is most responsive to X-ray photons of energies 0.6–10.0 keV. ACIS was sensitive to low energy X-ray photons down to 0.1 keV during its launch. However, the build-up of molecular contaminants on its optical blocking filter has led to the gradual degradation of the quantum efficiency of ACIS to low energy photons[4]. All the

[3] http://cxc.harvard.edu/proposer/POG/html/ACIS.html
[4] refer http://cxc.harvard.edu/ciao/why/acisqecontamN0010.html for details

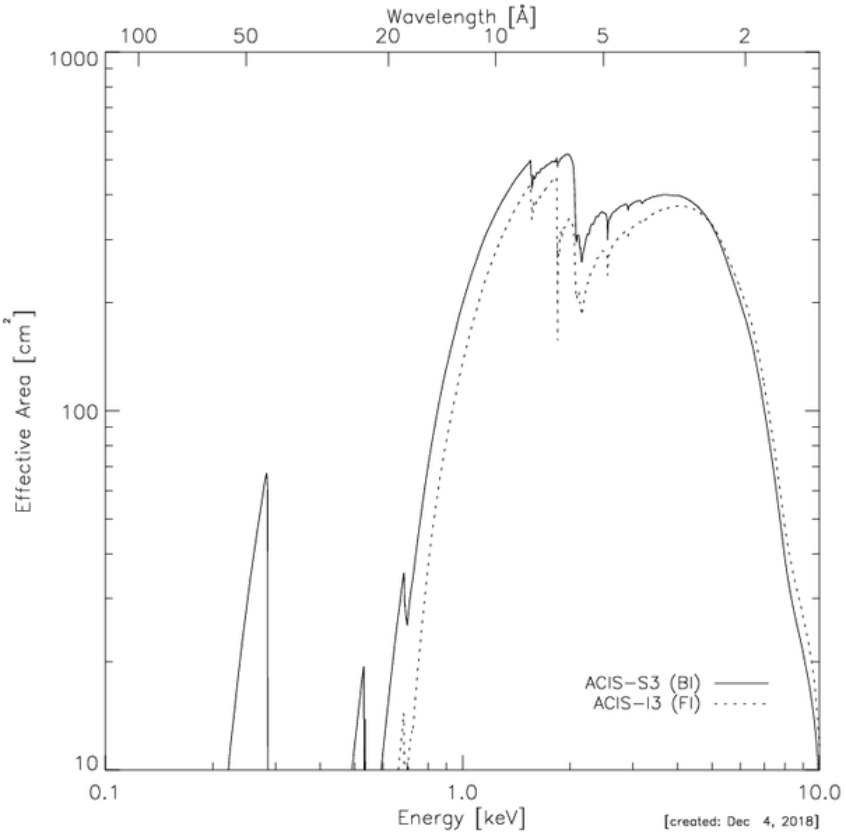

Figure 1.5: ACIS on-axis effective area for chips I3 and S3. We see that ACIS is most sensitive for X-ray photons of energies $0.6 - 10$ keV. This graph includes the response due to the *Chandra's* high resolution mirror assembly (HRMA) and the optical blocking filter on ACIS. Image Credit: *The Chandra Proposers' Observatory Guide* (2018).

observations used in this text were taken in the Timed Exposure (TE) mode, where the CCD collects data for a pre-decided frame time (3.2s by default) and then transfers the charge to the frame-store region where the data are read.

1.2.2 High resolution camera

The HRC[5] onboard *Chandra* is a micro-channel plate instrument and consists of two detectors: HRC-I (90mm $\times$ 90mm pair of plates), that provides a large field of view for imaging ($30' \times 30'$); largest among all *Chandra* instruments;

[5] http://cxc.harvard.edu/proposer/POG/html/chap7.html

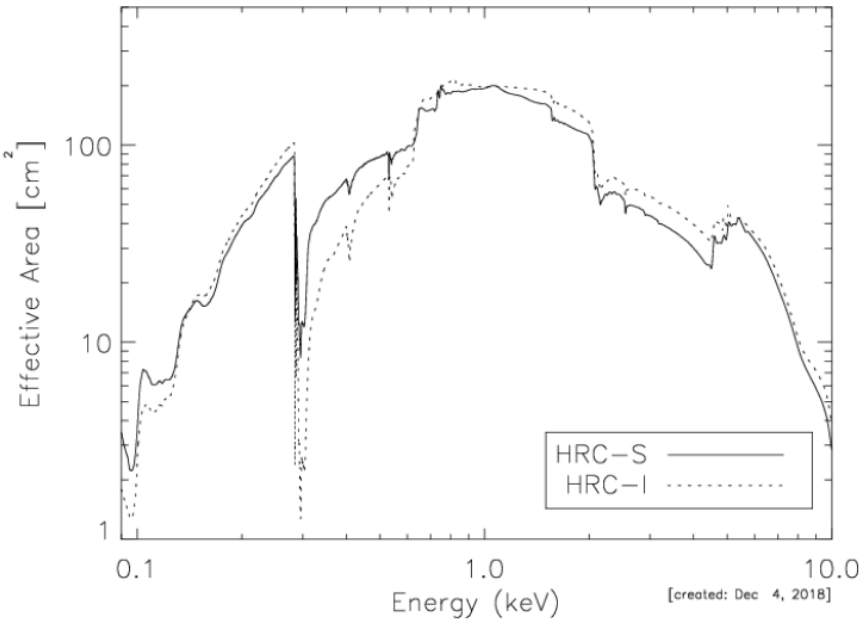

Figure 1.6: Effective area of HRC instrument with energy. HRC has a higher sensitivity to low energy photons as compared to ACIS but a lower total effective area. Image Credit: *The Chandra Proposers' Observatory Guide* (2018)

and HRC-S (three 100mm × 20mm pairs of plates), which can also be used as a readout of LETG spectra. Absorption of an X-ray photon emits electrons that are accelerated through the microchannel tubes creating a cascade of secondary electrons ($\sim 2 \times 10^7$ electrons for each photon detected) at the readout.

The intrinsic angular resolution of HRC (modelled by a Gaussian of $\sigma = 0.2''$) is well matched with that of the mirror assembly of *Chandra* and has a slightly better angular resolution than ACIS. HRC provides a timing resolution of 16µs. However, the spectral resolution of HRC is extremely poor and thus the HRC data cannot be used for spectral analysis unless the LETG has been used.

Fig. 1.6 shows the effective area of *Chandra* HRC. We see that HRC is more sensitive to photons of lower energies (< 0.1 keV) as compared to ACIS. The UV/ion shield does not contaminate the low energy response of HRC. However, the overall effective area of HRC is smaller than that of ACIS.

All the data collected by *Chandra* are publicly available after the proprietary period and can be accessed using the *Chandra* Search & Retrieval (ChaSeR)

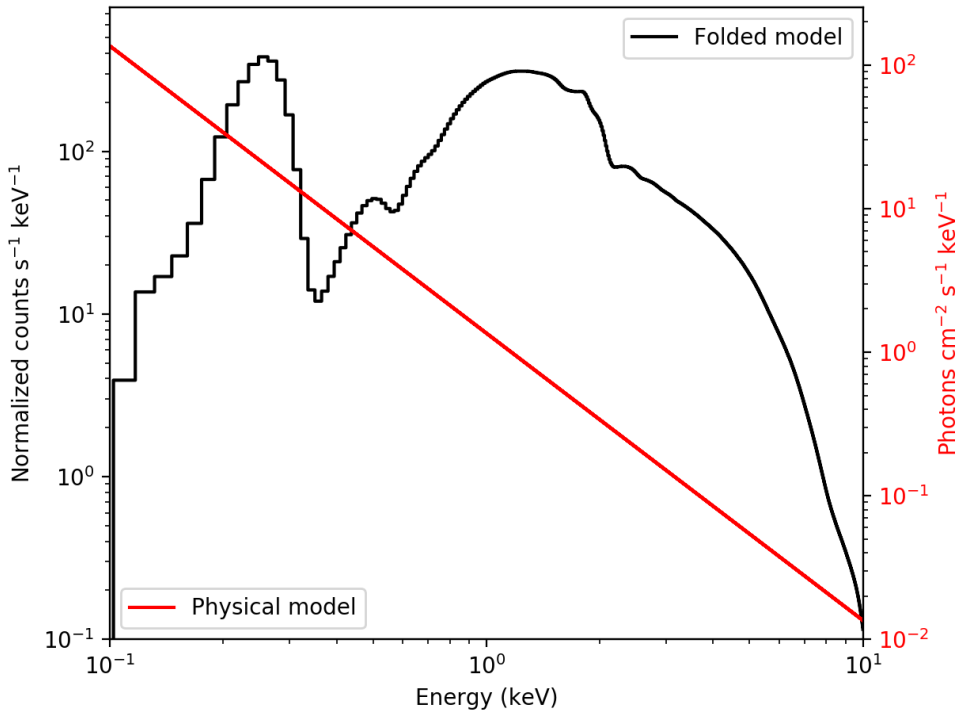

Figure 1.7: Power-law model ($N(E) = KE^{-\alpha}$) with index $\alpha = 2$ and a flux of 10^{-8} ergs cm^{-2} s^{-1} in the $0.1 - 10.0$ keV energy interval folded with the response of *Chandra* ACIS-S instrument (shown in black) provided by *Chandra* Cycle 21 Call for Proposals. The power-law model being used (unfolded) is shown in red and its values are indicated along the y-axis on the right.

tool[6]. The calibration files are updated regularly and released through CALDB[7]. The downloaded observations can be reprocessed and analyzed using the CIAO software[8] (Fruscione et al. 2006).

1.3 Physical interpretation of X-ray data

Raw X-ray data suffers from several artifacts including the point spread function of the mirror assembly and detector, changing effective area of the detector with energy, error in measuring the energy of photon, dead pixels within the CCD and

[6] https://cda.harvard.edu/chaser
[7] http://cxc.harvard.edu/caldb
[8] http://cxc.harvard.edu/ciao

inefficiencies in charge transfer etc. These effects are regularly monitored and updated in the calibration files of the mission. Once the data has been calibrated and reprocessed, understanding the physical process emitting X-rays might involve analyzing the changing flux with time (light-curve), energy (spectrum) and position (images). Common analysis techniques involve finding the physical model that best describes the observed data and estimating the best fitting parameters of this model.

Given that the X-ray images, light curves, and spectra are effected by the response of the detector used for the X-ray observation, it is important to include the properties of the detector while fitting the data. Standard X-ray analysis techniques use a forward modelling approach. In this method, the physical model is convolved with the detector response (folded model) before fitting it to the data (Fig. 1.7). For example, consider the analysis of observed X-ray spectrum. The number of counts per unit time in the i^{th} energy channel, m_i, as predicted by the physical model $f(E)$ (the number of photons per unit area per unit time per unit energy at energy E) is given by:

$$m_i = \int f(E) R_i(E) dE, \tag{1.4}$$

where $R_i(E)$ is the response of the detector i.e. effective area of the i^{th} channel times the probability that a photon of energy E will be detected in that channel.

1.4 Statistics for X-ray analysis

Fitting the data under the forward modelling approach involves perturbing the parameters of the physical model until the folded model best fits the observed X-ray data. Such analysis involved two stages – parameter estimation to determine the best fitting values of the parameters and goodness-of-fit test to determine if the best fitting physical model can actually explain the observed X-ray radiation.

Parameter estimation is achieved by maximizing the likelihood of generating

the observed data from the given model (likelihood function, L). The likelihood of a model with the given value of parameters denotes the probability of generating the observed data using the given model and parameter values i.e.

$$L(\theta|x) = f(x|\theta) \tag{1.5}$$

where x is the set of observed values, θ is the set of parmeter values and f is the joint probability distribution of generating each value in x with the given model and parameters. Commonly, we use statistics which consider $-2\ln L$ to get the best-fitting model. In order to estimate the confidence regions around the best-fitting parameters, we can fix a $\Delta_{\rm stat}$ (i.e. allowed change in the fitting statistics for the given confidence region; = 2.706 for 90% confidence region, if statistics are based on -2 ln L), and then calculate the region in the parameter space that gives the value of fitting statistic, $X < X_{\rm best} + \Delta_{\rm stat}$, where $X_{\rm best}$ is the value of fit statistic for the best fitting model. Complicated parameter spaces might require computationally expensive Monte-Carlo simulations for deriving the confidence regions.

Once we find the best-fitting model, we need to test whether this model is actually a good fit for the data i.e. if the best-fitting model can produce the observed data. For this purpose, we use a test statistic, T, and reject the null hypothesis that the data can be drawn from the model if $T > T_{\rm crit}$ (i.e. the null hypothesis probability is smaller than the allowed confidence). $T_{\rm crit}$ depends upon the confidence level set for rejecting the null hypothesis. Ideally, we wish the null hypothesis probability to only depend on $T_{\rm crit}$ and be independent of the model, so that one can generate tables relating the two quantities. However, if the null hypothesis probability also depends upon the model used, we need to perform goodness simulations that simulate the data given the model and evaluate the fraction of realizations that give $T < T_{\rm obs}$, where $T_{\rm obs}$ is the test statistic for the observed data. If this fraction is high (say 99%), the null

hypothesis can be rejected (with 99% confidence). Thus, it is important to understand the pros and cons of the statistical methods used for the parameter estimation and evaluating the goodness-of-fit.

1.4.1 χ^2-statistics

The χ^2-statistic (Pearson 1900) is twice the negative of the log-likelihood function for Gaussian data. It is defined as:

$$\chi^2 = \sum_i \frac{(y_i - m_i)^2}{\sigma_i^2}, \tag{1.6}$$

where y_i is the observed value and m_i is the model predicted value in the i^{th} data point, and σ_i is the expected standard deviation in the observed data. If there is no background, $\sigma_i^2 = y_i$ for data with Gaussian errors. For cases where the background needs to be considered, y_i is the net value after background subtraction and σ_i is the properly combined error from the source as well as the background.

For given values of the χ^2-statistic and number of degrees of (d.o.f, number of independently variable factors in the system – equal to number of data points - number of independent parameters in the model), the null hypothesis probability value is fixed, i.e. it is independent of the model used. Thus χ^2 can be used as a fit and test statistic, and is, therefore, the most widely used statistic in astronomy. However, the χ^2-statistic is only applicable to data following a Gaussian noise distribution; i.e., it cannot be used for faint sources with few counts per bin. Humphrey et al. (2009) showed that using χ^2 models to fit Poissonian data can give biased results even with high counts unless the number of bins is much smaller than $\sqrt{N}$, where N is the total number of events.

1.4.2 C-statistics

The Cash statistic, or C-statistic (Cash 1979), is twice the negative of the log-likelihood function for a Poissonian distribution, i.e.

$$C = 2\sum_i [m_i - y_i + y_i(\ln y_i - \ln m_i)], \tag{1.7}$$

where y_i and m_i are the numbers of observed and model predicted counts in the i^{th} data point. When the background is also Poissonian, then we need to include the likelihood from both the source and the background (note that subtracting two Poissonian variables does not give a Poissonian distribution). We refer to this as the W-statistic. In this case, the observed counts, y_i, includes background. If t_s and t_b are the exposure times of source and the background and b_i represents the number of background counts observed within a region of similar size as the source region, then the W-statistic can be written as:

$$W = 2\sum_i \left[m_i + f_i - y_i \ln\left(m_i + \frac{t_s f_i}{t_s + t_b}\right) - b_i \ln\left(\frac{t_b f_i}{t_s + t_b}\right) - y_i(1 - \ln y_i) - b_i(1 - \ln b_i) \right], \tag{1.8}$$

$$f_i = \frac{y_i + b_i - m_i(1 + t_b/t_s) + d_i}{2}, \tag{1.9}$$

$$d_i = \sqrt{[m_i(1 + t_b/t_s) - y_i - b_i]^2 + 4b_i m_i(1 + t_b/t_s)}. \tag{1.10}$$

The XSPEC manual recommends binning data such that there is at least one count per bin.

Since C-statistics calculates the likelihood for Poissonian data, it can also be used when the number of photon counts is low. However, C-statistics does not give a direct relation to the null-hypothesis probability, and thus we need to use a different statistic to evaluate the goodness of the fit. Also, C-statistics cannot be directly used to compare two models with different d.o.f.

1.4.3 Akaike information criterion with correction

If our objective is to compare fits using two different models, then the Akaike Information Criterion (AIC; Akaike 1973, 1974) is a good estimator to get the relative likelihood of the models. However, AIC tends to favor the model with larger number of parameters when considering small samples. Therefore, we can use the AIC with correction (AICc; Cavanaugh 1997) given by:

$$\mathrm{AIC} = 2k - 2\ln\hat{L}, \tag{1.11}$$

$$\mathrm{AICc} = 2k - 2\ln\hat{L} + \frac{2k^2 + 2k}{n - k - 1}, \tag{1.12}$$

where k is the number of parameters in the model and $\hat{L}$ is the maximum likelihood that can be achieved for the given model, i.e. the likelihood with the best fitting parameters. From § 1.4.1 and 1.4.2, we see that $-2\log\hat{L}$ is equal to the χ^2 or C-statistic value of the best fitting model. A smaller AICc model indicates a better likelihood. Given two models with AICc_i and AICc_j, we can say that the model i is $\exp\left((\mathrm{AICc}_i - \mathrm{AICc}_j)/2\right)$ more likely to explain the data as compared to model j. However, similar to C-statistics, the AICc cannot comment on the goodness-of-fit of the given model.

1.4.4 Cramer-von-Mises test

The Cramer-von-Mises test (CvM Cramér 1928; von Mises 1931) is a goodness-of-fit test based on the empirical distribution function (EDF), defined as,

$$Y_i = \frac{\sum_{j=1}^{i} y_j}{\sum_{j=1}^{N} y_j}, \tag{1.13}$$

where y_j is the value at the j^{th} bin and N is the total number of bins. Then,

$$w^2 = \sum_i (Y_i - M_i)^2, \tag{1.14}$$

where w^2 is the CvM statistic, and Y_i, M_i are EDFs of observed data, model respectively. The null hypothesis probability decreases with increasing CvM value for a given number of d.o.f. While CvM is valid even for low photon counts, there is no direct relation between w^2 and null hypothesis probability. Therefore we need goodness simulations to evaluate the goodness-of-fit.

1.5 Spectral analysis with XSPEC

XSPEC[9] is a command-based, interactive, forward-modelling, X-ray spectral fitting package from the High-Energy Astrophysics Science Archive Research Center[10]. It is compatible with the data from most X-ray telescope missions and provides a wide variety of physical and empirical models to fit the data. In this section, I will discuss the models that are used in this work and explain the significance of the parameters in these models. There are two kinds of models in XSPEC – additive models that represent emission from the source, and multiplicative models (includes absorption, scattering, convolution, mixing, etc.) that show how the source radiation is modified in an energy-dependent way from the intervening material.

1.5.1 Inter-stellar absorption models

The absorption of X-ray flux from the inter-stellar medium (ISM) can significantly affect the X-ray spectrum, especially in the soft X-ray regime ($E < 2$ keV). `tbabs` is a commonly used ISM absorption model (Wilms et al. 2000) in XSPEC that includes the contribution of gas-phase ISM, grain-phase ISM and molecules in ISM. This model has only one parameter that determines the equivalent hydrogen column density (in the units of 10^{22} atoms cm^{-2}). The XSPEC model `tbvarabs` uses the same model but provides additional parameters to set the

[9] https://heasarc.gsfc.nasa.gov/xanadu/xspec
[10] https://heasarc.gsfc.nasa.gov

ISM abundances and grain properties. The ISM abundance model to be used can be set by the `abund` command in XSPEC. Another absorption model that uses Anders and Ebihara (1982) abundances irrespective of the `abund` command is the `wabs` model (Morrison and McCammon 1983)

1.5.2 Power-law model

Power-law model of the form $N(E) = N_0 E^{-\alpha}$, where $N(E)$ is the number of photons per unit area per unit time per unit energy bandwidth, E is the energy, α is the photon index and N_0 is a normalization constant, can be used to fit a wide variety of physical phenomena including synchrotron radiation and inverse Compton scattering. In this text we use the XSPEC model `pegpw` for the power-law fits. This model has four parameters – the photon index, the lower and the upper energy bounds (say E_1, E_2) in keV for the pegged normalization and the flux between energies E_1 and E_2 in ergs cm^{-2} s^{-1}. Note that E_1, E_2 are only relevant in calculating the flux and are not the limits within which the power-law is valid.

The value of the photon index suggests the nature of the X-ray emission (Power-law with smaller α is said to be harder). $\alpha \sim 1-2$ represent an extremely hard non-thermal radiation from a distribution of highly non-thermal electrons like those from shocked region in ultra-relativistic pulsar wind (e.g. Bogdanov et al. 2005). Strongly accreting systems and pulsar wind nebulae (PWNe) around NSs have $\alpha \sim 2$ (e.g. Kargaltsev and Pavlov 2008; Karpova et al. 2019, etc.). The forward shock from SNRs have $\alpha = 2 - 3.5$ (Hughes et al. 2000b; Williams et al. 2018). $\alpha \gtrsim 4$ indicates a BB or BB-like emission.

1.5.3 Thermal plasma models

In § 1.1.1 and § 1.1.5, we discussed the thermal emission of plasma in collisonal equilibrium. XSPEC models `apec` and `vapec` can be used to model such

radiations. Both these models use the temperature of the plasma (in the units of keV), the abundance of elements in the plasma, redshift to the source and a normalization parameter related to the emission measure to calculate the X-ray spectrum. While the `apec` model has a single parameter for the plasma abundance (with respect to abundance model set from the `abund` command), the individual abundances of He, C, N, O, Ne, Mg, Al, Si, S, Ar, Ca, Fe, and Ni with respect to the solar values can be set in the `vapec` model.

For plasma not in collisional equilibrium, we can use the `nei` and `vnei` XSPEC models. This models also fit for the ionization timescale, τ (units s cm^{-3}), of the plasma in addition to the parameters used in `apec` and `vapec`. The plasma is said to be in full non-equilibrium for $\tau < 5 \times 10^{10}$ s cm^{-3} s, i.e. none of the ion species have same temperature; and full equilibrium for $n_e t > 10^{12}$ s cm^{-3} s when the entire plasma can be described by a single temperature. Similar to the difference between `apec` and `vapec`, while `nei` has only one parameter for plasma abundance, `vapec` has thriteen parameters for individual abundance of the elements with respect to the solar values.

1.5.4 Neutron star atmosphere models

Given the complexity in modelling NS atmospheres, XSPEC has several models that can be used to fit thermal NS emission. In this text, I particularly consider the `nsatmos` model (Heinke et al. 2006) for non-magnetic hydrogen atmosphere and the `nsmaxg` model(Mori and Ho 2007; Ho et al. 2008) for NS atmospheres with magnetic field and composed of heavier elements. `nstamos` model fits for the un-redshifted effective temperature (returns the value of $\log T_{\rm eff}$, where $T_{\rm eff}$ is the effective temperature in K), mass of the NS (in the units of solar mass), true radius of the NS (in the units of km; typical values 8 - 15 km), distance to the NS in kpc and the fraction of the NS emitting radiation. `nsmaxg` has the same parameters in addition to another fixed parameter that determines the composition of the NS atmosphere, magnetic field and its orientation.

1.5.5 Blackbody model

In this text, we shall use the `bbodyrad` XSPEC model to fit BB emission. This model has two parameters – the temperature of the BB, and a normalization constant which is equal to $R_{\rm km}^2/D_{10}$ where $R_{\rm km}$ is the radius of the BB in km and D_{10} is the distance to the BB in the units of 10 kpc.

Given the observed X-ray spectrum, we use a combination of models in XSPEC to fit the data and analyze the goodness-of-fit using the statistical tools discussed in § 1.4.

1.6 On the road to the thesis

In this chapter, I briefly discussed the basics of X-ray detection and analysis. § 1.2.1 and § 1.2.2 showed the difference in the effective area of ACIS and HRC instruments. Thus for astrophysical sources, with multiple emission components (soft and hard), the HRC and ACIS instruments might be looking at different physical mechanisms. In Chap. 2, we shall be looking at a millisecond pulsar (MSP) and how ignoring the response of HRC and ACIS would lead to a false conclusion that the MSP is switching between a non-accreting radio-pulsar state and an accretion-powered state. In § 1.1.5, we saw how line emission can dominate the X-ray energies at which *Chandra* is sensitive. Instruments like ACIS, with a moderate resolution, cannot distinguish individual lines, especially when the photon count is low. In Chap. 3, I shall show examples of how this could lead to young SNRs being falsely identified as candidate active galactic nuclei (AGN). Chap. 4 explores the properties of a NS in the SNR 1E0102.2-7219, amid high interference from the SNR background. By modelling the background along with the source (instead of background subtraction), we are able to provide further evidence for the NS and study its thermal emission.

Chapter 2

Millisecond Pulsar 47 Tuc W

2.1 Introduction

Millisecond pulsars (MSPs) constitute a separate class of radio pulsars with exceptionally small periods, $P \sim 1$ ms and spin down rates, $\dot{P} \sim 10^{-19} - 10^{-21}$, as shown in Fig. 2.1 (check Manchester and Taylor 1977; Lyne et al. 1990; Becker 2009, for reviews on radio pulsars and MSPs). From these values, it can be calculated that MSPs have magnetic fields $B \sim 10^{17} \times (P\dot{P})^{1/2} = 10^8 - 10^9$ G and characteristic ages, $\tau \sim P/2\dot{P} \sim 10^8 - 10^{10}$ yrs. The extremely low values of the spin period, spin-down rates and magnetic field suggest that MSPs were formed differently from other radio pulsars.

Shortly after the discovery of the first MSP, PSR B1937+21 (Backer et al. 1982), it was proposed that MSPs are recycled NSs, spun up by accretion from a companion star during an X-ray binary phase (Alpar et al. 1982; Bhattacharya and van den Heuvel 1991). Support for this evolutionary model has come from detections of millisecond X-ray pulsations in many accreting NSs (e.g. SAX J1808.4–3658, Wijnands and van der Klis 1998; check Patruno and Watts 2012, for review); and the observed transitions of IGR J18245-2452 (Papitto et al. 2013), PSR J1023+0038 (Archibald et al. 2009; Stappers et al. 2014; Tendulkar et al. 2014, etc.) and XSS J12270-4859 (D. de Martino et al. 2010; Hill et al.

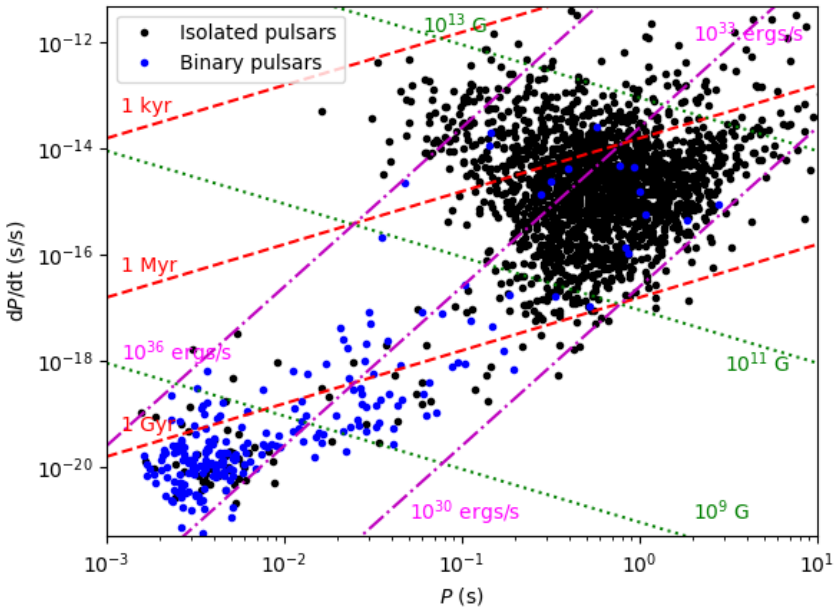

Figure 2.1: $P-\dot{P}$ diagram of pulsars. The pulsar population shows a bi-modal distribution with smaller period millisecond pulsars (MSPs) and longer "normal" period pulsars. The graph also shows lines of constant characteristic age, surface magnetic field and spin-down energy plotted in dashed red, dotted green, and dash-dotted magenta. MSPs are older and less magnetic than normal pulsars, and are more likely to be in binary systems. All data have been adopted from ATNF pulsar catalogue.

.

2011; Bassa et al. 2014; Bogdanov 2014; Roy et al. 2015) between an X-ray bright ($L_X > 10^{36}$ erg/s) low-mass X-ray binary (LMXB) state (observed only in IGR J18245-2542); a state of intermediate X-ray brightness ($L_X \sim 10^{33-34}$ erg/s) with unusual X-ray variability and signals of accretion; and a radio pulsar state. Detailed studies of PSR J1023+0038 across multiple wavelengths reveal that the X-ray intermediate state consists of three "modes" — a high flux mode ($\sim 10^{33}$ ergs s^{-1}) during which coherent X-ray and optical pulsations are observed (perhaps indicating active accretion); a low flux mode ($\sim 10^{32}$ ergs s^{-1}) where no X-ray pulsations have been observed, probably due to the accretion flow being pushed away from the pulsar by the pulsar wind; and sporadic flares reaching up to $\sim 10^{34}$ ergs s^{-1} (Archibald et al. 2015; Bogdanov et al. 2015;

Ambrosino et al. 2017). Similar behaviour is seen in the other two transitional MSPs (Papitto et al. 2013; D. de Martino et al. 2013) and in another candidate system CXOU J110926.4-650224 (Coti Zelati et al. 2019). In contrast, there is no accretion during the radio pulsar state. The X-ray emission during this state consists of a dominant shock component, that shows double-peaked pulsations, and sometimes a fainter, softer component, likely from heated magnetic polar caps (e.g. Bogdanov et al. 2005, 2010, 2011; Hui et al. 2015).

As predicted by the recycling model for the formation of MSPs, most MSPs are found in binary systems (also shown in Fig. 2.1). While only $\sim 4\%$ of longer-period radio pulsars are found in binary systems $\sim 64\%$ of MSPs have a companion star (ATNF pulsar catalog; Manchester et al. 2005)[1]. A significant fraction of these binary MSPs shows radio eclipses, in which radio pulsations cannot be detected during a fraction of the orbit, typically around the superior conjunction of the NS. These eclipsing binary MSPs are classified into two groups — black widows with tiny, partly degenerate companions of mass $M_2 \ll 0.1 M_\odot$, and the larger redbacks, with $M_2 \sim 0.1 - 0.4 M_\odot$ (Freire 2005; Roberts 2011). Redbacks have companions that are non-degenerate low-mass main sequence or subgiant stars. The first few redback MSPs were discovered in globular clusters (GCs; Camilo et al. 2000; D'Amico et al. 2001)[2], but targeted observations of the error circles of Fermi gamma-ray sources have identified many of these in the Galactic field (Roberts 2013).

Irradiation feedback from the pulsar heats up the companion and causes mass loss even when the companion does not fill its Roche lobe (quasi-Roche lobe overflow; Benvenuto et al. 2014, 2015). This stellar wind driven through pulsar heating can interact with the relativistic pulsar wind forming an intra-binary shock (IBS, Bednarek 2014). The structure of the IBS depends on a pressure balance between the pulsar and stellar winds. Wadiasingh et al.

[1] http://www.atnf.csiro.au/research/pulsar/psrcat/

[2] Refer http://www.naic.edu/~pfreire/GCpsr.html for up-to-date catalog of MSPs

(2018) explore the extreme cases when the pressure balance is set by the magnetic fields (requiring a several kilogauss poloidal field in the companion wind at the shock; the magnetospheric scenario) or from an advection-dominated supersonic companion wind (gas-dominated scenario, in which the magnetic field is dynamically unimportant). While the magnetospheric scenario is stable for timescales of at least $\tau_p > 10^8$ s for a low companion mass loss rate ($|\dot{m}_c| < 10^{15}$ g s^{-1}), the gas dominated scenario requires large mass loss rates ($|\dot{m}_c| \sim 10^{15}-10^{16}$ g s^{-1}) and is unstable (on dynamical time-scales; $\mathcal{O}(10^4\text{s})$), i.e., such systems demand additional self-regulatory stability mechanisms. The pressure balance and stability of such companion wind-dominated shocks needs to be investigated further. However, the large magnetic fields required in the former case are also difficult to explain.

In this paper, we use simulations of the gas-dominated pressure balance to model the observations of 47 Tuc W. This model is parametrized by two factors: the ratio of the momentum flux from stellar and pulsar winds, $\beta = \dot{M}_w v_w c/\dot{E}$ (where $\dot{M}_w$ is the mass loss rate of the companion, v_w is the companion wind velocity, $\dot{E}$ is the rate of energy loss by the pulsar and c is the speed of light), and the ratio of the companion wind velocity to orbital velocity of the companion, $f_v = v_w/v_{\rm orb}$. The parameter β determines the distance of the shock from the companion star, its curvature and whether the shock wraps around the companion ($\beta < 1$, pulsar dominated) or the pulsar ($\beta > 1$, companion dominated). The term f_v determines the asymmetry of the shock due to orbital motion ($f_v \gg 1$ implies a symmetric IBS).

Electrons accelerated across this shock cool through synchrotron or IC process, making IBS the dominant hard X-ray and γ-ray source (Bednarek 2014). The X-ray light curve of a typical eclipsing binary pulsar shows a double-peaked structure due to the eclipse from the companion and Doppler beaming of the radiation. Thus, studying the magnitude and location of minima in the count-rate constrains the parameters of the IBS. Early models of the shock

considered only the pulsar wind dominated scenario, with the prominent dip in X-ray flux near the radio eclipse explained as the occultation of the shock close to the L1 point (e.g. Bogdanov et al. 2005). However, detailed modelling of the IBS has shown that Doppler beaming of X-rays away from us in the companion wind dominated case can also cause a significant drop in the X-ray flux during the radio eclipse (Romani and Sanchez 2016; Sanchez and Romani 2017; Li et al. 2014; Al Noori et al. 2018, etc.).

The companions in compact tidally locked red-back and black widow systems are asymmetrically heated due to the pulsar wind. The resulting temperature difference across the surface of the companion leads to variability in the optical bands (Bogdanov et al. 2011; Bogdanov 2014; Romani and Shaw 2011; Kong et al. 2012; Breton et al. 2013, etc.). Given the orbital ephemeris from radio and γ-ray observations, studying the optical and X-ray light curves could reveal the details of pulsar heating mechanisms, companion wind, component masses and the geometry of the systems (Djorgovski and Evans 1988; Callanan et al. 1995). The detailed modelling of these light curves become especially important while measuring the precise mass of massive pulsars, which could give crucial clues towards understanding the NS equation of state (van Kerkwijk et al. 2011). Romani and Sanchez (2016) and Sanchez and Romani (2017) have shown that including the reprocessing of pulsar wind through intra-binary shock (IBS) and channelling of the pulsar wind by the magnetic field of the companion star is essential to fit the high precision optical data for black widow pulsars.

47 Tuc hosts 25 pulsars, all MSPs with $P \sim$ 2–5 ms, of which 15 are in binary systems (Camilo et al. 2000; Ridolfi et al. 2016; Pan et al. 2016; Freire et al. 2017). Radio eclipses have been detected in five of these pulsars, of which two are confirmed to be redbacks — PSR J0024-7204W (47 Tuc W), and PSR J0024-7201V (47 Tuc V). 47 Tuc W was first detected by Camilo et al. (2000) using the Parkes radio telescope, with a period of 2.35 ms and an orbital period of 3.2 hrs. The pulsar was eclipsed in the radio for $\sim$ 25% of its orbit. The

position and the nature of the companion were deduced by identifying a periodic variable in a long series of Hubble Space Telescope (HST) exposures, which showed variability matching the pulsar's known orbital period (Edmonds et al. 2002). 47 Tuc W has a companion consistent with a main sequence star, with $M_2 > 0.13\ M_\odot$ (Edmonds et al. 2002). The most up-to-date timing solution for this system gives an orbital frequency $f_b = 8.71 \times 10^{-5}$ s^{-1} with a first derivative $\dot{f}_b = -1.26 \times 10^{-18}$ s^{-2}, but multiple orbital period derivatives are necessary to account for its behaviour (Ridolfi et al. 2016).

The position of 47 Tuc W is coincident with that of X-ray source W29 detected by Chandra ACIS observations of the core of 47 Tuc (Grindlay et al. 2001; Heinke et al. 2005). X-ray analysis of 47 Tuc W showed that the emission consisted of two components — a hard non-thermal component that shows a decrease in flux for $\sim 30\%$ of its orbit, which contributes about 70% of the observed X-ray luminosity; and a soft, thermal component, which did not show variability (Bogdanov et al. 2005). Bogdanov et al. (2005) proposed that the non-thermal spectrum is from an IBS due to the interaction of the pulsar wind with the stellar wind and that the thermal component arises from the NS surface (e.g. Becker and Trümper 1993; Zavlin et al. 2002). Observations of 47 Tuc W using the Chandra HRC-S instrument in 2004–05 indicated an absence of X-ray eclipses, although the total exposure, and the number of collected counts, were larger (Cameron et al. 2007). This suggested the possibility that 47 Tuc W, like several other redbacks, may be a transitional MSP, and may have engaged in a state transition between these observations.

In this paper we use the 2014–15 Chandra ACIS-S observations of 47 Tuc W (PI Bogdanov; Bogdanov et al. 2016; Bahramian et al. 2017; Bhattacharya et al. 2017), along with the previous ACIS-S (PI Grindlay; Heinke et al. 2005) and HRC-S (PI Rutledge; Cameron et al. 2007) data to look into this puzzle. We also perform phase-resolved X-ray spectroscopy on the ACIS-S data to look into any changes in the spectra between the two observations and to derive

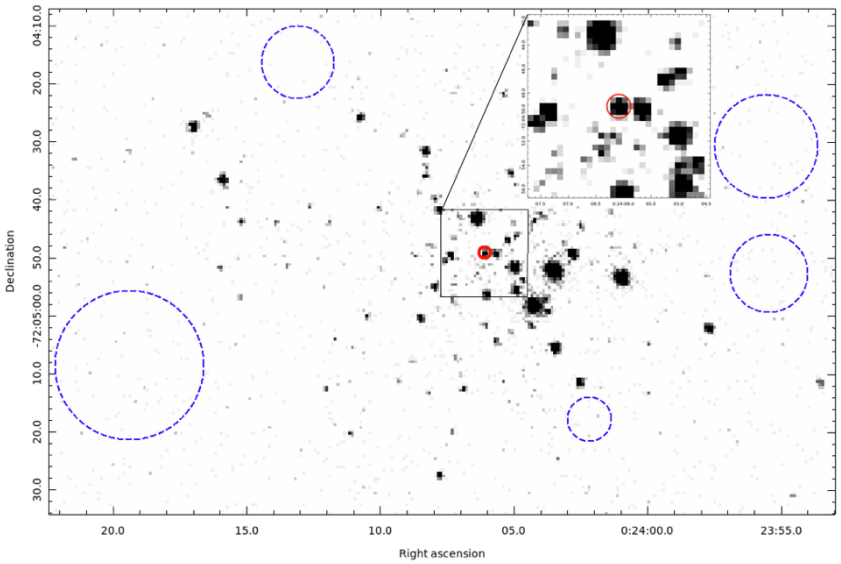

Figure 2.2: X-ray image of the globular cluster 47 Tuc. The solid red circle of radius 1″ centred at $\alpha = 00^{h}24^{m}06.^{s}1, \delta = -72°04'49.''1$ shows the region from which source photons of 47 Tuc W were extracted. We select 5 regions around 47 Tuc without any X-ray sources for background extraction (shown in dashed blue).

the properties of the suggested IBS. In § 2.2, we give a detailed description of how we extracted the source photons and analyzed the data. § 2.3 discusses our analysis of the X-ray light curve of 47 Tuc W and explains our hypothesis for why variability was not observed in the HRC data. We analyze the X-ray spectra of the system in § 2.4. In § 2.5, we use the ICARUS modules developed by Romani and Sanchez (2016) and Sanchez and Romani (2017) to model the optical (Edmonds et al. 2002) and X-ray light curves of 47 Tuc W and study the properties of the IBS and its heating of the companion. We discuss our conclusions on the properties of the IBS in § 2.6.

2.2 Observations and data reduction

Due to the density of the compact core of 47 Tuc, we used the sub-arcsecond resolution of the CXO and the *Hubble Space Telescope* (HST) to investigate 47 Tuc W binary system.

Table 2.1: X-ray observations used for analysis of 47 Tuc W.

Obs ID	Exposure(ks)	Year	Obs ID	Exposure(ks)	Year
2735	65.24	2002	5542	49.76	2005
3384	5.31	2002	5543	50.65	2005
2736	65.24	2002	5544	49.83	2005
3385	5.31	2002	5545	51.64	2005
2737	65.24	2002	5546	48.27	2005
3386	5.54	2002	6230	44.77	2005
2738	68.77	2002	6231	46.89	2005
3387	5.73	2002	6232	44.15	2005
15747	50.04	2014	6233	97.18	2006
15748	16.24	2014	6235	49.93	2006
16527	40.88	2014	6236	51.70	2006
16528	40.28	2015	6237	49.96	2005
16529	24.70	2014	6238	48.20	2005
17420	9.13	2014	6239	49.88	2006
			6240	49.07	2006

Observations on the *left* are taken with ACIS-S instrument and those on the *right* are taken with HRC instrument.

2.2.1 X-ray observations

§ 1.2 summarizes the characteristics of ACIS and HRC detectors of *Chandra*. In general, the ACIS detectors retain (limited) spectral information, have higher sensitivity above 1 keV and have a very low background, while the HRC detectors retain sub-millisecond timing information, have a slightly higher angular resolution than ACIS, and have higher sensitivity below 1 keV as compared to ACIS detectors.

We analyzed the ACIS-S 2002 observations (exposure $\sim$ 300ks) and 2014–15 observations (exposure $\sim$ 200ks) to construct the X-ray spectra and the light curves of the 47 Tuc W system. We also studied the HRC observations of 2005–06 (exposure $\sim$ 800ks) to verify the light curves presented by Cameron et al. (2007) and to check for rotational variability in 47 Tuc W using the new orbital ephemeris of Ridolfi et al. (2016). The details of all X-ray observations used are summarized in Table 2.1.

CIAO version 4.9 was used for data reduction and image processing. The initial data downloaded from WebChaSeR were reprocessed according to CALDB 4.7.6 calibration standards using the `chandra_repro` command. The parameters `'badpixel'` and `'process_events'` were set to "yes" to create new level=1 event and badpixel files using the latest calibrations. To prevent good events from being removed, the parameter `'check_vf_pha'` was set to "no". The `'pixel_adj'` parameter was set to "default" (EDSER) to obtain the maximal spatial resolution. The X-ray photons corresponding to 47 Tuc W were extracted from a circular region of 1″ radius around the source ($\alpha = 00^{\rm h}24^{\rm m}06.^{s}1; \delta = -72°04'49''.1$) as shown in Fig. 2.2. This region was selected as a compromise between selecting maximum photons from the target, and avoiding photons from the neighboring source W32. Photons were corrected for barycentric shifts using the `axbary` tool of CIAO. The aspect solution file and the exposure statistics file were also corrected to correct the good time intervals. Five regions close to 47 Tuc, and free of any resolved X-ray sources were chosen for background subtraction.

2.2.2 Optical observations

We use the reduced optical data as presented in Bogdanov et al. (2005) for our analysis. HST observations of 47 Tuc reveal the optical light curve of the companion star. Bogdanov et al. (2005) plot the light curves in the ACS bands F435W (67 points), F475W (19 points), F555W (8 points) and F606W (6 points), but only as normalized fluxes as a function of an unpublished radio ephemeris. However they also plot fluxes in these four bands with the SED of the companion at maximum, and from this, we can estimate the fluxes of the individual detections. Also, Cadelano et al. (2015) plotted WFC3 F300X (12 points) and F390W (5 points) magnitudes (on the HST system) as a function of binary phase on an updated radio ephemeris by P. Freire. We direct readers to the above-mentioned papers for details of the optical data reduction methods.

2.2.3 Variability analysis

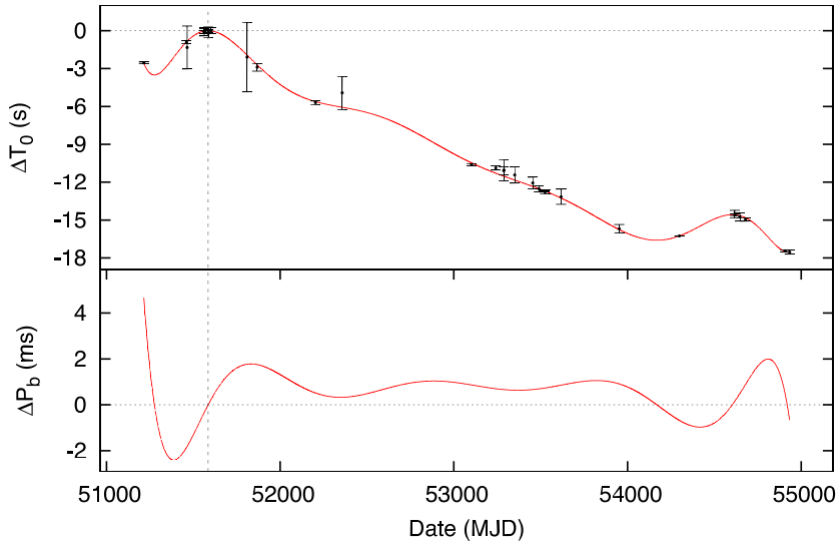

Figure 2.3: Variation in orbital parameters of 47Tuc W. (Top:) Deviation of observed times of the passage of the ascending node from the predicted times (assuming a Keplerian orbit). (Bottom:) Change in orbital period with respect to the reference value - $8.70594798 \times 10^{-5}$ Hz (Ridolfi et al. 2016). Image credits - Ridolfi et al. (2016).

We used the ephemeris data of 47 Tuc W from Ridolfi et al. (2016) to prepare the phase-folded X-ray light curve. However, this ephemeris contains many derivatives and thus diverges for times (such as our 2015 epoch) outside the epochs over which it is defined. To prevent this divergence, we employed the following, more approximate but far more stable method: We approximated the graph of deviation of the time of passage of the ascending node as a function of time (Fig.2.3) as a straight line. A uniform slope in ΔT_0 indicates a constant difference in orbital frequency from its reported value. This can be seen from the bottom plot in Fig. 2.3 where ΔP_b is approximately constant, $\sim$ 1s, over a wide range of modified julian dates (MJDs).

Using this slope and the reported frequency in Ridolfi et al. (2016), we calculated the orbital frequency to be $8.70594745 \times 10^{-5}$ Hz. We considered a reference epoch of 51585.3327 MJD (time of periastron, also the time of

passage of the ascending node since $\omega = 0$) to calculate the phase. Given $\dot{f} = -1.26(4) \times 10^{-18}$ s^{-1} in Ridolfi et al. (2016) (this seems to be the upper limit according to Fig 2.3), the error in phase, $\Delta\phi \leq 0.5\dot{f}(t_{\rm end} - t_{\rm start})^2 = 0.1$. Here $t_{\rm start}$ and $t_{\rm end}$ are the starting time of the 2002 observations and the ending time of the 2015 observations respectively.

We then constructed phase-folded light curves in the energy interval $0.3 - 8.0$ separately for each observation from the corresponding barycentre-corrected source and background files using the `dmtcalc` and `dmextract` commands. We created phase-folded light curves for observations taken in 2002, 2004–05 and 2014–15 separately. This enables us to study any possible differences in the light curves across the three epochs. We binned the light curves to intervals of 0.1 in phase so that the counts per bin are above 10 for most bins, so that Gaussian error bars and χ^2 statistics may be used. To study the variability across different energy bands, we constructed additional light curves in a very low energy band (0.2 - 1.0 keV), and a high energy band (2.0 - 8.0 keV) for the ACIS-S 2002 and 2014–15 observations. For the light curves in very low energy and high energy bands, we needed a larger bin size of 0.2 in phase to have reasonable counts in each bin. In order to study the IBS in more detail, we also constructed light curves with bin size 0.06 in phase that shows the double-peaked structure more clearly.

2.2.4 Spectral analysis

The HRC observations do not contain sufficient information regarding the energy of the photons and hence cannot be used for spectral analysis. We analyzed the data from the 2002 and 2014-15 ACIS observations separately to investigate any change in the spectrum. To look into the nature of the dips in the light curves, we grouped the data from the phase intervals when the 47 Tuc W system showed a decrease in the count rate separately from the remaining intervals. For this purpose, we extracted the good time intervals corresponding

to these phases using the `dmgti` tool and aligned them to the corresponding ACIS observations using the `gti_align` tool. We then extracted the spectrum from individual observations using the `spec_extract` tool and combined them using `combine_spectra` in order to increase the photon count. We grouped the spectra such that each bin had at least 1 photon, and used C-statistics (Cash 1979) for spectral analysis. χ^2-statistics with more conservative binning gave similar results, with larger errors. For the purpose of plotting alone, the data points were re-binned such that each bin had at least fifteen counts.

2.3 X-ray variability

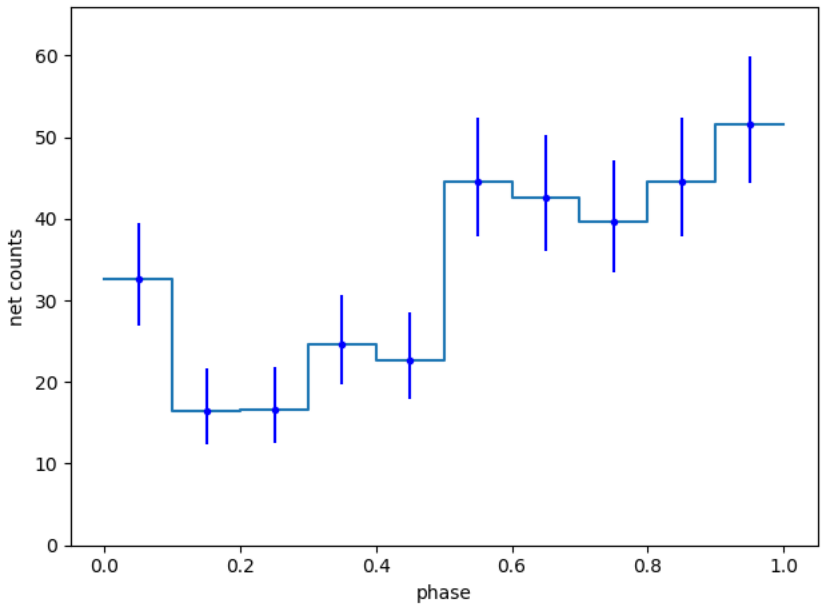

Figure 2.4: Phase-folded light curve of 47 Tuc W from 2002 observations, after background subtraction. Net count rate decreases in the interval $0.1 - 0.4$. Fitting this to a constant gives $\chi^2/\text{d.o.f} = 49.9/9$ (p-value $= 1.1 \times 10^{-7}$) indicating that a non-variable source cannot produce this light curve.

We extracted the light curves from the 2002 ACIS observations, and the 2004–05 HRC observations, from the reprocessed data, after accounting for the changes in the calibration standards. Figure 2.4 shows the phase-folded

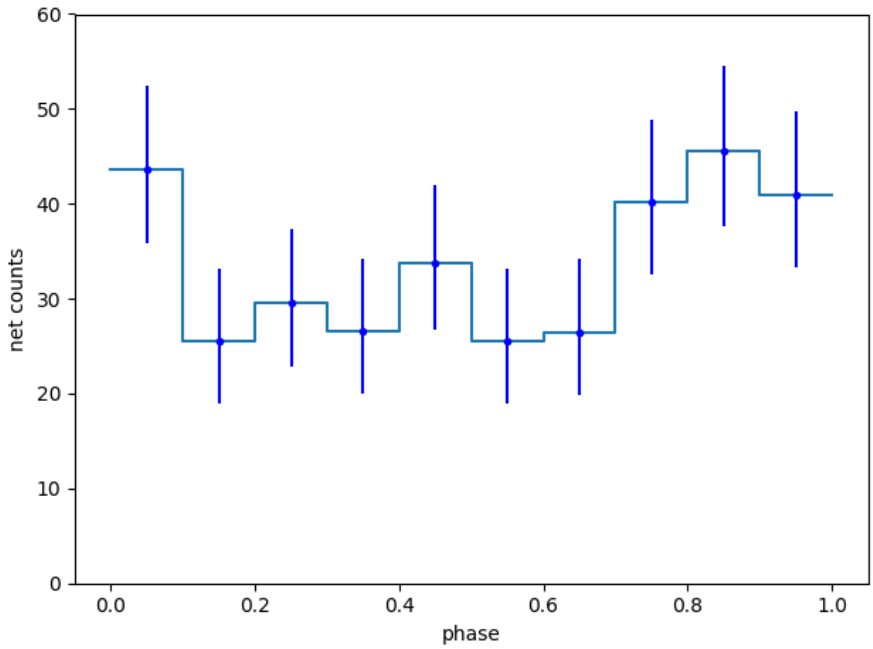

Figure 2.5: Phase-folded light curve of 47 Tuc W from 2005 observations after background subtraction. This light curve is significantly different from that from the 2002 observations. The changes in the net counts per bin are within the error limits. Fitting a constant to this light curve gives χ^2/d.o.f = 16.6/9 (p-value = 0.06) indicating that these changes are not of statistical importance.

light curve from the 2002 observations. We clearly see the dips in the light curve identified by Bogdanov et al. (2005) during phases 0.1–0.4. These phases correspond to the radio eclipse of the MSP (0.09–0.43, Ridolfi et al. 2016). Fitting the folded light curve to a constant gave $\chi^2 = 49.9$ for 9 degrees of freedom (d.o.f), giving the probability of the null hypothesis (no variability), p-value $= 1.1 \times 10^{-7}$. Figure 2.5 shows the phase-folded light curve from the 2004–05 observations. As can be seen from the graph, the changes in the net counts per bin were less significant. Fitting this curve to a constant value gave $\chi^2 = 16.6$ for 9 d.o.f, i.e p-value = 0.055. Thus this light curve could be produced from a constant source, as noted by Cameron et al. (2007).

Figure 2.6 shows the light curve extracted from the 2014–15 ACIS observations. Note that the light curve is very similar to that in the 2002 observations. We observed periodic transits in this light curve too. The positions of these dips

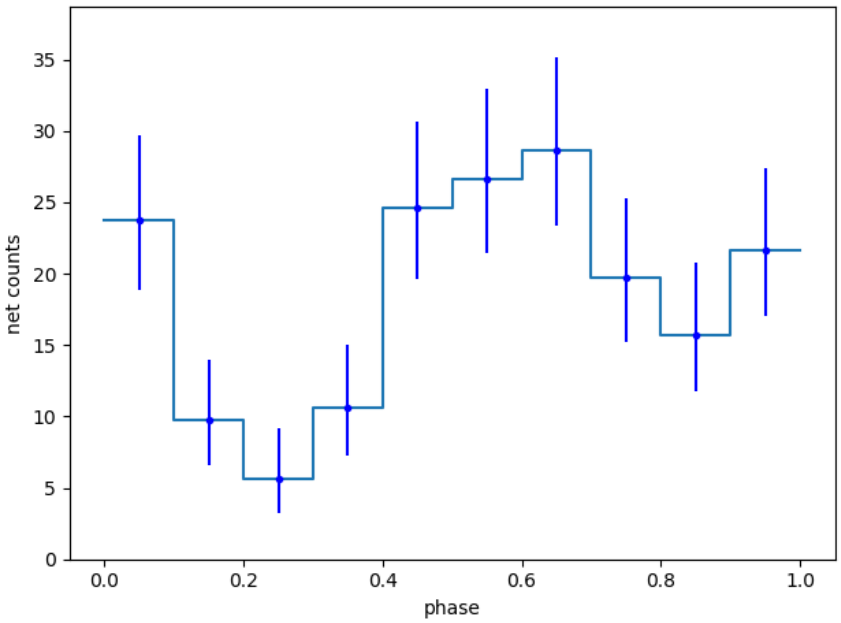

Figure 2.6: Phase folded light curves from 2014-15 observations. The features are very similar to the 2002 observations. Fitting a constant to this light curve gives $\chi^2/\text{d.o.f} = 42.0/9$ (p-value $= 3.3 \times 10^{-6}$) indicating evidence of variability.

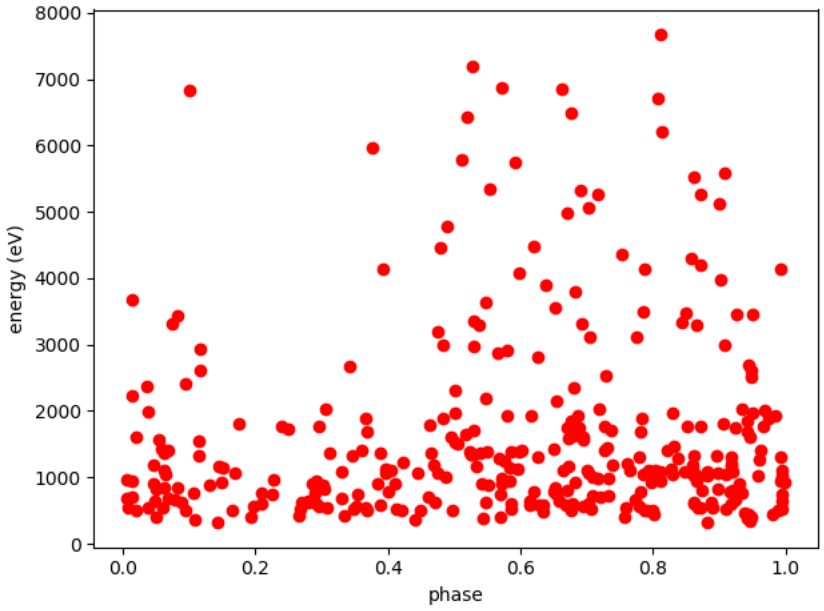

Figure 2.7: Scatter plot of photon energy vs. phase for the 2002 data. Each dot represents an X-ray photon detected. We see that the source exhibits larger variability at higher energies than at lower energies.

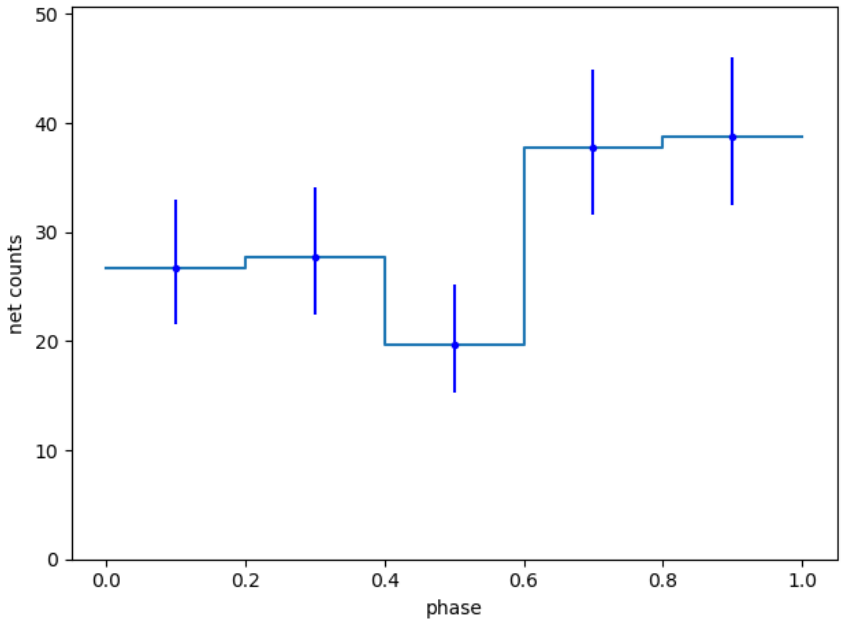

Figure 2.8: Phase folded light curves for 0.2 - 1.0 keV photons, from ACIS 2002 observations. Fitting a constant to this light curve gives χ^2/d.o.f = 9.01/4 (p-value = 0.06) indicating that the dips in the light curve are less significant at lower energies.

were slightly different due to approximations made in calculating the ephemeris of 47 Tuc W. We saw earlier that the error in the phase between 2002 and 2015 observations, $\Delta\phi \leq 0.1$, which corresponds to 1 phase bin. The change in the photon count rates between 2000–02 & 2014–15 observations can likely be attributed to the decreased effective area of Chandra at low energies, though we cannot rule out a real flux change from the light curve alone (see spectral fitting below). A fit of a constant to the light curve gave $\chi^2 = 42.0$ for 9 d.o.f, slightly less than that of the 2002 data, because of increased errors (due to fewer photon counts). The χ^2 value for 9 d.o.f corresponds to a null hypothesis (that the source has a constant count rate) probability of 3.3×10^{-6}.

To visualize the difference in the 2005 light curve from the other two light curves, we first plotted a scatter plot of photon energy versus phase for the 2002 data, as shown in Fig. 2.7. The density of points in a region depicts the number of photons observed with the given energy during a given phase. From the

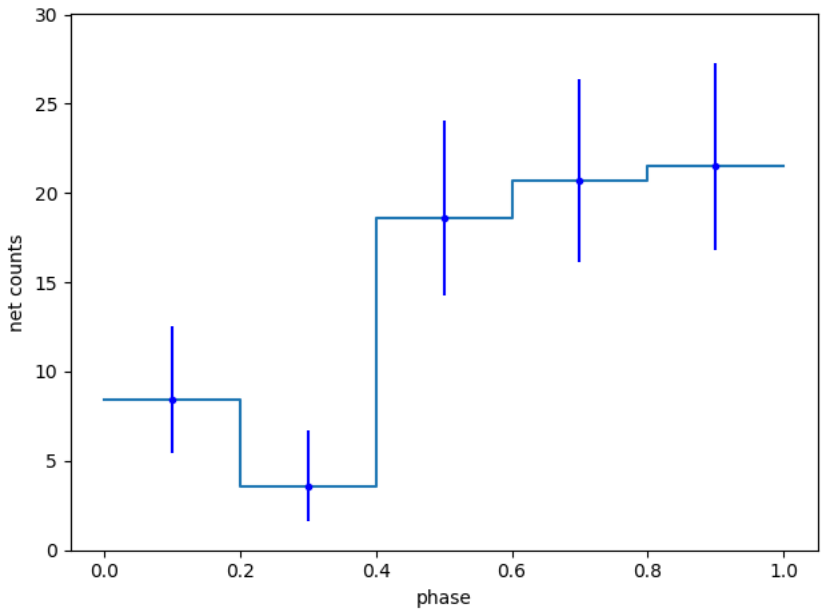

Figure 2.9: Light curve for photons in the energy interval 2.0 - 8.0 keV. $\chi^2 = 27.2$ for a constant fit, i.e the probability $= 1.8 \times 10^{-5}$ indicating that such a light curve cannot be produced by a non-variable source.

figure, we saw that the variation in the count rate was much more prominent for high energy photons, in comparison to the lower energy photons which showed a much smaller variation. Thus, the lower sensitivity of the HRC detector to the variable, higher energy X-rays might be the reason for the absence of variability. To investigate this, we plotted the light curve for 2002 observations for photons in the energy interval 0.2–1.0 keV (shown in Fig. 2.8). We increased the bin size to 0.2 so that each bin had a reasonable number of photons to apply Gaussian statistics. This reduced the χ^2/d.o.f to 9.01/4, i.e. the probability that the source has a constant light curve in this range is 0.06 - approximately equal to that of the 2005 light curve.

This could imply that the differences in the light curves of ACIS and HRC observations may be explained by the difference in the sensitivity of the two detectors. On the other hand, in Fig.2.9, the light curve for high energy photons (2.0–8.0 keV) from the ACIS 2002 observations, the change in counts per bin in the light curve was much more significant, $\chi^2 = 27.2$ for 4 d.o.f i.e. probability

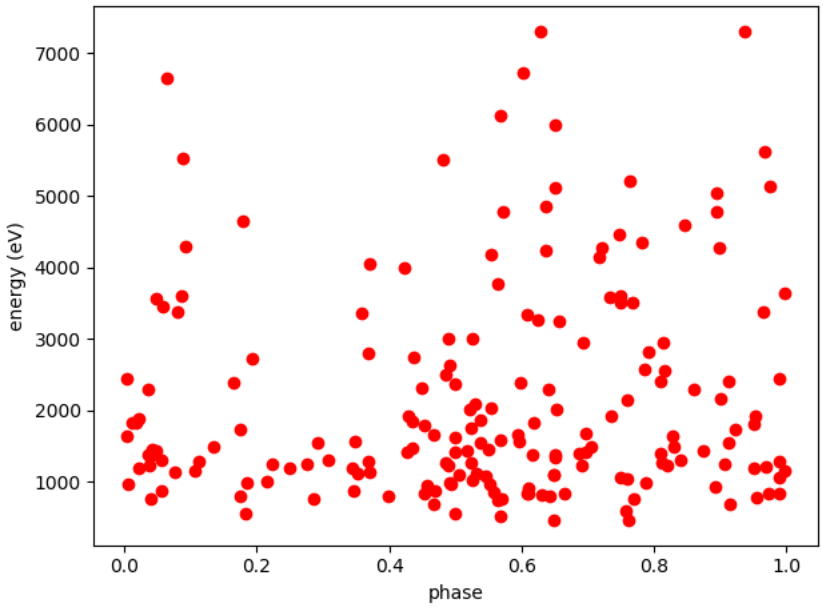

Figure 2.10: Scatter plot of energy vs. phase for each photon detected in the 2014-15 data. Comparing with fig. 2.7, we can see that the number of low energy photons has significantly decreased. We attribute this to the reduction in the effective area of ACIS at low energies over the intervening years.

of the source having a constant count rate was 1.8×10^{-5}.

Figure 2.10 shows the scatter plot of photon energy vs. photon phase for the 2014–15 observations. The declining effective area of ACIS over the mission produced the reduced number of low energy photons in Fig. 2.10, compared to Fig. 2.7. The 2014–15 observations showed a less dramatic difference in the variability characteristics of low and high-energy photons, largely because the lowest-energy photons are simply missing in 2014–15 (Fig. 2.11). The high energy light curves of 2000–02 and 2014–15 observations are similar.

2.4 X-ray spectrum

We analyzed the X-ray spectrum for 47 Tuc W using the 0.3–8.0 keV photons where the ACIS instrument has the highest sensitivity. We divided the data into 4 groups to look for changes in the spectra during the drop in X-ray flux,

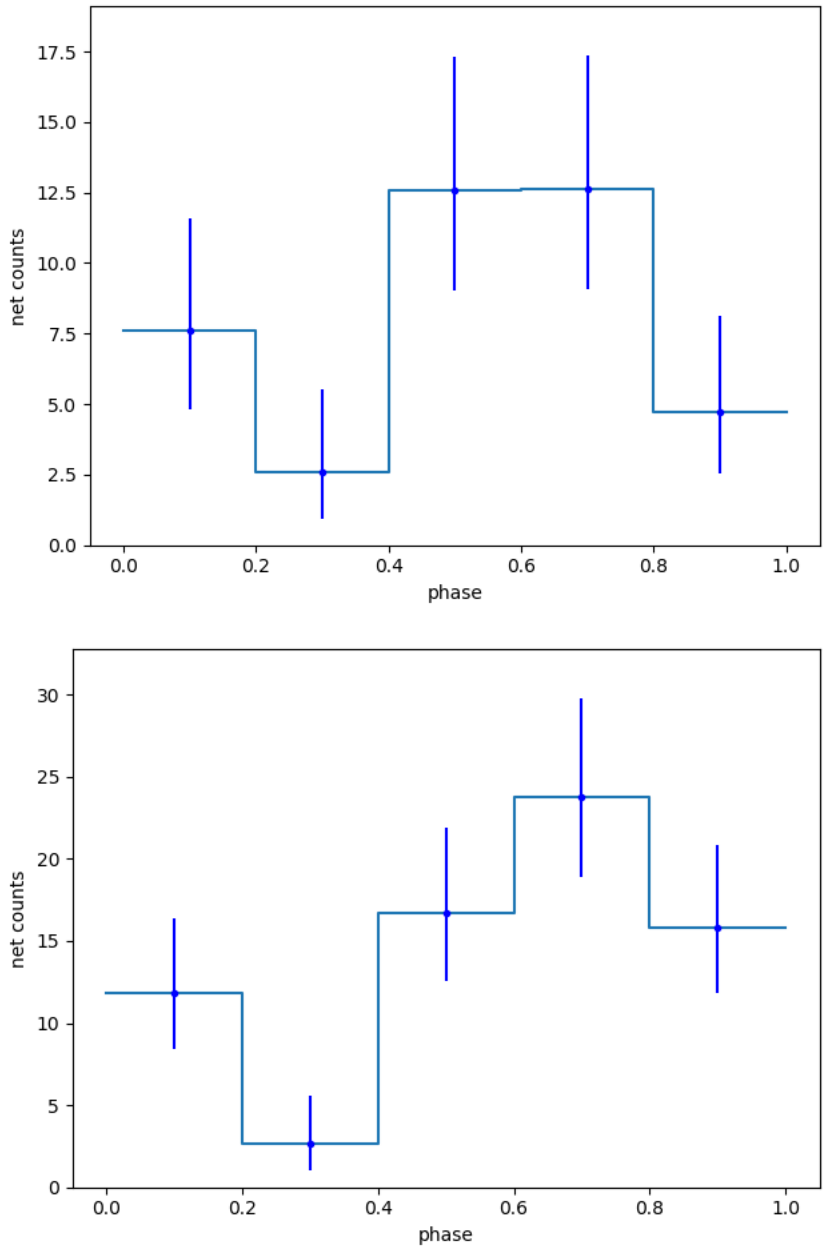

Figure 2.11: Phase folded light curves for different energy bands for the 2014-15 observations.(Top) Low energy photons ($0.2 - 1.0$ keV). $\chi^2 = 17.9$ for 4 d.o.f i.e. $p = 0.04$ for a constant fit. (Bottom) High energy photons ($2.0 - 8.0$ keV). $\chi^2 = 30.7 \implies p = 3.5 \times 10^{-6}$ for a constant fit.

and between the 2002 and 2014–15 observations:

- **D1** - Data from 2002 observations extracted from phases 0.0–0.1, and 0.4–1.0 (where count rate is not low).

- **D2** - Data from 2014–15 observations extracted from phases 0.0–0.1, and 0.4–1.0 (where count rate is not low).
- **D3** - Data from 2002 observations extracted from phases 0.1–0.4 (where flux decreases).
- **D4** - Data from 2014–15 observations extracted from phases 0.1–0.4 (where flux decreases).

Table 2.2: Summary of spectral analysis of 47 Tuc W

Data Groups	Parameters	PEGPW	PEGPW(linked indices)
D1	PL index	1.60 ± 0.15	1.50 ± 0.12
	PL flux	$1.07^{+0.14}_{-0.13} \times 10^{-14}$	$1.13^{+0.14}_{-0.13} \times 10^{-14}$
	T_{eff}	-	-
	Radius	-	-
	Thermal Flux	-	-
D2	PL index	1.29 ± 0.21	1.50 ± 0.12
	PL flux	$1.54^{+0.26}_{-0.22} \times 10^{-14}$	$1.42^{+0.20}_{-0.18} \times 10^{-14}$
	T_{eff}	-	-
	Radius	-	-
	Thermal Flux	-	-
D3	PL index	$2.43^{+0.40}_{-0.38}$	$2.30^{+0.33}_{-0.31}$
	PL flux	$3.98^{+0.98}_{-0.82} \times 10^{-15}$	$4.07^{1.01}_{-0.85} \times 10^{-15}$
	T_{eff}	-	-
	Radius	-	-
	Thermal Flux	-	-
D4	PL index	$2.01^{+0.58}_{-0.56}$	$2.30^{+0.33}_{-0.31}$
	PL flux	$5.03^{+1.88}_{-1.47} \times 10^{-15}$	$5.00^{1.81}_{-1.47} \times 10^{-15}$
	T_{eff}	-	-
	Radius	-	-
	Thermal Flux	-	-

Note: Flux is expressed in the units of ergs/cm^2/s, Teff in K and radius in km. Refer the text for the definitions of D1, D2, D3, D4. "Radius" refers to the radius of the region emitting thermal radiation. Flux is calculated between 0.3–8.0 keV. Error-bars represent 90% confidence intervals, i.e. 1.65σ. Note that $T_{\rm eff}$, radius and thermal flux aren't defined for PEGPW model.

Table 2.2 Continued: Summary of spectral analysis of 47 Tuc W

Data Groups	Parameters	(PEGPW+BBODYAD)	(PEGPW+NSATMOS)
D1	PL index	$1.16^{+0.24}_{-0.26}$	$1.04^{+0.26}_{-0.27}$
	PL flux	$1.04^{+0.16}_{-0.15} \times 10^{-14}$	$1.01^{0.17}_{-0.16} \times 10^{-14}$
	T_{eff}	$1.84^{+0.48}_{-0.58} \times 10^{6}$	$1.05^{+0.36}_{-0.37} \times 10^{6}$
	Radius	$2.38^{+2.73}_{-0.87} \times 10^{-1}$	$1.29^{+1.61}_{-0.49}$
	Thermal Flux	$1.58^{+0.60}_{-0.61} \times 10^{-15}$	$2.02^{+0.62}_{-0.66}$
D2	PL index	$1.16^{+0.24}_{-0.26}$	$1.04^{+0.26}_{-0.27}$
	PL flux	$1.45^{+0.24}_{-0.21} \times 10^{-14}$	$1.45^{+0.26}_{-0.22} \times 10^{-14}$
	T_{eff}	$1.84^{+0.48}_{-0.58} \times 10^{6}$	$1.05^{+0.36}_{-0.37} \times 10^{6}$
	Radius	$2.38^{+2.73}_{-0.87} \times 10^{-1}$	$1.29^{+1.61}_{-0.49}$
	Thermal Flux	$1.58^{+0.60}_{-0.61} \times 10^{-15}$	$2.02^{+0.62}_{-0.66}$
D3	PL index	$1.16^{+0.24}_{-0.26}$	$1.04^{+0.26}_{-0.27}$
	PL flux	$3.04^{+1.64}_{-1.38} \times 10^{-15}$	$2.41^{+1.65}_{-1.29} \times 10^{-15}$
	T_{eff}	$1.84^{+0.48}_{-0.58} \times 10^{6}$	$1.05^{+0.36}_{-0.37} \times 10^{6}$
	Radius	$2.38^{+2.73}_{-0.87} \times 10^{-1}$	$1.29^{+1.61}_{-0.49}$
	Thermal Flux	$1.58^{+0.60}_{-0.61} \times 10^{-15}$	$2.02^{+0.62}_{-0.66} \times 10^{-15}$
D4	PL index	$1.16^{+0.24}_{-0.26}$	$1.04^{+0.26}_{-0.27}$
	PL flux	$4.38^{+2.45}_{-2.05} \times 10^{-15}$	$3.73^{2.48}_{-1.92} \times 10^{-15}$
	T_{eff}	$1.84^{+0.48}_{-0.58} \times 10^{6}$	$1.05^{+0.36}_{-0.37} \times 10^{6}$
	Radius	$2.38^{+2.73}_{-0.87} \times 10^{-1}$	$1.29^{+1.61}_{-0.49}$
	Thermal Flux	$1.58^{+0.60}_{-0.61} \times 10^{-15}$	$2.02^{+0.62}_{-0.66} \times 10^{-15}$

Due to the low photon counts, we grouped data to have a minimum of 1 photon per bin and used C-statistics to fit the models. We used the `tbabs` model in XSPEC to model the absorption due to the interstellar medium. We fixed the hydrogen column density towards 47 Tuc to be 3.5×10^{20} cm^{-2} (Bogdanov et al. 2016) and `wilms` abundances (Wilms et al. 2000) were used. We describe the various spectral models used and the approximations made in the paragraphs below. The results of our spectral analysis are summarized in Table 2.2. Note that the errors correspond to 90% confidence intervals.

We first fit all four data groups independently with a power law (model 1). Due to the low photon counts, the parameters of the spectral fits for D3 and

D4 were essentially unconstrained. We observed that the photon indices of D1 and D2 were consistent within their 90% confidence errors, as were those of D3 and D4. Therefore, we linked the photon indices of (D1, D2) and (D3, D4) to be equal. Fitting a pegged power law, with linked photon indices (model 2), gave $\Gamma = 1.50 \pm 0.12$ for D1/D2 and $\Gamma = 2.30^{+0.33}_{-0.31}$ for D3/D4.

The large change in the photon index during the dips suggested the possibility of two spectral components in 47 Tuc W. The hard spectrum could be emitted from the intra-binary shock (IBS). The decrease in the flux from this hard spectral component could be due to eclipsing from the companion or due to Doppler beaming of shocked material away from us. The softer spectrum could be thermal emission from the NS, which does not change. The soft spectrum from the NS could be fit by either a BB (model 3) or a NS atmosphere (Heinke et al. 2006, `nsatmos`,) model (model 4). We assumed the emission from the NS to be constant with phase, as the inclination is unlikely to be large enough for a direct occultation of the NS by the small secondary (which would be very short even if it occurred, <5% of the orbit). Therefore we assumed that the parameters of the softer spectrum are constant across all the data groups. Note that since there could be some X-ray emission from the IBS, even during the phases where flux decreases, we do not fix the power-law flux to be zero in data groups D3 and D4.

We modelled the BB emission using `bbodyrad` in XSPEC, limiting the BB temperature to <0.3 keV (check Chap. 4 for details on NS surface temperatures). Including the thermal component decreased the power-law index slightly to $\Gamma = 1.16^{+0.24}_{-0.26}$. The BB component had an effective temperature $T_{\rm eff} = 1.84^{+0.48}_{-0.58} \times 10^6$ K, and a radius $R_{\rm eff} = 0.24^{+0.27}_{-0.09}$ km — consistent with emission from heated polar caps of an NS. From the best-fit model (Fig. 2.12 *(top)*, we saw that the non-thermal flux was roughly twice the thermal flux even during the phase interval 0.1–0.4.

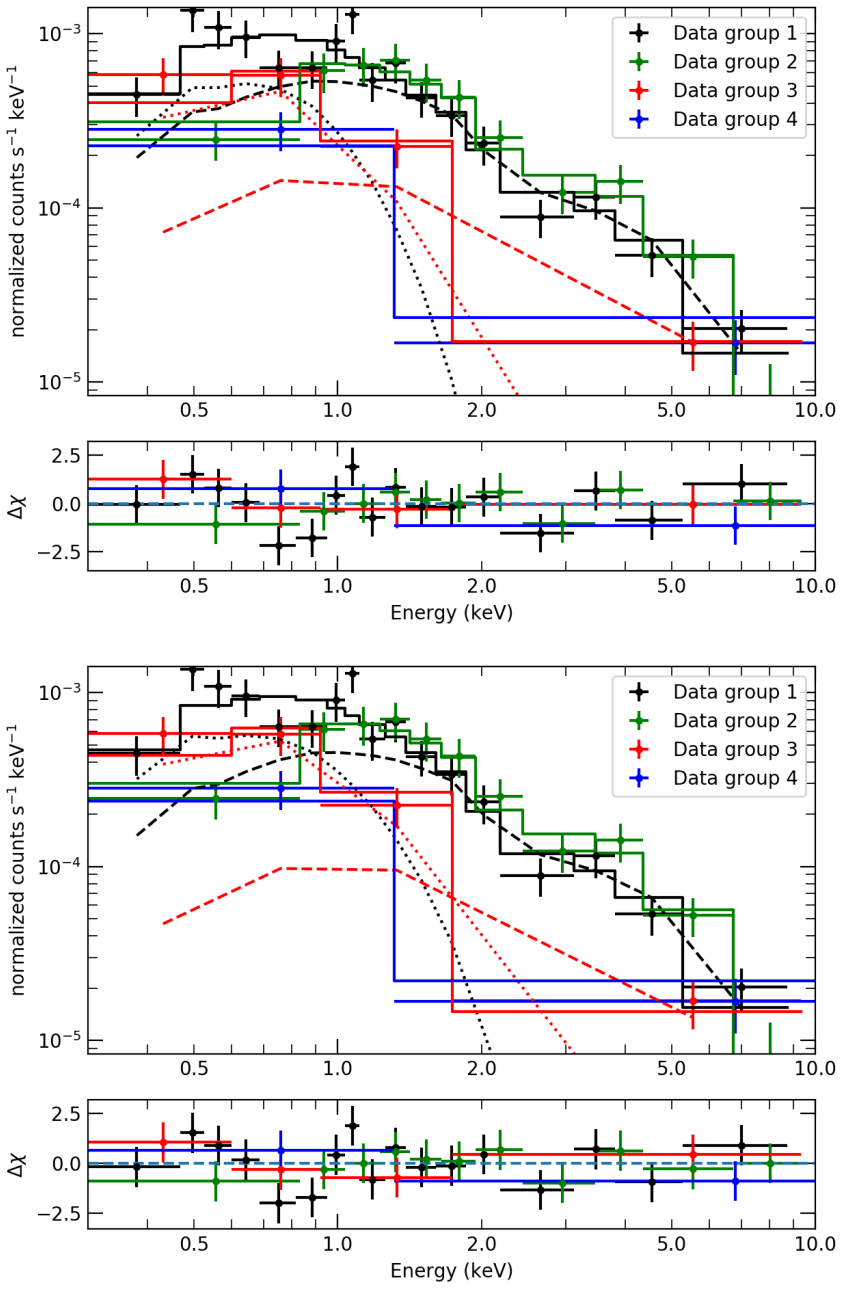

Figure 2.12: Spectral fits to the 2002 data (black: bright phases — 0.0–0.1, 0.4–1.0; red: faint phases — 0.1–0.4), and 2014–15 data (green: bright phases - 0.0–0.1, 0.4–1.0. blue: faint phases — 0.1–0.4). *Top*: Model with power-law and BB components, and `tbabs` absorption. *Bottom*: Model with power-law and NS atmosphere components, plus absorption. We also plot the thermal (dotted) and non-thermal (dashed) components of the spectrum separately for the 2002 bright (black) and faint (red) spectra.

We fit the NS atmosphere using the `nsatmos` model of XSPEC. We fixed the NS mass to 1.4 $M_\odot$, the NS radius to 10 km, and the distance to 4.53 kpc (Bogdanov et al. 2016). The `norm` parameter in this model allows a rough estimate of the fractional part of the NS emitting, which we left free (model 4). The best-fitting model shown in Fig. 2.12 (bottom), has a photon index, $\Gamma = 1.04^{+0.26}_{-0.27}$ — similar to that in the `tbabs*(pegpw+bbodyrad)` model. We find that the temperature and radius of the hotspot on the NS are $1.05^{+0.36}_{-0.37} \times 10^6$ K and $1.29^{+1.61}_{-0.49}$ km, respectively. Since `nsatmos` is a more physically motivated model for emission from a NS surface, we use this model for further analysis.

From the values of the thermal flux in Table 2.2, we saw that the thermal emission is much smaller($\approx 1/5$) than the non-thermal emission. The radius of the region emitting thermal radiation was much smaller than the NS radius, indicating the presence of hot spots on the NS. Fixing the `norm` to 1 and varying the radius of the NS gave an extremely small radius ($\sim$ 5 km), which is physically not plausible. The non-thermal and thermal luminosities were estimated as $L_{X,\rm pl} = (2.5 \pm 0.4) \times 10^{31}$ ergs/s, and $L_{X,\rm th} = 5^{+1}_{-2} \times 10^{30}$ ergs/s between 0.3 - 8.0 keV for the 2002 data. The non-thermal flux seemed to have increased during the 2014–15 observations by $\gtrsim 3\sigma$. This could be caused by the changes in the properties of the IBS. Since the pulsar properties are not expected to evolve on such small time scales, we suggest a change in the wind from the companion star between these dates.

2.4.1 Verifying the HRC light curve

We used our best-fitting spectral model for the ACIS-S data to check if *Chandra* HRC-S could indeed detect the change in the light curves. We used the *Chandra* PIMMS tool[3] to estimate the background and the source count rates for the thermal and non-thermal X-ray emission separately. We used the

[3] http://cxc.harvard.edu/toolkit/pimms.jsp

`tbabs*(bbodyrad+pegpw)` model due to the limited capability of the PIMMS tool. We found the estimated count rates for the power-law and BB components to be 3.3×10^{-4} cts/s and 1.9×10^{-4} cts/s. The background count rate of HRC was 2.4×10^{-4} cts/s for an extraction region of $1''$. The total exposure of all 2014-15 observations was 781.88 ks. Thus each bin in our light curve (where bin size 0.1) corresponded to ~ 78 ks. The estimated number of source counts in each bin would be 25.7 and 14.8 due to the non-thermal and the thermal components respectively, and the background counts in each bin would be 18.7. From our spectral analysis, we see that the photon count rate from power-law drops by a factor of 0.3 during the dip in the ACIS-S light curve. Using Gaussian errors the average net source counts per bin during phase 0.0-0.1 and 0.4-10.0 would be 40.5 ± 10.7, while that in 0.1 - 0.4 would be 22.5 ± 9.1. We see that the two counts are only $\sim 2\sigma$ apart i.e increase χ^2 by ~ 8. Given that we have 9 d.o.f, we would not be able to detect such a change from the statistical noise.

2.5 Analysis of the optical data

We converted the normalized fluxes in Bogdanov et al. (2005), magnitudes in Cadelano et al. (2015) and their errors to units of ergs cm^{-2} s^{-1} Hz^{-1} (f_ν) and plotted them in Fig. 2.13 (two periods are shown for clarity). As expected for a low-mass companion star strongly heated on one side, the optical light curves showed relatively shallow dips, while the UV light curves showed a deeper modulation from the higher temperature of the heated side of the companion. All light curves show a maximum at $\phi_B \sim 0.75$ relative to the phase of the pulsar ascending node, indicating strong heating of the pulsar companion. The light curves appear slightly asymmetric and F300X, in particular, is shifted to peak at $\phi_B \approx 0.8$. Unfortunately, lacking the detailed ephemeris used, we do not know the accuracy of the phase determination. However, comparing the

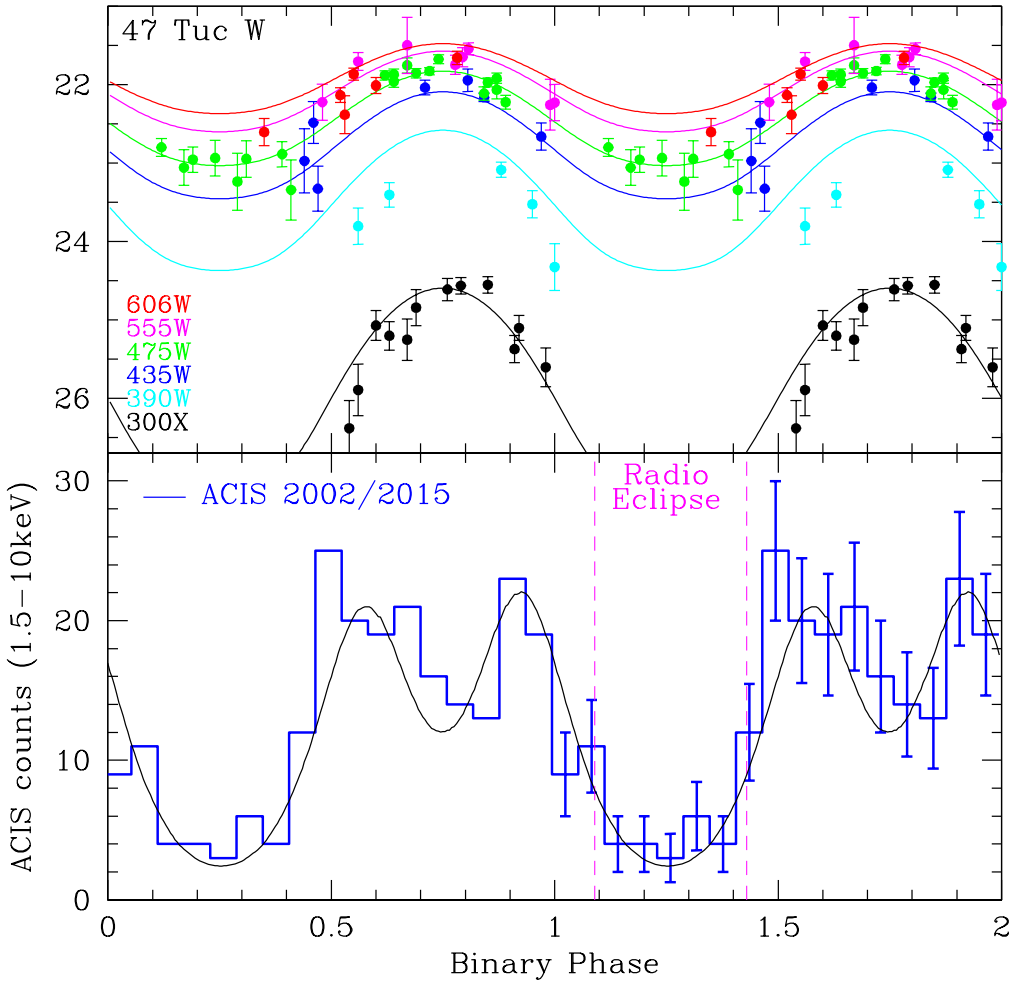

Figure 2.13: *Top* HST ACS and WFC3 measurements of 47 Tuc W in four optical and two UV-dominated bands (after Bogdanov, et al. 2005 and Cadelano et al. 2015). Our best-fitting model light curves are superimposed. Note the poor fit to the F390W points. *Bottom*: An X-ray light curve in the energy interval $1.5 - 10.0$ keV from the combined data sets, with the model X-ray light curve for the geometry of the combined fit.

phase of maxima and the minima of the optical light curves, we estimate the error in the phase to be ≤ 0.05.

These light curves are compared with the 1.5–10 keV ACIS light curves, combining the 2002 and 2015 data sets, folded on the Ridolfi et al. (2016) radio ephemeris. The X-ray maximum is broad, covering over half of the orbit $\phi_B \approx$

0.45–0.10, with a hint of a double-peak structure ($\phi_{p,1} \approx 0.58$, $\phi_{p,2} \approx 0.93$) bracketing the optical maximum. The radio eclipse covers $\phi_B = 0.09$–0.43 (Ridolfi et al. 2016).

To model the heated companion surface, we use the ICARUS code of Breton et al. (2012) with the extensions for IBS illumination (Romani and Sanchez 2016). This requires tables of atmosphere colors as a function of local surface temperature and gravity. We extract these from the Spanish Virtual Observatory fold of the BT-Settl atmosphere models (Allard et al. 2012) through the responses of the individual HST filters, convert the normalized surface fluxes to f_ν, and supply them to the ICARUS code. Note that the four optical HST bands are quite similar in spectral coverage, and indeed the light curves largely overlap at the level of the reconstructed photometry. The five F390W points are the most problematic with our models generally over-predicting this flux. It is possible that the inferred calibration is off by a factor of $\sim 2\times$, but we have not been able to identify a source for such an error. Since the HST optical and ultraviolet data points were taken at different times, we speculate that the companion's heated side may show secular variability, due perhaps to variations in the properties of the IBS.

2.6 Properties of the intra-binary shock

The non-thermal emission is most probably synchrotron emission (Bogdanov et al. 2005) from particles accelerated by the IBS formed by the interaction of the pulsar wind and the stellar wind from the main-sequence companion. To study the emission from the IBS, we have further extended the ICARUS IBS code (Romani & Sanchez 2016) with a module following the variation of the synchrotron emission across the shock (details to be presented in Kandel et. al., in prep). In this model, the shape of the IBS is controlled by the wind momentum ratio β and a wind velocity asymmetry factor f_v. The IBS spectral

behaviour is controlled by the evolution of the bulk flow speed $\Gamma_{\rm bulk}$, the spectral index of the accelerated electron power-law and the characteristic magnetic field strength at the IBS nose. 47 Tuc W is a redback MSP, and like many such binaries, the momentum of the massive companion wind dominates so that $\beta > 1$ and the IBS wraps around the pulsar. Accordingly, we expect the growth of the post-shock bulk velocity is slower than in the black widow case, which was the focus in Romani & Sanchez (2016). The data seem to support this and here we adopt

$$\Gamma_{\rm bulk} \approx 1.1 \left(1 + 0.1 \frac{\delta r}{r_0}\right), \tag{2.1}$$

where r_0 is the stand-off distance of the shock from the nose, and δr is the increase in radial distance from the nose of the IBS.

For many black widows and redbacks, the IBS synchrotron emission dominates non-thermal X-rays directly from the pulsar. For 47 Tuc W, the relatively hard observed X-ray spectrum (photon index ~ 1.04) implies negligible contribution by the IBS emission to the flux in the optical/UV bands, which are dominated by the heated face of the companion. To constrain the system parameters, we have fitted the combined optical and X-ray light curves. Since there are many more optical than X-ray data points, we have increased the weight of the X-ray points by 3×. Fig 2.13 shows the model-fitted optical and X-ray light curves, and the fitted parameters are listed in Table 2.3. The resulting fit gives χ^2/d.o.f ~ 2.8, which is not statistically acceptable. The poor fit appears to be principally due to the F390W normalization. The UV phase shift is also important. These can likely be addressed by models that include a surface hot spot, as generated by particle precipitation to a magnetic pole (Sanchez and Romani 2017), however, higher S/N X-ray and optical light curves are needed for such detailed modelling.

Table 2.3: Parameters of the best-fitting IBS model for 47 Tuc W X-ray and optical data

Parameter	Symbol	Value
Inclination (deg)	i	63.76 ± 7.11
Roche lobe filling factor	f_1	0.65 ± 0.03
Star temperature (night, K)	T_N	4959 ± 70
Direct heating luminosity (erg s^{-1})	L_H	$(5.81 \pm 0.41) \times 10^{33}$
IBS luminosity (erg s^{-1})	L_{IBS}	$(3.67 \pm 0.20) \times 10^{32}$
Magnetic field at nose (G)	B	10.0
Wind momentum ratio	β	5.7
Wind velocity asymmetry factor	f_v	800

Note: From the best-fitting values, we infer that the IBS is dominated by the momentum from the companion wind and hence wraps around the MSP. The companion star seems to be directly heated rather than from the IBS.

2.7 Summary and conclusions

In this work, we analyzed the *Chandra* observations of 47 Tuc over the years 2000–2015 to study if the redback pulsar 47 Tuc W was a transitional MSP. The ACIS-S X-ray light curves of 47 Tuc W in the years 2002 and 2014–15 showed a drop in the count rate during the phases $\sim$ 0.1–0.4 (where phase 0 corresponds to the time of periastron passage). However, the X-ray light curve of 2004–05 did not show any statistically significant change in the orbital period folded count rate. Our analysis of the energy of the photons and their phase showed that the variability in the count rate is more pronounced at higher energies. Thus instruments like *Chandra* HRC, which are primarily sensitive to soft X-rays (and have low effective areas for photons $>$ 2 keV), cannot detect such change in the flux. This hypothesis is supported by the X-ray light curves in the energies 0.2–1.0 keV being consistent with a constant fit. The estimated count rates on HRC-S using our spectral fit to the X-ray light curve were similar over all the phases showing that HRC-S instrument will not be able to detect the variability in the X-ray light curve.

Our analysis of the X-ray spectrum showed that the X-ray emission consisted

two components — a dominant hard non-thermal power-law (power-law index, $\Gamma \sim 1.1$) which showed variability (drops by a factor of 3 during the phases 0.1–0.4) and a soft thermal emission which could be assumed to be constant over all phases. The thermal emission could be fit using a thermal BB with effective temperature $T_{\rm BB} = 1.8^{+0.5}_{-0.6} \times 10^6$ K and radius $R_{\rm BB} = 0.24^{+0.27}_{-0.09}$ or a $M_{\rm NS} = 1.4$ $M_\odot$, $R_{\rm NS} = 10$ km NS H atmosphere with effective $T_{\rm eff} = (1.0 \pm 0.4) \times 10^6$K and radius $R_{\rm eff} = 1.29^{+1.61}_{-0.49}$ km. The unabsorbed non-thermal luminosity, $L_{X,\rm pl} = (2.5 \pm 0.4) \times 10^{31}$ ergs s^{-1} was about 5 times the thermal luminosity, $L_{X,\rm th} = 5^{+1}_{-2} \times 10^{30}$ ergs s^{-1}.

The X-ray and the optical variability of 47 Tuc W system allowed us to study the properties of the IBS and the geometry of the binary system. Modelling the double-peaked X-ray light and the optical light curve using ICARUS IBS code showed that the companion is heated directly from the pulsar wind rather than from the IBS – direct heating luminosity is ~ 15 times IBS luminosity. Though the companion does not fill the Roche lobe, the heating of companion leads to a strong stellar wind which has 5.7 times the momentum of the pulsar wind (i.e. the IBS is wrapped around the pulsar and the dips in the X-ray light curve in the phase interval 0.1–0.4 is due to Doppler beaming of synchrotron radiation away from us). The high χ^2/d.o.f of our fits could be attributed to the channelling of pulsar wind by the magnetic field of the companion. Higher S/N X-ray and optical light curves would allow us to model these effects.

Our temporal and spectral analysis are limited by low photon count from the source. Longer exposures or use of instruments like Lynx (The Lynx Team 2018) with a larger effective area but a similar angular resolution would allow us to further study the binary system. A larger number of X-ray photon counts would allow a smaller bin time and thus we could study of double-peaked nature of the light curve in more detail and constrain the properties of the IBS better. More photons in the region corresponding to radio eclipse will also allow better modelling of the underlying thermal NS emission.

Chapter 3

Candidate Active Galactic Nuclei in Dwarf Galaxies

3.1 Introduction

The key properties of a galaxy bulge (its mass and velocity dispersion) are tightly correlated with the mass of the central BH hosted by the galaxy (Fig. 3.1 shows the relation between the mass of the bulge and the mass of the central BH). These observational results are explained through theories of co-evolution of the galaxies and central BHs which suggest that the radiation and outflows from the AGN hosted by galaxies act as feedback in regulating the properties of the galaxy, at least in part. The irradiation from accretion around AGN can evaporate the cold gas while the jets and outflows heat and expel the warm gas from the galaxy. Thus the feedback from the AGN terminates the fuel source for star-formation as well as accretion onto the AGN itself.

As seen in Fig. 3.1, while massive galaxies and bright cluster galaxies with classical bulges show clear evidence of AGN feedback, it has been harder to study AGN activity in low-mass galaxies that lack bulges, or have only pseudo-bulges (i.e. have more disk-like properties in comparison to classical bulges; e.g. Booth and Schaye 2013; Dashyan et al. 2018). Such observations have also motivated

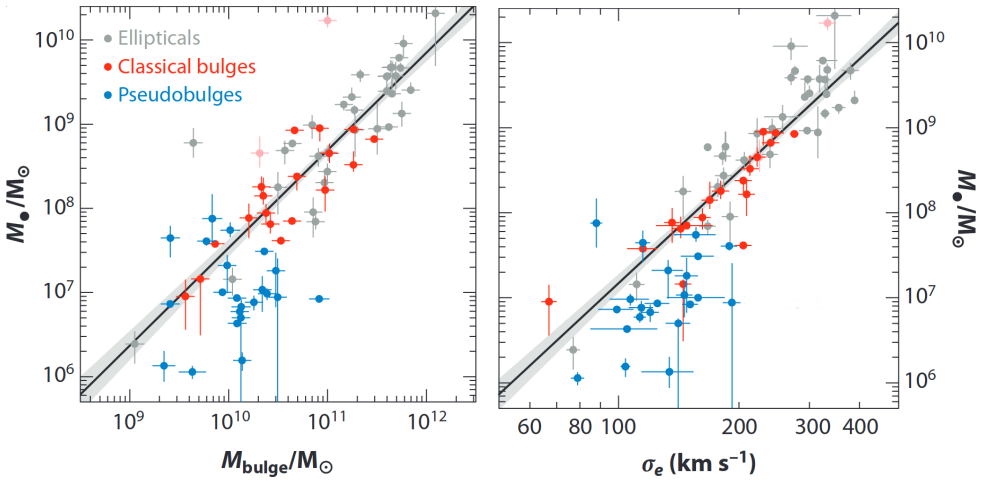

Figure 3.1: Co-evolution of the galactic bulge and the central BH. (*Left*) Relationship between mass of the bulge (M_{bulge}) and the mass of the central BH (M_{BH}). (*Right*) Change in dispersion velocity of stars in the galactic bulge (σ_e) with M_{BH}. We see that bright elliptical galaxies and galaxies with classical bulges show a tight relationship with M_{BH} but lower-mass galaxies with pseudo-bulges show large scatter. Image credits: Kormendy and Ho (2013).

theories which suggest that the observed connection between BH and bulge might only be a result of repeated mergers (i.e. they aren't physically coupled Jahnke and Macciò 2011). Volonteri and Natarajan (2009) points out that the relation of BH masses to galaxy and bulge masses on the low-mass end will provide key evidence as to the origin of massive BHs, as either direct collapse of $\sim 10^4$ $M_\odot$ clouds versus initial seeds of $\sim 10^3$ $M_\odot$ BHs from the collapse of Population III (first generation) stars. Recent works have been divided as to whether the standard BH-bulge mass relation continues straightforwardly to lower-masses (Barth et al. 2005; Xiao et al. 2011; Baldassare et al. 2015) or shows substantial changes (Greene et al. 2008; Jiang et al. 2011). Thus the detections of AGN powered by lower mass BHs (10^3–$10^6 M_\odot$, hereafter intermediate-mass black holes or IMBHs, as opposed to super-massive black holes or SMBHs) in low-mass bulgeless or pseudo-bulge galaxies are crucial for understanding how SMBHs and galaxies grow.

Increasing efforts have been devoted towards finding IMBHs in dwarf and/or bulgeless galaxies over the past 30 years. For instance, the small, bulgeless

spiral galaxy NGC 4395 hosts a faint Seyfert I AGN, verified to be powered by a relatively small BH, of mass $(3.6 \pm 1.1) \times 10^5$ $M_\odot$ (Filippenko 1989; Peterson et al. 2005). The dwarf elliptical galaxy Pox 52 also hosts a weak AGN, with a central BH engine of mass $(3.2 \pm 1.0) \times 10^5$ $M_\odot$ (Kunth et al. 1987; Barth et al. 2004; Thornton et al. 2008). A number of optical spectroscopic searches for "dwarf" Seyfert nuclei have been conducted (e.g. Ho et al. 1995; Greene and Ho 2004, 2007; Reines et al. 2013; Lemons et al. 2015; Chilingarian et al. 2018; Liu et al. 2018), identifying a large number of candidate IMBHs.

A number of methodologies have been used to test whether emission line regions at the centres of galaxies are produced by AGN, including: the ratios of emission lines indicating the ionization state (and thus suggesting an origin either in star formation or from AGN activity Baldwin et al. 1981); the breadth of H lines (Greene and Ho 2005; Reines et al. 2013); and the identification of X-rays from the candidate AGN. The Wide-Field Infrared Survey Explorer (WISE) provides mid-infrared colour information, which has been exploited to identify AGN regardless of obscuration (Stern et al. 2012; Satyapal et al. 2014). Abel and Satyapal (2008) proposed using the luminosity of a [Ne V] line in the mid-infrared, which also allows the study of obscured AGN.

However, young SNRs evolving in a high-density medium can also produce emission lines in a relatively high ionization state, and broad H lines (e.g. Filippenko and Sargent 1989; Terlevich et al. 1992; Baldassare et al. 2016). Hainline et al. (2016) showed that selection using only mid-infrared colors from WISE is vulnerable to confusion from star-forming galaxies. The formation of Wolf-Rayet and massive O stars in young starbursts can produce extreme ultraviolet flux that could lead to high ionization of Ne (Schaerer and Stasińska 1999; Kewley et al. 2001; Lutz et al. 1998). Accurate measurement of the BH mass requires time-consuming reverberation mapping (Peterson 1993; Peterson et al. 2005; Peterson 2014, etc.) or dynamical spectroscopic measurements (Du et al. 2017; Songsheng and Wang 2018), which have been done for relatively

few candidate IMBH AGN in small galaxies. Thus, identification of X-rays from candidate AGN has become a crucial element of many campaigns to identify IMBH AGN, sometimes being regarded as the crucial piece of proof necessary to verify a candidate AGN (e.g. Greene and Ho 2007; Secrest et al. 2012; Chilingarian et al. 2018).

The key element of the present work is the realization that moderate-resolution X-ray spectroscopy, even with relatively small numbers of counts, is capable of distinguishing between some hot plasma models, typical of young thermal SNRs[1], and the power-law spectra typical of AGN. This opportunity is provided by the very strong emission lines in the metal-enriched thermal ejecta dominating typical SNR spectra, especially the strong Si lines around 1.8 keV. The ability to identify X-ray spectra produced by thermal SNR emission allows us to constrain whether X-ray emission arising from a candidate AGN is more consistent with an AGN or an SNR. In this paper, we study two test cases in detail.

3.1.1 Potential AGN in Henize 2–10 and NGC 4178

Henize 2–10

Henize 2–10 is a dwarf starburst galaxy without a central bulge, located at a distance of 9 Mpc (Vacca and Conti 1992), with a stellar mass of 3.7×10^9 $M_\odot$ (Reines et al. 2011). Reines et al. (2011) identified an X-ray source located in Henize 2–10 with a steep-spectrum radio source. Comparing the X-ray and radio luminosities of this source, Reines et al. (2011) argued that the radio and X-ray luminosities and their ratio excluded origins other than an accreting black hole. The Fundamental Plane of black hole activity relates black hole mass, X-ray luminosity, and radio luminosity, for black holes accreting in a radiatively

[1]Not all SNR X-ray spectra are dominated by thermal ejecta; some, like the Crab and SN 1006, are dominated by non-thermal synchrotron emission from pulsar wind nebulae or shocks.

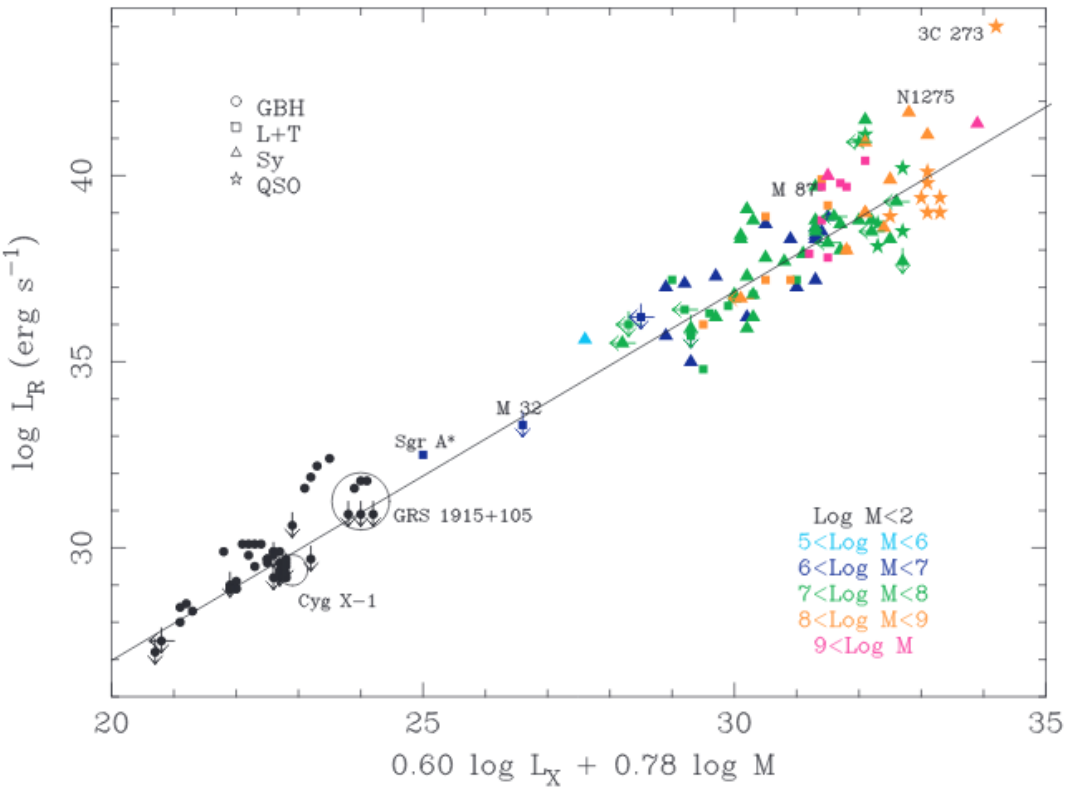

Figure 3.2: Fundamental plane of BH activity relating L_X, L_R & M_{BH}. Thus given that the emission is from an active BH we can use this plot to estimate the mass of the central BH. Image credits - Merloni et al. (2003)

inefficient state (e.g. Merloni et al. 2003, shown here in Fig. 3.2). Using the fundamental plane of BH activity, Reines et al. (2011) argued that the observed radio brightness requires a BH with a mass $\sim 2 \times 10^6$ $M_\odot$, as smaller black holes do not generate this radio brightness at the observed L_X. The identification of a BH with such a large mass in a dwarf starburst galaxy without a bulge was quite surprising, as it suggested that large BHs could appear first, before galactic bulges grow. Such a discovery would have strong implications for the evolution of galaxies and BHs.

Deeper *Chandra* observations of Henize 2–10 (Reines et al. 2016) resolved the X-ray source identified as the candidate AGN into two components. One source, coincident with the radio point source, was suggested by Reines et al. (2016) to be the AGN. Another X-ray source, brighter (in some epochs) and spectrally

hard, without a radio counterpart, was suggested to be a high-mass X-ray binary. The weaker X-ray source coincident with the radio source had an X-ray luminosity $L_{0.3-10\mathrm{keV}} \sim 10^{38}$ erg s^{-1}. Reines et al. (2016) fit the X-ray spectrum of the nuclear source with a power-law, and a thermal plasma model (`apec`), but their spectral fitting did not discriminate between the models. We argue below that their choice of spectral binning lost information, thus preventing clear discrimination between these models.

Recently, Cresci et al. (2017) performed MUSE (Multi Unit Spectroscopic Explorer) integral field spectroscopy on this portion of Henize 2–10. They found that the optical emission line ratios of gas in the central region of Henize 2–10 were consistent with starburst models, with no indication of AGN ionization. They also show that the revised X-ray luminosity, and X-ray/radio flux ratio, of the candidate AGN identified by Reines et al. (2016) are consistent with those of young SNRs.

NGC 4178

NGC 4178 is an SB(rs)dm galaxy with an `HII` nucleus (Ho et al. 1997) and Hα emission similar to a star-forming galaxy (Koopmann and Kenney 2004). This dwarf galaxy ($M_* = 1.3 \times 10^{10}$ M$_\odot$; Ho et al. 1997) is highly inclined ($i \sim 70$ deg) and located at a distance of 16.8 Mpc (Tully and Shaya 1984) in the Virgo cluster. Satyapal et al. (2009) argued for the existence of an AGN in NGC 4178, based on the high mid-IR luminosity observed in a [Ne V] line ($L_{14.32\mu\mathrm{m}} = 8.23 \times 10^{37}$ erg s^{-1}), using the arguments of Abel and Satyapal (2008). Secrest et al. (2012) used a *Chandra* X-ray observation of NGC 4178 to identify an X-ray source corresponding to the IR source. However, the observed luminosity of the X-ray source is about five orders of magnitude less than that expected based on the [Ne V] luminosity. They postulated that this could be due to strong absorption in the nucleus. Secrest et al. (2013) did not detect any optical signature of an AGN in Gemini observations. Thus, the X-ray emission

and strong [Ne V] emission are the only evidence for an AGN in this galaxy.

In this paper, we scrutinize the X-ray spectra of the candidate AGN in Henize 2–10 and NGC 4178 to test whether these candidate AGN may be better explained as SNRs. In § 3.2, we describe how we obtained X-ray spectra of the candidate AGN in Henize 2–10 and NGC 4178. § 3.3 compares various models fit to the observed X-ray spectra. We demonstrate that minimally-binned spectral analysis can robustly identify strong X-ray spectral lines, which can be helpful in discriminating between AGN and SNRs.

3.2 Observations and data reduction

We used the high-resolution *Chandra* X-ray observations of Henize 2–10 in February 2015 (ObsID 16068, PI: Reines; Reines et al. 2016)) and of NGC 4178 in February 2011 (ObsID 12748, PI: Satyapal; Secrest et al. 2012)) to study these X-ray sources. Both observations were taken using the ACIS-S instrument, in the VFAINT mode and FAINT mode, respectively.

We used CIAO version 4.9 (Fruscione et al. 2006) for the data reduction and the construction of the X-ray spectra. We reprocessed the initial data according to CALDB 4.7.6 standards using the `chandra_repro` command. We set the `check_vf_pha` parameter to "no" to prevent the removal of any good events. The default option of the `pix_adj` parameter uses the EDSER algorithm (Li et al. 2004), which results in more precise sub-arcsecond resolution. We constructed X-ray spectra using the `specextract` command, which produces effective area files corrected for the fraction of the point spread function extracted in the spectrum. We used the energy interval 0.3–10.0 keV for our analysis.

Because of the low photon counts, grouping these spectra with 15 photons in each bin would provide an inadequate number of bins to constrain different models. Such spectra would also not resolve any narrow features that might exist in the spectrum. Thus, we regrouped the spectra using the `dmgroup` command

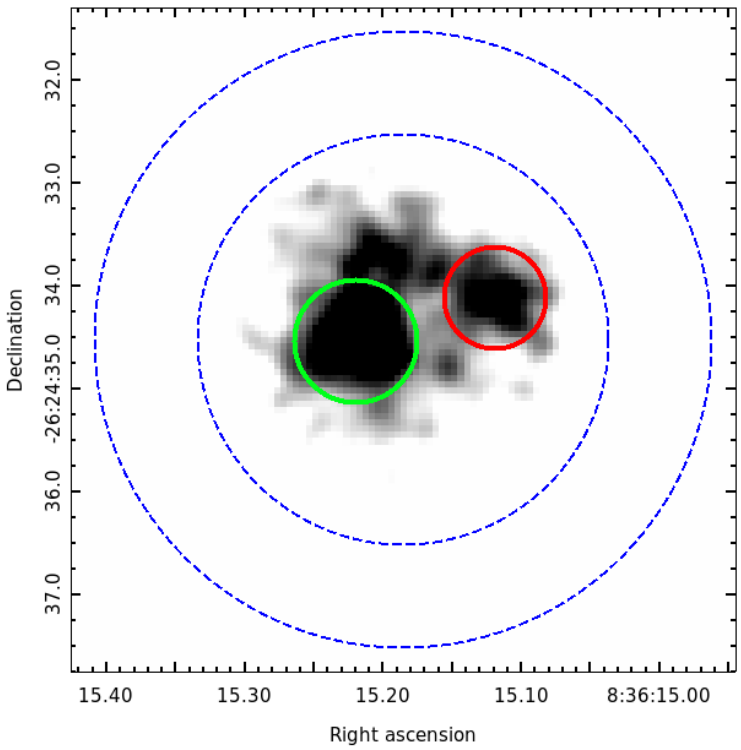

Figure 3.3: *Chandra* 0.3-10 keV X-ray image of the candidate AGN in Henize 2–10, overbinned to $1/8^{th}$ of the ACIS pixel size, and smoothed with a Gaussian of FWHM= 0.″25. The 0.″5 source region (red) captures 207 photons. We also show the bright source to the east of the candidate AGN. The 0.″6 circular region (green) around this source encloses 356 counts.. The background region, shown between two dashed blue circles of radius 2″ and 3″, contains 598 photons.

such that each group included at least 1 photon. The spectra generated were analyzed using XSPEC version 12.9.1m, using the C-statistic (Cash 1979) modified to deal with backgrounds, which can handle few to no counts per bin (note that binning to keep 1 count/bin is recommended[2]).

3.2.1 Henize 2–10

The central region of Henize 2–10 is extremely compact with multiple X-ray sources within a 2″ region, plus three other clear X-ray sources within a 50″ region. The X-ray image of the central region of Henize 2–10 is dominated by

[2] https://heasarc.gsfc.nasa.gov/xanadu/xspec/manual/node304.html

diffuse emission and a highly variable off-nuclear hard X-ray source suggested by Reines et al. (2016) to be a high-mass X-ray binary (HMXB). However, the likely HMXB was not visible in the 160 ks 2015 observation of Henize 2–10 used here. Thus, there was relatively less contamination of the weak X-ray source and candidate AGN, compared to the other X-ray observations of Henize 2–10 (The HMXB, which is $0\farcs7$ from the candidate AGN, was ~ 10 times brighter than our source in the remaining observations.). To clearly resolve the candidate AGN from the nearby diffuse emission and select the source region, we re-binned the image to $1/8^{\rm th}$ of the ACIS-S pixel size and convolved this image with an FWHM= $0\farcs25$ ($\sigma \approx 0.44$ pixels) Gaussian kernel using the `aconvolve` command (see Fig. 3.3). We extracted X-ray photons from a $0\farcs5$ circular region centred on this X-ray source ($\alpha = 8^{\rm h}36^{\rm m}15.^{s}13$; $\delta = -26°24'34\farcs08$). This radius was chosen to encompass the maximum source photons while minimizing photons from the diffuse emission around the nuclear source. We selected background photons from an annulus of radius 2–3″, excluding the bright diffuse emission directly east of the AGN candidate.

3.2.2 NGC 4178

The sub-arcsecond angular resolution of the *Chandra X-ray Observatory* clearly resolves the nuclear X-ray source from nearby bright X-ray sources (see Fig. 3.4). We selected a circular region of 1″ around the source ($\alpha = 12^{\rm h}12^{\rm m}46.^{s}32$; $\delta = +10°51'54\farcs61$) to collect the source photons. We used a 10″ region nearby, lacking bright X-ray sources, for the background.

3.3 Results and discussion

In each fit, we calculated the best-fitting parameters using the C-statistic (§ 1.4.2, as the fit statistic (e.g. "statistic cstat" in XSPEC), with correction for

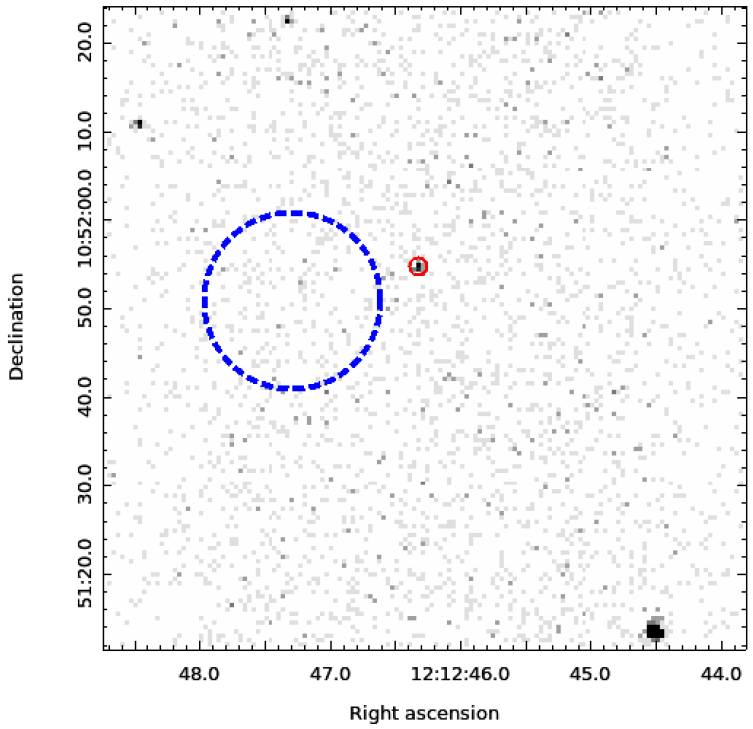

Figure 3.4: *Chandra* 0.3-10 keV image of the candidate AGN in NGC 4178. The red circular region of radius 1″ contains 39 photons. The background circular region (dashed blue circle of radius 10″) contains 189 photons.

background subtraction, aka the "W-statistic"[3]. To evaluate the relative quality of different models, we used the AICc statistic (refer § 1.4.3 for details). We also used XSPEC's "goodness" simulations to calculate the quality of individual fits. For these simulations, we used the CvM statistic (refer § 1.4.4 for detailes; e.g. we set "statistic test cvm" in XSPEC).

For both sources, we chose a simple absorbed power-law spectrum for an initial fit, and when that proved inadequate to explain the emission features (based on the quality of the fit), moved on to use hot thermal plasma models. For modelling photoelectric absorption, we used the `tbabs` model with typical interstellar (*wilm*) abundances (Wilms et al. 2000). For both sources, we found that the hot plasma models explain the observed spectra better than a simple power-law. The results of our spectral fitting are summarized in Tables 3.1

[3] https://heasarc.gsfc.nasa.gov/xanadu/xspec/manual/node304.html

& 3.2. For easy visualization, the plotted spectra of Henize 2–10 and NGC 4178 in this paper were re-binned such that each bin had four and three counts, respectively. We also tested the effects of modelling the background for the Henize 2–10 candidate AGN, rather than subtracting it. As the background makes only a small ($\sim 10\%$) contribution to the source flux, we found negligible differences in the fits that we tested, with all fitted parameters lying within the errors found with background subtraction.

3.3.1 Henize 2–10

From Fig. 3.3, we see that there is another bright X-ray source to the east of our candidate AGN, even in ObsID 16068. However, the convolved image showed that the X-ray emission from the two sources are distinct and clearly resolved by *Chandra*. We analyzed the X-ray flux from this eastern source in later sections. We binned the ~ 200 photons observed from the candidate AGN into ≈ 96 bins, each with one or more count per PHA (energy) bin. The minimum N_H was fixed to 9.1×10^{20} cm^{-2} to account for Galactic absorption in the direction of Henize 2–10 (Kalberla et al. 2005). Fitting an absorbed power-law (`tbabs*pegpwrlw`) to the spectrum gives $\Gamma = 2.7^{+0.5}_{-0.5}$ and $N_H = 2.3^{+1.7}_{-1.4} \times 10^{21}$ cm^{-2}, consistent with the spectral fit found by Reines et al. (2016). This fit is shown in Fig. 3.5, achieving a C-statistic of 131.47. We created 10^5 realizations of the power-law spectrum using the `goodness` command and found that $\sim 99\%$ of them had a lower CvM statistic than the data. This indicated that a simple power-law was a poor description of the observed spectrum.

In Fig. 3.5, we can see that the power-law model predicts the overall trend in counts versus energy, but fails to explain several narrow features clearly visible by eye in the observed spectrum. On studying the residuals, we observed that the higher counts at ≈ 1.3 keV and ≈ 1.9 keV aligned with the Kα emission lines of Mg and Si. The overall shape of the spectrum, with evidence of strong lines near 1.0, 1.3, 1.9, and (perhaps) 2.5 keV is reminiscent of the spectral

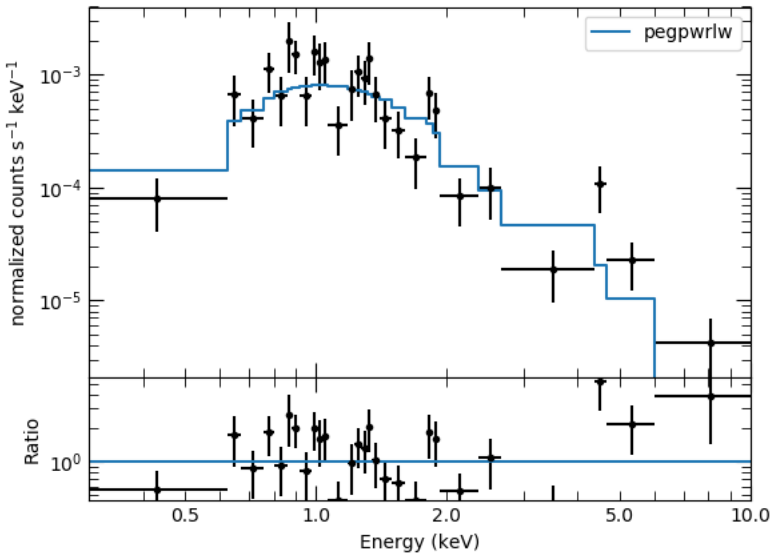

Figure 3.5: Power-law fit to the X-ray spectrum of the candidate AGN in Henize 2–10, with $\Gamma = 2.7^{+0.5}_{-0.5}$ and $N_H = 2.3^{1.7}_{-1.4} \times 10^{21}$ cm^{-2}. The C-statistic is 131.5 for 3 free parameters (93 d.o.f). Though the fit can explain the overall shape of the spectrum, it fails to model the observed narrow features.

shapes of SNRs, with lines around those energies due to Ne and/or Fe, Mg, Si, and S, respectively (e.g. Cas A SNR: Holt et al. 1994; Hughes et al. 2000a; Tycho SNR: Badenes et al. 2006; SNR 1987A: Michael et al. 2002). There also appeared to be a feature at ~ 4.5 keV, which we have discussed below.

As a first step, we modelled the spectrum with an absorbed power-law plus Gaussians at the locations of strong residuals (Fig. 3.6). We found that four lines were strongly required. Narrow ($\sigma < 0.1$) lines were required at $1.31^{+0.02}_{-0.04}$ keV (associated with Mg XI Kα, lab energy 1.33 keV[4]), $1.85^{+0.06}_{-0.05}$ keV (associated with Si XIII Kα, lab energy 1.83 keV), and 4.56 ± 0.11 keV, which does not have an immediately obvious nature. A broad ($\sigma = 0.18^{+0.09}_{-0.06}$ keV) emission feature is also required at $0.78^{+0.06}_{-0.22}$ keV, which may be explained by a combination of O VIII (0.65 keV), Ne IX Kα (0.91 keV), and/or Fe L-shell (covering roughly 0.8–1.1 keV). When we added these four Gaussians to the power-law model,

[4] http://www.atomdb.org/Webguide/webguide.php

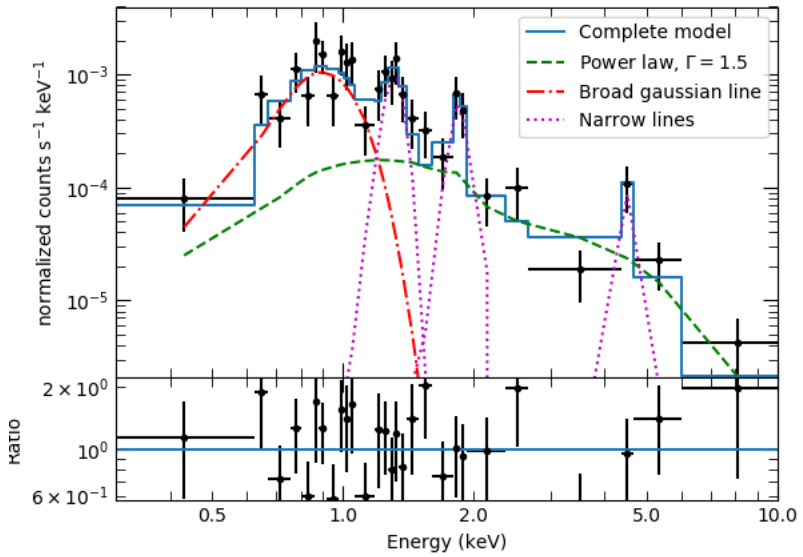

Figure 3.6: X-ray spectrum of the AGN candidate in Henize 2–10, here modelled with four Gaussian emission lines added to a power-law continuum. The broad line at 0.8 keV may be due to the Kα lines of O and Ne, along with Fe-L lines. The narrow lines at 1.3 & 1.8 keV correspond to Kα lines of Mg and Si, respectively. The nature of the narrow 4.5 keV line is unclear. This figure shows strong evidence for multiple emission lines in this X-ray spectrum.

the C-statistic dropped by ~ 45 with 10 fewer degrees of freedom. Comparing the AICc statistics (Table 3.1) for the power-law fit, vs. the fit including four Gaussians, indicated that the latter was preferred by a factor of $\sim$37,000.

These strong emission lines suggested thermal plasma at low temperatures and/or high abundances, consistent with thermally emitting ejecta from an SNR. We, therefore, attempted to fit the spectrum of the Henize 2–10 AGN candidate with self-consistent physically motivated thermal plasma models, beginning with a simple collisionally ionized model.

The `apec` model has a single parameter for all metal abundances. Since there was no strong Fe K emission line in our spectrum (e.g. at 6.7 keV), the single `apec` model failed to fit the observed emission lines of Mg and Si. Thus we employed the `vapec` model that allows fits to individual relative abundances of metals. We allowed the abundances of O, Ne, Mg, Si, and S to

vary relative to solar values, since these are the abundant elements with strong lines in the observable spectral range. Fitting an absorbed collisionally ionized plasma emission model (`tbabs*vapec`) gave $kT = 2.5^{+0.9}_{-0.8}$ keV and preferred high abundances of O (176^{+824}_{-169}) and Ne (190^{+810}_{-175}), with Si (5^{+995}_{-5}), S (7^{+228}_{-7}), and Mg (0^{+249}_{-0}) abundances basically unconstrained. Since the errors on the relative abundances of Mg, Si and S were large and consistent with solar abundances, we fixed the abundance of these elements to solar (1). Fitting the X-ray spectrum with this constraint gave $N_H = 9^{+15}_{-0} \times 10^{20}$ cm^{-2}, $kT = 2.5 \pm 0.9$ keV, and super-solar abundances of O and Ne (~ 1000). The spectrum matched the observed features with Kα emission lines of O and Ne. Despite having two additional parameters in comparison to an absorbed power-law model, the C-statistic decreased only marginally (by 6.47). Thus, though this fit was not a statistically significant improvement over the power-law model. We also performed "goodness" simulations using 10^5 realizations of the model to test the quality of the fit. Due to the large error-bars in the abundance parameters, we used the "`nosim`" option in the `goodness` command in XSPEC for our simulations. Similar to the absorbed power-law spectra, we found that $\sim 99\%$ of the realizations had a lower CvM statistic confirming that a single temperature hot plasma model is a poor fit to the observed spectrum. Also, the high relative abundance of O and Ne with respect to Mg and Si seemed unphysical.

The low abundances of Mg & Si in this fit seemed unlikely, due to the apparent emission lines near the Kα energies of Mg XI and Si XIII. Adding Gaussian emission lines, with $\sigma = 0.01$ keV, at energies 1.31 & 1.85 keV decreased the C-statistic by ~ 14 while decreasing the degrees of freedom by 4. The change in the AICc values indicated that adding these Gaussian lines increased the likelihood by ~ 20. The data thus suggested that these lines are real, but that the single-temperature plasma model did not get their energies correct.

Another way of showing the statistical significance of these lines is by looking at the probability of obtaining the observed number of counts in these energy

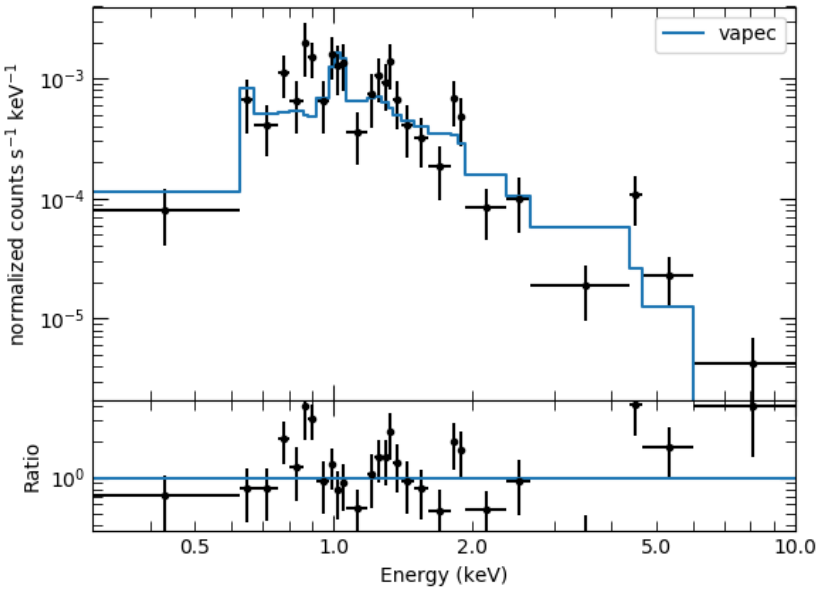

Figure 3.7: X-ray spectrum of the AGN candidate in Henize 2–10, here modelled by an absorbed collisionally ionized plasma emission model with a single temperature, $kT = 2.5^{+0.9}_{-0.9}$ keV. The model fits the emission features of O and Ne well, but fails to fit other narrow spectral features that are suggestive of emission from Mg, Si, and S.

ranges, given the spectral fit to the remainder of the spectrum. While the single temperature hot plasma model predicted a total of 26.4 photons in the energy ranges 1.2-1.4 and 1.75 - 1.95 keV, the data showed 46 photons in these bins. Assuming a Poissonian distribution, this has a single-trial probability of 0.2%.

The single-temperature model predicted the Mg Kα line to be at slightly higher energies ($\sim$ 1.47 keV) than observed (1.31 keV). At the required temperature to explain the high-energy photons as bremsstrahlung, the Mg will be principally in Mg XII, which has a Kα line at 1.47 keV, rather than the observed 1.31 keV better fit by Mg XI. Thus, a lower temperature plasma could match the observed Mg emission line, but would not explain the observed continuum emission at higher energies. We considered three models to address this problem.

First, we considered a two-temperature plasma to model the observed

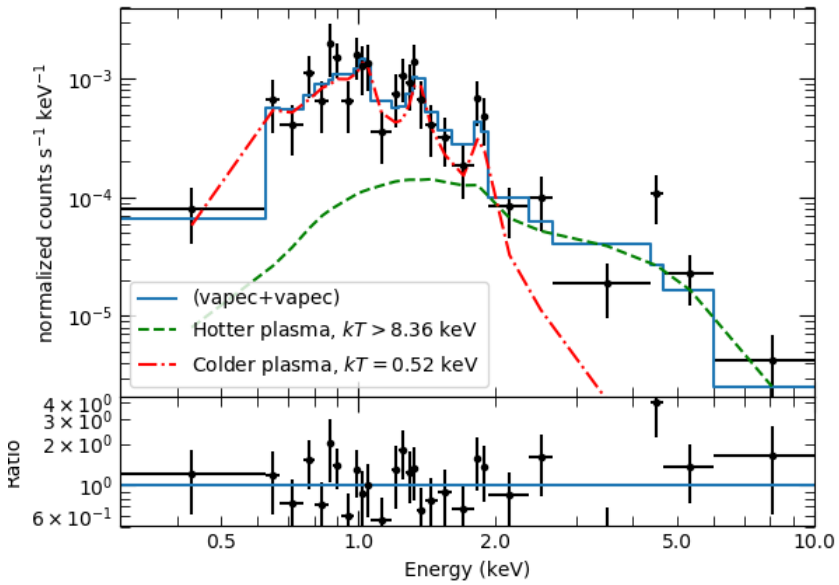

Figure 3.8: X-ray spectrum of the AGN candidate in Henize 2–10, here modelled by an absorbed collisionally ionized plasma model with two different temperatures, $kT > 8.4$ keV & $kT = 0.5^{+0.3}_{-0.1}$ keV . We find super-solar abundances of O, Ne, Mg, Si ($= 11^{+24}_{-7}$) . This model captures the continuum emission as well as all the emission features, except the one at ~ 4.5keV.

spectrum (`tbabs*(vapec+vapec)`). Similar models have often been used to model SNR emission, and have been suggested to indicate cooler emission from the reverse shock and hotter emission from the blast wave (e.g. Jansen et al. 1988; Willingale et al. 2002). To minimize the number of free parameters, we only allowed the abundances of the (measurable) elements O, Ne, Mg & Si to vary. When fitting this model, we saw that the error bars in the abundances of these four elements overlap. Given that O, Ne, Mg, and Si are α-group elements, we expect their abundance to be similar. Numerical simulations of supernovae with progenitor masses from 9 to 120 $M_\odot$ in Sukhbold et al. (2016) also show that the relative abundance ratios of these elements with respect to Si are $\sim O(1)$. Since the errors on the abundance values are large in our case, we linked the abundances of O, Ne, Mg, and Si in both plasmas. This model gave $N_H = 2.7^{+2.8}_{-1.8} \times 10^{21}\mathrm{cm}^{-2}$, $kT = 0.52^{+0.24}_{-0.11}$ for the cold plasma and $kT \geq 8.36$ keV

for the hot plasma (see Fig. 3.8). We found the relative abundances of the linked elements O, Ne, Mg, Si and S to be 11^{+24}_{-7} times solar. This model is shown in Fig. 3.8. The Fe abundance preferred to be smaller than the abundances of O, Ne, Mg, Si & S. Fixing the abundances of O, Ne, Mg, & Si to 11.0, we constrain the Fe abundance to be $1.0^{+1.08}_{-0.85}$. Compared to the absorbed power-law model, the C-statistic have decreased by 31.82 while the degrees of freedom only decreased by 5. Thus, the AICc value decreased by 24.84, implying that this model was $\sim 2.5 \times 10^5$ times more likely. The "goodness" simulations showed that $\sim 59\%$ of the realizations had a lower CvM statistic than the observed data, showing that this model was a good fit to the observed data.

The lower ionization state of Mg & Si could also be explained by a plasma that is not yet in ionization equilibrium, as is often the case in young SNRs. A `vnei` model with a lower ionization time-scale (The ionization time-scale to attain equilibrium at 10^7 K is $\sim 10^{11} - 10^{12}$ s cm^{-3} for Mg and Si; Smith and Hughes 2010) could explain the continuum emission at higher energies, while explaining the low-ionization emission lines of Mg and Si. The relative abundances of O, Ne, Mg & Si were linked together as in the previous models. When fitting this model, we found $N_H = 5.9^{+1.8}_{-2.2} \times 10^{21}$ cm^{-2}, $kT > 22$ keV and ionization time-scale $\tau = 1.6^{+1.1}_{-0.7} \times 10^{10}$ s cm^{-3}. The ionization time-scale is similar to that of the young SNR Cassiopeia A (Willingale et al. 2002). Though we found the abundance of O, Ne, Mg, and Si to be consistent with solar values within their error limits ($1.7^{+1.2}_{-0.7}$), the low ionization time-scale of this model argued for the X-rays being generated by an SNR, rather than an AGN. This model had similar AICc and CvM statistic values as the two-temperature plasma model, suggesting that both models were equally likely.

The emission at higher energies could also be due to synchrotron emission from a PWN (e.g. Crab nebula Hester 2008) or synchrotron-dominated shocks (e.g. SN 1006 Koyama et al. 1995). Synchrotron spectra can typically be modelled using a power-law component (§ 1.1.4). Thus we also tried fitting a

`tbabs*(pegpw + vapec)` model to the observed spectrum. Though the best-fitting model did indicate super-solar abundances, the power-law component was very hard ($\Gamma = 0.4^{+1.1}_{-1.3}$). Using $\Gamma = 2.7$ (typical of forward shocks in SNRs; eg. Torii et al. 2006; Tamagawa et al. 2009), gave a poorer fit (the "goodness" exceeded 95%, indicating a poor fit). Thus, synchrotron emission from shocks in an SNR did not appear to explain the flux at higher energies well.

The observed X-ray spectrum also showed an increase in the photon count rate at 2.6 keV, which is very close to the Kα emission line of S XVI (2.62 keV). This could be incorporated into the `tbabs*(vapec+vapec)` model by allowing for an increased abundance of S in the hot plasma. Linking the abundance of S in both plasmas brought its abundance down since there were no emission corresponding to the expected S XV line that should be produced by the plasma at the lower temperatures. Allowing the abundance of S in hotter plasma alone gave an abundance of ~ 1000 while reducing the C-statistic by 4.79 and decreasing the d.o.f by 1 (i.e. slight improvement in AICc statistics; ~ 3 times more likely). Similarly, a higher ionization time-scale of S in the `vnei` model ($\sim 10^{13}$ s cm^{-3}) could also account for the relative over-abundance of S XVI as compared to S XV. Understanding why S behaves differently from the other elements requires further observations.

4.5 keV feature?

The apparent emission feature at ~ 4.5 keV could not be explained by any of the above models. There were 6 photons between 4.4–4.7 keV, corresponding to a count rate of 3.75×10^{-5} counts/s. This is a small number of counts and our $0\farcs5$ extraction region should have only captured 60% of the 4.5 keV point-spread function. Nevertheless, the line appeared significant (as we show below), and we are unaware of any calibration issue that would generate a spurious emission line at this energy. We used the `flux` command in XSPEC to calculate the total flux in the interval 4.4–4.7 keV and determined the predicted number of

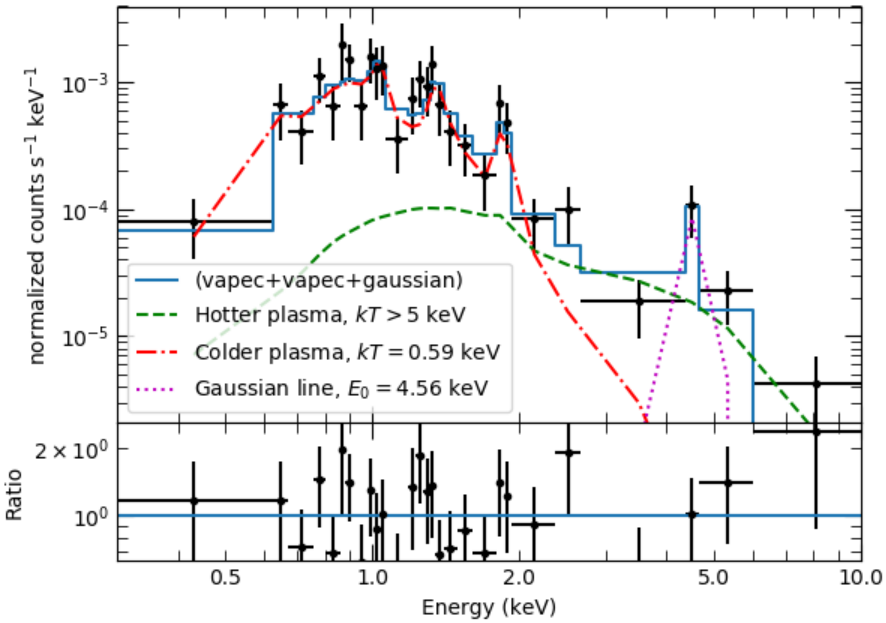

Figure 3.9: X-ray spectrum of the AGN candidate in Henize 2–10, here modelled with a Gaussian emission line at 4.6 keV added to the two-temperature plasma. Since the C-statistic decreases by ~ 10 on addition of the Gaussian, it might indicate a real feature.

photons using the exposure time ($= 1.59 \times 10^5 s$) and effective area of *Chandra* ACIS-S at 5 keV ($= 400$ cm^2). The model with two collisionally-ionized plasmas, for example, only predicted $1.23^{+0.23}_{-1.0}$ counts. Therefore we chose to further investigate the presence of an emission feature at this energy. This feature is consistent with the energy of the Kα emission line of Ti, but the very high abundance of Ti needed (~ 1000) seems extremely improbable. We added a Gaussian with $\sigma = 0.1$ and line energy constrained between 4.4–4.7 keV to the two-temperature plasma model. Adding the Gaussian greatly improved the fit ($\Delta\mathrm{cstat}_{\mathrm{2vapec}}/\Delta\mathrm{d.o.f}_{\mathrm{2vapec}} = 8.87/-2$), as shown in Fig. 3.9 and Table 3.1. We found that $kT > 5$ keV for the hot plasma, $kT = 0.59^{+0.20}_{-0.16}$ keV for the cold plasma and the (linked) abundances of O, Ne, Mg, Si & S to be 11^{+46}_{-7}. From the C-statistic value ($= 90.95$) and the number of parameters ($= 8$), we calculated the AICc value to be 108.44. Comparing this to the AICc value of our two

temperature model without the Gaussian (= 112.59), we observed that adding a Gaussian at $\sim$ 4.5 keV increased the likelihood that the fit explained the data by a factor of $\sim$ 8. If we treat ΔC-statistic as a $\Delta\chi^2$-statistic (since both are logarithms of likelihood ratios), using the $\Delta\text{cstat}_{\text{2vapec}}$ & Δd.o.f observed, we have a 1.2% probability of getting this statistical improvement by chance. Adding a Gaussian to the partially ionized hot plasma model gives similar results, with $\Delta\text{cstat} = 10.1$ while decreasing the degrees of freedom by 2.

The potential presence of this line raises a critical question: are any similar lines observed in other SNRs? A faint emission line of Ti has been observed in Tycho's SNR at 4.7 keV (Miceli et al. 2015), but the 3.9 keV Ca Heα line (undetectable in our data) is at least 240 times stronger (measured by equivalent width) in that SNR. An alternative scenario is that the line could be the $\sim$ 3.9 keV Ca line, blue-shifted by $\sim$ 10% of c. This would require that the Ca-emitting part of the remnant is moving at extreme speeds unusual in SNRs, and uniformly in our direction — both of which seem unlikely. We conclude that the nature of this candidate line remains unclear.

Nearby X-ray emission in Henize 2–10

We also analyzed the X-ray spectrum of the diffuse X-ray emission 1″ east of the candidate AGN in Henize 2–10 (shown in the green circle in Fig. 3.3), for comparison. We found that the X-ray spectrum of this eastern source was similar to our candidate AGN, with strong O, Ne, Mg, and Si Kα emission lines. Therefore, we used our two-temperature hot plasma model to explain the X-ray emission from this source. Fitting this model to its X-ray spectrum gave $N_H = (7 \pm 5) \times 10^{21}$ cm^{-2}, $kT_{\text{hot}} = 1.9^{+1.1}_{-0.6}$ keV, $kT_{\text{cool}} = 0.30^{+0.33}_{-0.12}$ keV, and the relative solar abundance of O, Ne, Mg & Si to be 3^{+4}_{-2}, i.e., only marginally super-solar. Fig. 3.10 compares the spectra of these two X-ray sources in Henize 2–10. From Fig. 3.10, and the values of the best-fitting parameters, we noted that though these sources had broadly similar spectra, the X-ray

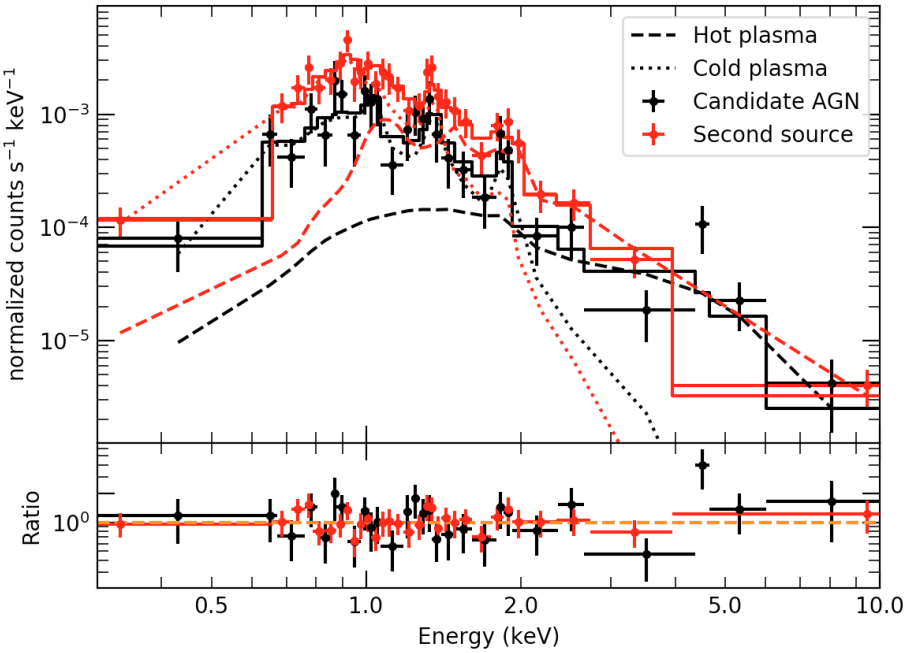

Figure 3.10: Comparison between the spectra of the two X-ray sources in Henize 2–10. The dashed and the dotted lines show the contribution of hot and cold plasma respectively. We find that the X-ray spectrum of the candidate AGN is slightly harder, and has a higher required metallicity, and shows stronger emission around 4.5 keV, than to the other source.

emission from the candidate AGN in Henize 2–10 was both harder and required a higher abundance of O, Ne, Mg & Si compared to the diffuse emission. These differences helped us investigate the nature of the differences between the two X-ray sources.

We first noted that the contribution from this diffuse source to the spectrum of the candidate AGN was minimal. From Fig. 3.3, we see that the two sources are separated by $> 1''$. A $1''$ radius encloses 84 (91)% of the point-spread function for photons of 6.5 (1.5) keV. Some particular points of interest in the candidate AGN's spectrum — the low-energy emission lines, the hard component, and the 4.5 keV possible line — were all stronger in the candidate AGN than the diffuse eastern source, clearly indicating that none of them were produced by contamination from the eastern source.

The similarities and differences between the two spectra suggested that the

candidate AGN was likely produced by a single young SN, while the diffuse eastern source was produced by multiple, older SNRs. The eastern source's larger spatial extent would thus arise from multiple sources, while the candidate AGN is consistent with a point source. The higher-temperature spectrum of the candidate AGN suggested a faster expansion speed, typical of younger SNRs. Similarly, the higher metallicity was consistent with less mixing of ejecta with the circumstellar and interstellar medium. This picture was consistent with the VLBI size constraints upon the radio source, which must be several times larger than 0.1 pc (Ulvestad et al. 2007), but not much larger than 1.3 pc (Reines and Deller 2012, cf. their resolving a larger SNR to the NE with VLBI). In this picture, the candidate AGN is actually a young SNR that is less than 100 years old and is extremely luminous in the radio and X-ray, 4 and 3 times brighter than Cas A in these bands (e.g. Ulvestad et al. 2007; Ou et al. 2018).

Variability of Henize 2–10

Reines et al. (2016) identified evidence for (likely) periodic variability in the X-ray light curve of Henize 2–10. This evidence did not come from a signal in a standard periodicity search (e.g. a power spectrum). Instead, a sinusoidal model (with period 33.5 ks) was statistically favoured compared to a constant rate model (at the 3.8σ level), as measured with the F-test (typically used to compare spectral models). In addition, the amplitude of the fitted sinusoid was non-zero at 3.9σ significance. Should significant variability on short timescales be confirmed, it would require a source of X-ray emission other than an SNR. For instance, a slow-spinning X-ray luminous magnetar within the SNR, similar to the one in the SNR RCW 103 (A. de Luca et al. 2006; Rea et al. 2016; D'Aì et al. 2016) could explain such variability.

However, the methods used to verify variability by Reines et al. (2016) do not appear to account for the number of trials used to search for the correct period, phase, and amplitude of the sinusoidal fit. Thus they may be less

statistically significant than claimed. The F-test is also designed to be used with Gaussian, not Gehrels, errors. We, therefore, investigated the evidence for variability using several methods and performed Monte Carlo testing to directly measure the statistical significance of nonstandard tests for variability. For all timing analyses, we first barycentre-corrected the events file using the position of the target source.

Our first variability check used the Gregory-Loredo variability test algorithm implemented in the `glvary` tool of CIAO (Gregory and Loredo 1992)[5]. This algorithm has been designed to search for periodic, variable signals, such as the one suggested here, as well as non-periodic variability. Running this tool on the unbinned event file returned `VAR_INDEX` $= 0$, the lowest variability index, indicating no evidence for variability in the X-ray emission.

We also calculated the Leahy normalized power spectral density (PSD, Leahy et al. 1983) to check the significance of the reported period, using the `powspec` tool in FTOOLS. We used the minimum time resolution of ACIS, 3.14101 s, to construct background subtracted light curves to calculate the power-spectra. The PSD values at $P = 29.4$ ks and $P = 34.3$ ks were 7.68 and 10.44 respectively. We found that there are 173 out of the 51648 frequencies in our spectra that have PSD values greater than or equal to 10.44 (and 700 values greater than 7.68). Thus, the PSD value at the frequency reported by Reines et al. (2016) does not appear to be significant. This is in agreement with Reines et al. (2016), who found a less than 2σ significance for their claimed signal from a power spectral analysis. In sum, we do not see any evidence for this potential periodicity in these standard statistical tests.

We performed Monte-Carlo simulations to understand the significance of the difference in χ^2 between the constant and sinusoidal fits, as well as the ratio of the amplitude of the sinusoidal model to its error, reported by Reines et al. (2016). We first binned the data using a bin time of 5 ks (following Reines et al.

[5] http://cxc.harvard.edu/csc/why/gregory_loredo.html

2016) and fit the data using constant and sine models. We used Gehrels errors for the fitting. The best fitting constant model gave 4.7 ± 0.6 counts per bin and $\chi^2 = 19.25$ for 32 degrees of freedom, similar to Reines et al. (2016) who reported $\chi^2/\nu = 18.4/32$. The sinusoidal model gave best fitting values of the amplitude, $A = 2.5 \pm 0.9$ counts/bin, and period, $P = (3.2 \pm 0.1) \times 10^4$ s, with χ^2/d.o.f = 11.39/29 for the best fitting sine model. This was slightly larger than the fit value from Reines et al. (2016), χ^2/ν=9.2/29; the difference might be due to different background subtraction.

We then simulated 10^4 realizations of 180 photons uniformly emitted over the observed time of 160 ks and binned these realizations using the same bin time of 5 ks. We fit each of these realizations with constant and sinusoidal models using the PYTHON SCIPY `curve_fit` function (Jones et al. 2001). To ensure that we identify the best fitting sine model, we explored ten different values of period and five values of amplitude as the initial parameters for fitting each realization, and chose the best fitting model with the smallest χ^2 values for each. We found that 14% of the random realizations have $\chi^2 >= 19.25$ for the constant fit. We also checked what fraction of our realizations showed a ratio $A/\sigma_A >= 2.8$ (i.e., that the amplitude of the sinusoidal signal was detected at 2.8σ confidence, as in the data). Finally, we checked the fraction of the random realizations that showed improvements in the sinusoidal fit compared to the constant fit that were stronger than that found for our source (i.e., $\chi^2_{\rm const} - \chi^2_{\rm sin} > 7.86$). We found that 3% of our simulations satisfied both the conditions on the ratio of amplitudes and the difference in χ^2 (The fraction of realizations satisfying either of the above conditions was also around 3%, as typically these conditions occurred together.). We thus found that the probability of a non-variable light curve producing a signal of this strength was 3% i.e. moderately significant — above 2σ, but not above 3σ. Although this possible signal was interesting, we did not feel that it was robust enough to rule out the non-variable SNR interpretation of this X-ray source.

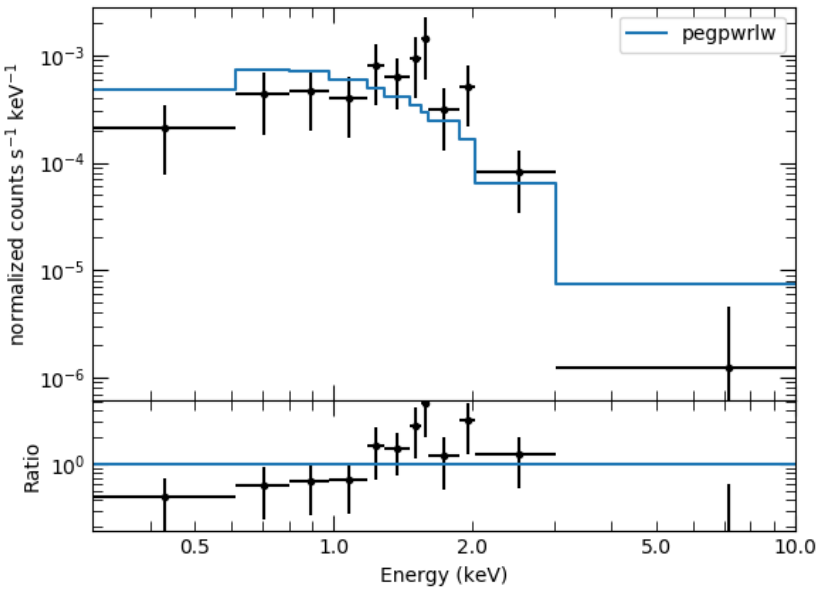

Figure 3.11: X-ray spectrum of the candidate AGN in NGC 4178, fit with a partially-covered power-law model as in Secrest et al. (2012), but with finer binning; $N_H = 5 \times 10^{24}\mathrm{cm}^{-2}$, covering fraction $f = 0.99$, and $\Gamma = 2.3$. The C-statistic for this model is 43.27. The residual plot (below) shows that this model predicts an excess of photons at both lower and higher energies, compared to the observed data.

3.3.2 NGC 4178

We analyzed the 36 photons from the candidate AGN in NGC 4178 using similar methods. Secrest et al. (2012) uses a partially absorbed power-law model with $N_H = 5 \times 10^{24}\mathrm{cm}^{-2}$, a covering fraction $f = 0.99$, and $\Gamma = 2.3^{+0.6}_{-0.5}$ to explain the observed X-ray flux and the hardness ratio. We fit this model to the minimally binned X-ray spectra in Fig. 3.11. This model did not match the strong emission between 1.8 and 2.0 keV, and over-predicted emission above 2 keV and below 1 keV. Inspection of the residuals suggested the possibility of Si emission lines between 1.8 and 2 keV, and Mg lines around 1.4 keV, motivating a thermal plasma model.

We also checked a simpler power-law fit (`tbabs*pegpwrlw`) to the NGC 4178 X-ray spectrum, finding $N_H = 4.1^{+5.1}_{-3.3} \times 10^{21}$ cm^{-2} and $\Gamma = 2.9^{+1.4}_{-1.0}$. From

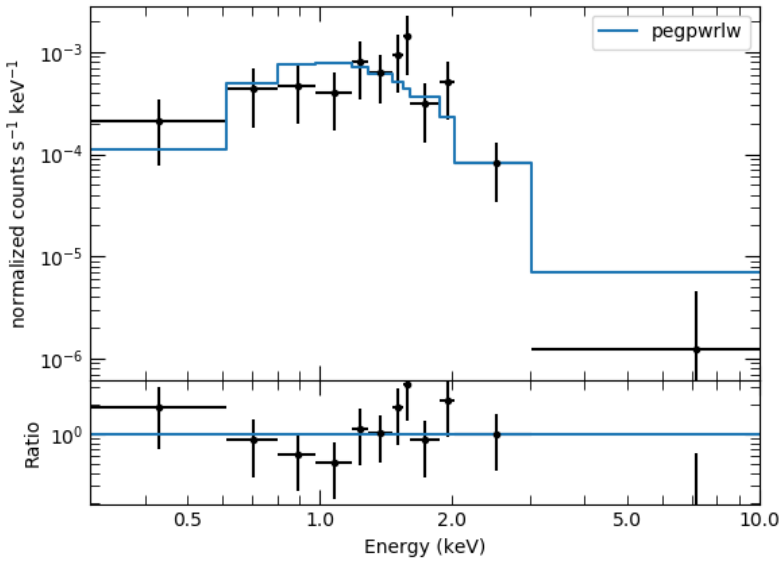

Figure 3.12: X-ray spectrum of the AGN candidate in NGC 4178, here modelled by a power-law, with $N_H = 4^{+5}_{-3} \times 10^{21}$ and $\Gamma = 2.9^{+1.4}_{-1.9}$. C-statistic = 35.3. Though this model is a better fit than the one in Secrest et al. (2012) and Fig. 3.11, it does not model the potential emission lines.

Fig.s 3.11 and 3.12, we see that neither power-law model fits the observed emission lines or rapid count rate decrease above 2 keV. The "goodness" simulations for both these models showed that a large fraction ($\sim 99\%$) of the simulated realizations have a lower CvM statistic than the data, suggesting that these fits were poor. The large magnitude of the photon index for a power-law fit also suggested a softer thermal origin of the X-ray emission.

We checked the significance of excess emission near 1.5 keV and 2.0 keV by adding Gaussian emission lines to the simple power-law, as in the previous case. These lines could correspond to the Kα emission lines of Mg XII (1.472 keV) and Si XIV (2.006 keV). Gaussian lines with $\sigma = 0.1$ produced good fits at $E_1 = 1.5 \pm 0.1$ keV and $E_2 = 2.0 \pm 0.1$ keV (shown in Fig. 3.13). These Gaussian lines reduced the C-statistic of the best fitting model by ~ 15 while decreasing the d.o.f by 4. From the AICc value of this model (39.14), we found that this model was ~ 5 times better than the simple power-law model. Running the

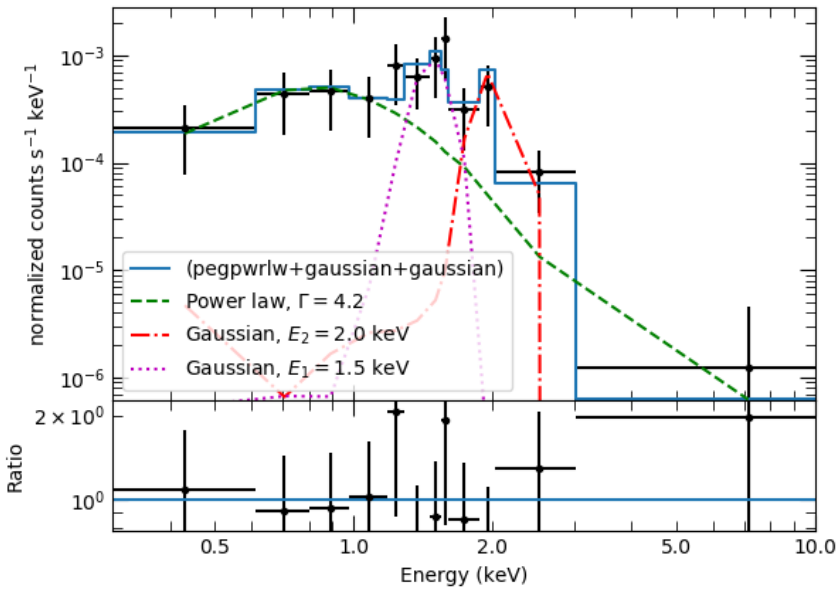

Figure 3.13: X-ray spectrum of the candidate AGN in NGC 4178, modelled by a simple power-law with two Gaussian lines, with $N_H = 3.4^{+10.7}_{-2.2} \times 10^{21}$ cm^{-2}, $\Gamma = 4^{+10.7}_{-2}$. These Gaussian lines indicate excess emission at 1.5 ± 0.1 and 2.0 ± 0.1 keV, which coincide with the Kβ emission of Mg XII (= 1.473 keV) and Si XIV (= 2.004 keV). C-statistic = 20.3.

"goodness" test with this model showed that $\sim 30\%$ of the test models had CvM values smaller than the best fitting model, indicating that the model was a reasonable representation of the data.

To explain the emission features, we tried fitting a single temperature plasma modelled by `tbabs*vapec`. Since we had very low photon counts, we link the relative abundances of O, Ne, Mg & Si, reducing the number of parameters. Fitting this model to the observed spectrum (Fig. 3.14) gives $N_H = 9^{+28}_{-7} \times 10^{20}$ cm^{-2}, $kT = 1.4^{+1.1}_{-0.4}$ keV, and super-solar abundances of O, Ne, Mg and Si (> 11). With only one additional parameter compared to the absorbed power-law fit, the C-statistic reduced by 8.3. Thus comparing the AICc values, the hot plasma model was about 17 times more probable to explain the observed spectrum, compared to the simple power-law model. The lack of photons above 2.1 keV, matching the single temperature plasma model predictions, indicated that this

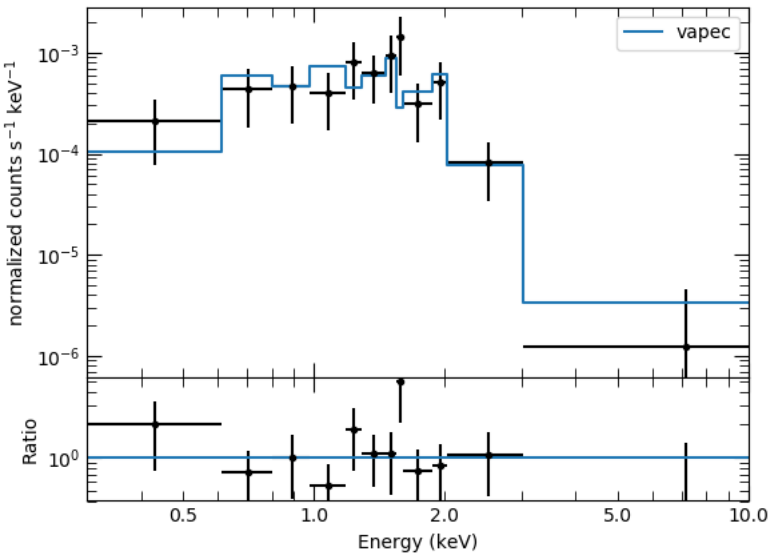

Figure 3.14: X-ray spectrum of the AGN candidate in NGC 4178, here modelled by a collisionally ionized hot plasma model, with $N_H = 9.4^{+27.6\times10^{20}}_{-7.2}$ cm^{-2}, & $kT = 1.4^{1.1}_{-0.4}$ keV. C-statistic = 26.9. This model is able to fit the narrow emission features along with the broad characteristics of the spectrum. The AICc test indicates that the likelihood of this hot plasma model is ~ 17 times larger than that of a simple power-law model.

model was sufficient to explain the observed data. The super-solar abundances of Mg and Si indicated that the X-rays from the candidate AGN in NGC 4178 could also be better explained as emission from an SNR than an AGN.

3.4 Summary and conclusions

We have used the moderate spectral resolution of *Chandra*, and the strength of emission lines in the thermal emission from SNRs, to discriminate between power-law and thermal plasma emission models in low-count X-ray spectra. Through our analysis, we argue that the X-ray sources identified as candidate AGN in Henize 2–10 and NGC 4178 are more likely to be SNRs than actual AGN.

The recent analysis of Cresci et al. (2017) argued that the optical emission

lines from the AGN candidate in Hen 2–10 indicate ionization by star formation rather than an AGN. In addition, the revision of the X-ray luminosity of the candidate AGN by Reines et al. (2016) reduces its X-ray/radio flux ratio into the regime of SNRs (Cresci et al. 2017). Thus, we find that the published evidence from optical, X-ray and radio emission does not make a compelling argument for an AGN in Henize 2–10. However, Reines et al. (in prep.; priv. comm.) argue that their newly obtained HST/STIS spectra of the AGN candidate favour LINER-like line ratios.

We find that the X-ray source identified by Secrest et al. (2012) as a candidate highly-obscured AGN does not resemble the X-ray spectrum of an obscured AGN, and instead can be well described by models for SNRs. The only remaining evidence for an AGN in NGC 4178 is the strength of the [Ne V] line (Satyapal et al. 2009), suggested to be produced by an obscured AGN. Given the lack of optical (Secrest et al. 2013) and X-ray evidence for an AGN in this galaxy, we suggest that radiative transfer simulations be performed to determine if the [Ne V] line might be produced by a young stellar population as well. Although there is no question that small AGN exist in many dwarf galaxies, our work demonstrates that X-ray emission from SNRs can be a confounding factor in searches for low-luminosity AGN.

Standard hardness ratios, as well as more sophisticated quantile analyses (Hong et al. 2004), do not take advantage of the capability of X-ray CCD spectra to resolve clear X-ray lines. We are now devising and testing general hardness ratios that can be used by X-ray CCD instruments to discriminate between strongly line-dominated and continuum-dominated spectra, even with low numbers of X-ray photon counts. Immediate applications include identifying Fe-K lines (e.g. from highly absorbed hard X-ray sources such as IGR J16318-4848, Walter et al. 2003), Fe-L lines (around 1 keV) from chromospherically active stars with soft X-ray spectra, and Si lines from SNRs.

Future X-ray and radio instruments will also permit more powerful analyses. For objects such as Henize 2–10, for instance, the *Lynx* mission (The Lynx Team 2018), with quantum calorimeter spectral resolution, high effective area, and *Chandra*-like angular resolution can provide conclusive answers. Similarly, the ngVLA (Murphy et al. 2018), with a higher effective area and longer baselines than the Jansky VLA, would resolve radio sources such as this, enabling firm identification of low-luminosity low-mass AGN (Plotkin and Reines 2018; Nyland and Alatalo 2018).

Table 3.1: Summary of spectral analysis results for the candidate AGN in Henize 2–10.

Model	Parameters	Parameter Values	Δcstat$_{pl}$/Δd.o.f$_{pl}$	AICc	log(CvM) (goodness)
`tbabs*pegpwrlw`	N_H	$2.3^{+1.7}_{-1.4} \times 10^{21}$ cm^{-2}	0.0/0	137.73	-6.32 (99%)
	Γ	$2.71^{+0.52}_{-0.46}$			
	Flux$_{\rm unabsorb}$	$1.61^{+1.10}_{-0.48} \times 10^{-14}$ ergs cm^{-2} s^{-1}			
TBABS*(PEGPWRLW + GAUSS + GAUSS + GAUSS + GAUSS)	N_H	$1.3^{+2.8}_{-0.4} \times 10^{21}$ cm^{-2} *	$-45.26/-10$	116.70	-9.37 (10%)
	Γ	$1.5^{+0.8}_{-0.9}$			
	Flux$_{\rm unabsorb}$	$4.8^{+3.7}_{-1.6} \times 10^{-14}$ ergs cm^{-2} s^{-1}			
	E_1	$0.78^{+0.06}_{-0.22}$ keV			
	σ_1	$0.18^{0.09}_{-0.06}$ keV			
	E_2	$1.31^{+0.02}_{-0.04}$ keV			
	E_3	$1.85^{+0.06}_{-0.05}$ keV			
	E_4	4.56 ± 0.11 keV			
	$\sigma_2, \sigma_3, \sigma_4$	$0.04^{+0.06}_{-0.04}$ keV			

Note: For models with `vapec` & `vnei`, the abundances of all the elements that were not specified in the table were fixed to solar values (1). The unabsorbed flux is calculated in the $0.3-10$ keV interval. The "goodness" values, below the CvM statistic values, denote the percentage of realizations of the model that have a lower CvM statistic than the data. Thus, a large "goodness" value (e.g. 99%) indicates a small (e.g. 1%) probability of obtaining such a poor fit by chance–and thus a high probability that the model is not the correct description of the data. Comparing the Δcstat/Δd.o.f and the AICc values between different models, we see that the Henize 2–10 AGN candidate is more likely to be an SNR than an AGN. The values of CvM statistic and "goodness" further confirm our results.

* Lower error bound reaches the lower hard limit.

** Upper error bound exceeds the upper hard limit.

[a] E.M stands for Emission Measure $= \int n_e n_H dV$

Table 4.1 Continued: Summary of spectral analysis results for Henize 2–10

Model	Parameters	Parameter Values	Δcstat$_{pl}$/Δd.o.f$_{pl}$	AICc	log(CvM) (goodness)
TBABS*VAPEC	N_H	$9.1^{+15.0}_{-0.0} \times 10^{20}$ cm^{-2} *	$-6.47/-2$	135.67	-6.40 (99%)
	kT	$2.45^{+0.91}_{-0.83}$ keV			
	O	960^{+40}_{-930} **			
	Ne	970^{+30}_{-940} **			
	E.M.[a]	$1.39^{+25.4}_{-0.31} \times 10^{59}$ cm^{-3}			
TBABS*(VAPEC + VAPEC)	N_H	$2.7^{+2.8}_{-1.8} \times 10^{21}$ cm^{-2} *	$-31.82/-3$	112.59	-8.12 (59%)
	$kT_{\rm hot}$	> 8.36 keV			
	$kT_{\rm cool}$	$0.52^{+0.24}_{-0.11}$ keV			
	O, Ne, Mg, Si	11^{+24}_{-7}			
	E.M.$^{a}_{\rm hot}$	$3.3^{+1.83}_{-2.2} \times 10^{60}$ cm^{-3}			
	E.M.$^{a}_{\rm cool}$	$1.72^{+5.66}_{-0.96} \times 10^{60}$ cm^{-3}			
TBABS*VNEI	N_H	$5.9^{+1.8}_{-2.2} \times 10^{21}$ cm^{-2}	$-29.31/-2$	112.83	-8.15 (38%)
	kT	> 22 keV			
	O, Ne, Mg, Si	$1.7^{+1.2}_{-0.7}$			
	τ	$1.6^{+1.1}_{-0.7} \times 10^{10}$ s cm^{-3}			
	E.M[a]	$3.9^{+2.0}_{-1.4} \times 10^{60}$ cm^{-3}			

Table 3.1 Continued: Summary of spectral analysis results for Henize 2–10

Model	Parameters	Parameter Values	Δcstat$_{pl}$/Δd.o.f$_{pl}$	AICc	log(CvM) (goodness)
TBABS*(VAPEC + VAPEC + GAUSS)	N_H	$2.2^{+1.9}_{-1.3} \times 10^{21}$ cm^{-2} *	$-40.69/-5$	108.44	-8.29 (46%)
	$kT_{\rm hot}$	> 5 keV			
	$kT_{\rm cool}$	$0.59^{+0.20}_{-0.16}$ keV			
	O, Ne, Mg, Si	11^{+46}_{-7}			
	E.M.$^a_{\rm hot}$	$2.3^{+1.7}_{-1.3} \times 10^{60}$ cm^{-3}			
	E.M.$^a_{\rm cool}$	$1.6^{3.4}_{-0.7} \times 10^{60}$ cm^{-3}			
	E_0	4.56 ± 0.11 keV			
	σ	0.1 keV			
	Flux$_{\rm unabsorb,gauss}$	$6.6^{+6.6}_{-4.4} \times 10^{-16}$ ergs cm^{-2} s^{-1}			
`tbabs*(vnei + gauss)`	N_H	$4.9^{+2.1}_{-2.0} \times 10^{21}$ cm^{-2}	$-39.40/-4$	107.34	-8.50 (22%)
	kT	> 16 keV			
	O, Ne, Mg, Si	$2.3^{+2.0}_{-1.0}$			
	τ	$2.1^{+1.0}_{-0.9} \times 10^{10}$ s cm^{-3}			
	E.M.^{a}	$2.8^{+1.6}_{-1.1} \times 10^{60}$ cm^{-3}			
	E_0	4.56 ± 0.11 keV			
	σ	0.1 keV			
	Flux$_{\rm unabsorb,gauss}$	$6.6^{+7.0}_{-4.2} \times 10^{-16}$ ergs cm^{-2} s^{-1}			

Table 3.2: Summary of spectral analysis results for the candidate AGN in NGC 4178.

Model	Parameters	Parameter Values	Δcstat$_{pl}$/Δd.o.f$_{pl}$	AICc	log(CvM) (goodness)
PCFABS*PEGPWRLW (Expected)	N_H	5×10^{24} cm^{-2}	7.98/2	45.41	-3.60 (99%)
	f	0.99			
	Γ	2.3			
	Flux$_{\rm unabsorb}$	$8.4^{+2.6}_{-2.2} \times 10^{-13}$ ergs cm^{-2} s^{-1}			
TBABS*PEGPWRLW	N_H	$4.1^{+5.1}_{-3.3} \times 10^{21}$ cm^{-2}	0.0/0	42.18	-5.14 (99%)
	Γ	$2.9^{+1.4}_{-1.0}$			
	Flux$_{\rm unabsorb}$	$1.8^{+8.1}_{-1.0} \times 10^{-14}$ ergs cm^{-2} s^{-1}			
TBABS*(PEGPWRLW + GAUSSIAN + GAUSSIAN)	N_H	$3.4^{+10.7}_{-3.2} \times 10^{21}$ cm^{-2}*	$-15.02/-4$	39.14	-7.62 (30%)
	Γ	4^{+10}_{-2}			
	Flux$_{\rm pl,0.2-10.0}$	$1.8^{+68}_{-1.5} \times 10^{-14}$ ergs cm^{-2} s^{-1}			
	E_1	1.5 ± 0.1 keV			
	E_2	2.0 ± 0.1 keV			
	σ_1, σ_2	0.1 keV			
TBABS*VAPEC	N_H	$9.4^{+27.6}_{-7.2} \times 10^{20}$ cm^{-2} *	$-8.33/-1$	36.50	-6.49 (45%)
	kT	$1.4^{+1.1}_{-0.4}$ keV			
	O, Ne, Mg, Si	761^{+240}_{-750} **			
	E.M.[a]	$10^{58} - 10^{61}$ cm^{-3}			

Note: The model given by Secrest et al. (2012) (line 1) cannot explain the observed results. Comparing the Δcstat/Δd.o.f, AICc and the CvM statistic values, it is more probable that NGC 4178 is a SNR.

Chapter 4

Neutron Star in Supernova Remnant 1E 0102.2-7219

4.1 Introduction

The detection of the Crab (Staelin and Reifenstein 1968) and Vela pulsars (Large et al. 1968) within SNRs verified the theory that NSs are produced in supernova explosions (Baade and Zwicky 1934). However, not all likely core-collapse SNRs contain pulsars; some contain NSs in other manifestations, while some do not show any evidence of a compact object in them. Failures to detect NSs in deep X-ray surveys of nearby Galactic SNRs suggest that these SNRs produced BHs, exceptionally cold young NSs, or no compact object at all (Kaplan et al. 2004, 2006). Thus searching for and identifying NSs in young SNRs is essential for understanding supernovae in more detail.

X-ray studies have been one of the most effective means to find NSs in SNRs as NSs can generate bright X-ray emission through magnetospheric processes or simply by re-radiating the heat retained since their formation. X-ray observations by *Chandra* and *XMM-Newton* have helped reveal that NSs in young SNRs form a very diverse population. Approximately one-third of the young core-collapse SNRs have proposed evidence of associated NSs (Kaspi and

Helfand 2002). Considering selection effects, it is plausible that a majority of SNRs may contain radio pulsars. A significant number of young SNRs, however, contain central X-ray sources that do not show any signs of radio pulsar activity. These include anomalous X-ray pulsars (AXPs) and soft γ-ray repeaters (SGRs), which are manifestations of high-B ($B \sim 10^{14} - 10^{15}$ G) NSs known as magnetars (Thompson and Duncan 1995, 1996; Woods and Thompson 2006). At least nine magnetars are now confidently associated with SNRs (i.e. roughly 1/3 of the known magnetars Olausen and Kaspi 2014; Gavriil et al. 2008; Rea et al. 2016; D'Aì et al. 2016). The central X-ray sources in SNRs also include central compact objects (CCOs), showing purely thermal X-ray emission without radio or optical counterparts (Pavlov et al. 2004). Nine to eleven CCOs are known in SNRs (e.g. Gotthelf et al. 2013; Klochkov et al. 2016).

Rapidly rotating pulsars produce energetic charged particles, typically detectable in both radio and X-ray via synchrotron emission and/or as an extended pulsar wind nebula (Gaensler and Slane 2006; Kaspi et al. 2006; Li et al. 2008). The X-ray spectra of young radio pulsars ($\tau \lesssim 10^3$ yrs) generally include a primary non-thermal component along with a BB-like X-ray emission from the surface, often dominated by the hotter parts of the surface near the magnetic poles (e.g. Pavlov et al. 2001a; A. de Luca et al. 2005; Manzali et al. 2007). These spectra generally have temperatures between 40 and 200 eV, and the inferred radii between 1 and 10 km, when fit by BB models (e.g. Page et al. 2004). For old pulsars ($\tau \gtrsim 10^6$ yrs), the NS surface becomes cool, and the X-ray emission is primarily due to thermal radiation from the heated magnetic polar caps, with weak non-thermal components (e.g. PSR J0437-4715, Zavlin et al. 2002; Bogdanov et al. 2006). CCO X-ray spectra can be fit by an exclusively thermal spectra, with BB temperatures of a few hundred eV (Pavlov et al. 2002), while magnetars have more complex spectra that may be parameterized (below 10 keV) as hot ($0.3 - 0.5$ keV) BB plus a hard power-law (PL) contribution (e.g. Kaspi and Beloborodov 2017).

The thermal radiation of the NS is significantly affected by its mass, radii, magnetic field, surface temperature and the composition of the NS atmosphere (see Potekhin et al. 2014, for review). Thus, modelling the effects of these parameters on the NS X-ray spectra are essential to learn the properties of the NSs. Strong magnetic fields increase the binding energy of atoms and molecules (e.g. Lai 2001), affecting the thermal radiation from the NS atmosphere and producing to cyclotron resonance scattering that mimics a separate PL component (Lyutikov and Gavriil 2006). The assumption of a hydrogen atmosphere should be valid for most NSs where fallback or accretion has occurred since the elements stratify quickly to leave the lightest (generally H) on top (Alcock and Illarionov 1980; Romani 1987; Brown et al. 1998). Thermonuclear burning of the lightest elements on the hot young NS surface may remove H and He, possibly leaving a C (or higher-Z) atmosphere, if fallback and accretion are kept at very low rates (Chang et al. 2004; Chang et al. 2010; Wijngaarden et al. 2019). The heavy elements in such a mid-Z atmosphere can lead to detectable spectra features (Ho and Heinke 2009; Mori and Ho 2007) in soft X-rays. If such features can be confidently identified, the gravitational redshift of these spectral features would be a crucial constraint on the NS mass and radius, which would constrain our knowledge of the dense matter equation of state.

4.1.1 SNR 1E 0102.2-7219

The SNR 1E 0102.2-7219 (hereafter, E0102), discovered by the *Einstein* observatory (Seward and Mitchell 1981), is the second brightest X-ray source in the Small Magellanic Cloud (SMC). The high X-ray flux from E0102 and its strong emission lines of O, Ne and Mg make it an ideal calibration source in soft X-rays for instruments onboard *Chandra*, *Suzaku*, *Swift*, *XMM-Newton* (Plucinsky et al. 2017). Optical analyses of this SNR and the filaments in its ejecta, have revealed the SNR to be an oxygen-rich (Dopita et al. 1981; Tuohy and Dopita 1983) SNR with an age of 2000 ± 600 years (Finkelstein et al. 2006). Blair et al.

(2000) suggested it to have been produced by a Type Ib supernova, based on the non-detection of emission from O burning products (S, Ca, Ar). However, the recent detection of [S II], [S III], [Ar III] and crucially Hα by Seitenzahl et al. (2018) in the fast-moving ejecta of the SNR provides support for a Type IIb nature. Regardless, E0102 is certain to be formed by the core-collapse of a massive star, and thus is expected to have left a compact object.

Recently, Vogt et al. (2018) reported the detection of a compact object in E0102, from *Chandra* X-ray observations, supported by the MUSE identification of a low-ionization nebula surrounding the X-ray point source. However, they did not report a direct, detailed spectral analysis of the X-ray point source, in part due to the complexity of the X-ray background in this region. Density and temperature variations within the SNR can make it difficult to subtract the background directly, leading to large residuals in the background-subtracted spectrum. However, the analysis by Vogt et al. (2018), using only 4 spectral bins and only rough comparison between simple models and the X-ray data does not allow discrimination between different possible models for the X-ray emission from NSs.

In this paper, we re-analyzed the X-ray data used by Vogt et al. (2018), to verify the presence of an NS, and study the properties of this NS. In Section 4.2, we describe our data reduction methods and how we extracted the X-ray spectra. The details of the spectral analysis, the comparison between different models and the effects of background are discussed in Section 4.3. In Section 4.4, we discuss the implications of these results on the properties of the NS.

4.2 Observations and data reduction

The supernova remnant E0102 has been extensively observed by *Chandra*, and used as a calibration source to model the response of the CCD instruments (Plucinsky et al. 2017; Alan et al. 2019). However, the background X-ray

Table 4.1: X-ray observations used for analysis of E0102.

ObsID	Exp.(ks)	Year	ObsID	Exp.(ks)	Year
3519	8.01	2003	8365	20.98	2007
3520	7.63	2003	9694	19.20	2008
3544	7.86	2003	10654	7.31	2009
3545	7.86	2003	10655	6.81	2009
5130	19.41	2004	10656	7.76	2009
5131	8.01	2004	10657	7.64	2009
6042	18.9	2005	11957	18.45	2009
6043	7.85	2005	13093	19.05	2011
6075	7.85	2004	14258	19.05	2012
6758	8.06	2006	15467	19.08	2013
6759	17.91	2006	16589	9.57	2014
6765	7.64	2006	18418	14.33	2016
6766	19.70	2006	19850	14.33	2017

flux from E0102 around the compact object reported by Vogt et al. (2018) is extremely strong, necessitating the high angular resolution of the *Chandra X-ray Observatory*. We used *Chandra* ACIS-S VFAINT observations taken in timed exposure (TE) mode and pointed within $1.2'$ of SNR 1E 0102.2-7219 ($\alpha = 01^{\rm h}04^{\rm m}02.^{s}4; \delta = -72^{\circ}01'55.''3$). We excluded observations with signs of background flaring. We provide the list of all observations used for our analysis in Table 4.1. We point the readers to Plucinsky et al. (2017), Vogt et al. (2018), and Alan et al. (2019) for detailed comments on these observations.

We reprocessed all the data according to CALDB 4.7.6 standards using the command `chandra_repro` in CIAO 4.10 (Fruscione et al. 2006). We extracted events from a $1''$ region around the point source ($\alpha = 01^{\rm h}04^{\rm m}02.^{s}7; \delta = -72^{\circ}02'00.''2$) as a compromise between encompassing as large a fraction as possible of the point-spread function (PSF) of the *Chandra* ACIS-S instrument, and reducing the contribution from the background. This region captures about 90% of energy from a point source at ~ 1.5 keV. The source and the background regions used for the analysis are shown in Fig 4.1. These region files were shifted manually for individual observations to account for shifts in the astrometry.

We extracted the spectra from each observation separately using the CIAO

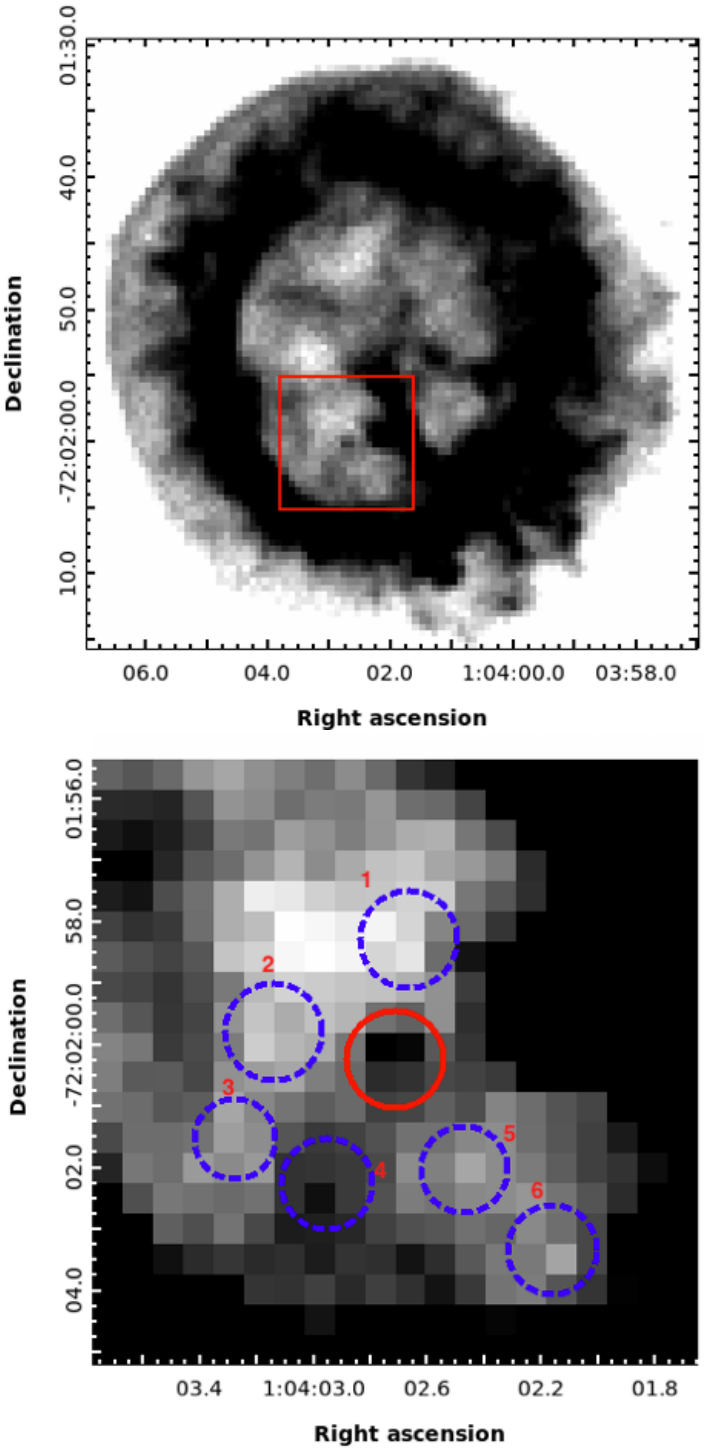

Figure 4.1: (*Top*) X-ray image of SNR 1E 0102.2-7219. (*Bottom*) Magnified image showing the position of the candidate NS within the SNR. The solid red circle (radius 1″) is our source extraction region. The dashed blue labelled circles denote background regions used in our study (see § 4.3.2). Emission from the SNR contributes significantly to the flux from the source region.

tool `specextract`, which considers the PSF and the encircled energy fractions while constructing the effective area files for the spectral analysis. The increasing contamination of the ACIS detectors has resulted in degradation of their low-energy quantum efficiency over the years (Marshall et al. 2004). Thus, individual observations have different effective areas and response matrix files. Assuming a linear response of the instruments, the spectra from these observations can be combined using `combine_spectra`. The `combine_spectra` tool of CIAO 4.10 also generates exposure weighted response matrix and ancillary response files (RMFs and ARFs respectively) for proper spectral analysis. The combined spectra have more counts and better statistics, allowing us to resolve narrow lines and test the quality ("goodness") of different models. We grouped the X-ray photons of the combined spectra so that each spectral bin has a width of at least 50 eV (~ 0.5 times the spectral resolution of *Chandra* ACIS) and contains at least 15 photons. As uncertainties in the bright background radiation from the supernova remnant itself dominate our uncertainties, we modelled the source spectrum along with the background, instead of subtracting the background and used Gaussian error bars for our analysis. We only considered the interval $0.5 - 10.0$ keV, where the *Chandra* ACIS-S instrument is most responsive. We used XSPEC v12.9.1m for spectral analysis. We adopted C-statistics (Cash 1979) for spectral fitting since it has been shown to be relatively unbiased, compared to χ^2 statistics, to fit Poissonian data (Humphrey et al. 2009).

We also verified our primary spectral results from the methods above by modelling all the spectra simultaneously, rather than combining them and modelling the combined spectrum. For this purpose, we combined the spectra from observations in a given year (within each year, the responses change only slightly) using `combine_spectra` and loaded each of these separately into XSPEC. We then modelled these spectra simultaneously by linking the corresponding parameters for each data set (We observe that the source doesn't exhibit any long-term variability). Grouping the spectra to 15 photons per bin

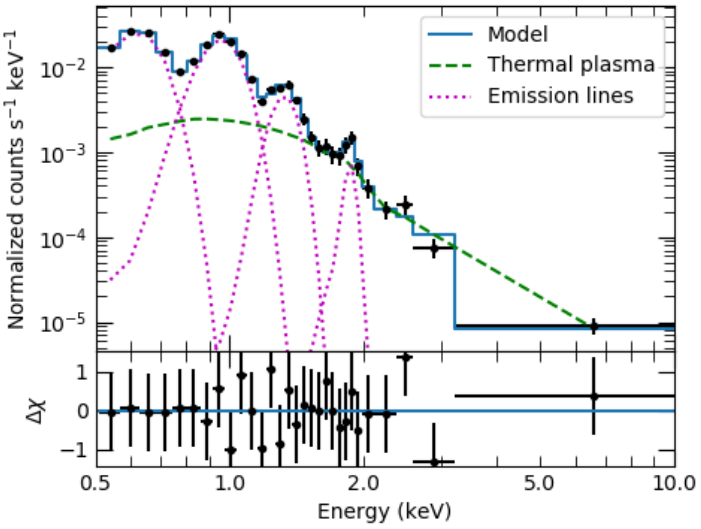

Figure 4.2: Empirical spectral fit to our background spectrum. Our model consists of a thermal plasma with $kT = 1.2 \pm 0.3$ keV and Gaussian emission lines at $E_1 = 0.60 \pm 0.01$ keV, $E_2 = 0.95 \pm 0.01$ keV, $E_3 = 1.32^{+0.02}_{-0.01}$ keV & $E_4 = 1.88 \pm 0.03$ keV, corresponding to the emission lines of O, Ne, Mg, and Si respectively. With χ^2/d.o.f = 10.64/16, the model is a good fit to the background spectrum.

leads to large bins and would miss narrow emission features. Therefore, we grouped the spectra such that each bin contains a minimum of 1 photon, and used C-statistics (Cash 1979) for our analysis.

In both cases, we compared the quality of different models using the AICc values (§ 1.4.3). Since AICc cannot comment on the absolute quality of the fit of a given model, we used the χ^2 test for the combined spectrum, and the "goodness" simulations of XSPEC, using the CvM statistic (Cramér 1928) for individual spectra analyzed simultaneously.

4.3 Results

Given the high background flux, we first needed to confirm the presence of a compact object in the SNR. Plucinsky et al. (2017) and Alan et al. (2019) do

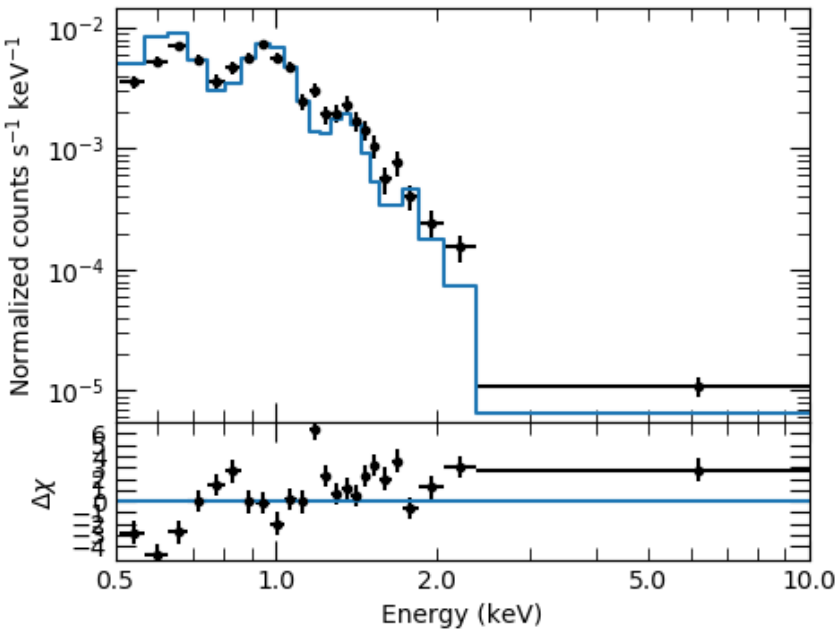

Figure 4.3: Source spectrum without background subtraction, fit with the scaled background model alone. The χ^2-test gives $\chi^2/\text{d.o.f} = 132.17/19$, resulting in a null hypothesis probability of $p \sim 10^{-16}$. The large residuals require an additional component along with the background.

not consider regions near the candidate compact object in their spectral analysis. We analyzed spectra derived from six different nearby background regions, and found that all six regions have similar spectra. Therefore we used these regions together to model the background flux. We fit the background using an empirical model consisting of a hot collisionally ionized plasma model (`apec`) with no lines (this was achieved in XSPEC using the command `xset APECNOLINES yes`) for the continuum and four Gaussian lines (`gaussian`) to model the emission line complexes from O, Ne, Mg, and Si. We used two components for absorption — `wabs` (which uses the Anders and Ebihara (1982) abundances) for absorption within the Milky Way, and `tbabs` with SMC abundances (Russell and Dopita 1992) for absorption by gas in the SMC (We use `wabs` since we need different abundances for absorption within milky way. Given that the absorption column is small, using `wabs` instead of `tbvarabs` with Wilms et al. (2000) values

Table 4.2: Background model used for the spectral analysis of the compact object in SNR 1E 0102.2-7219.

Parameters	**Parameter Values**
$N_{H,\mathrm{MW}}$	5.36×10^{20} cm^{-2}
$N_{H,\mathrm{SMC}}$	5.76×10^{20} cm^{-2}
kT	1.2 ± 0.3
$\mathrm{Flux_{apec}}$	$1.5^{+0.4}_{-0.3} \times 10^{-14}$ ergs cm^{-2} s^{-1}
E_O	0.60 ± 0.01 keV
σ_O	$0.065^{+0.008}_{-0.007}$ keV
Flux_O	$4.4^{+0.2}_{-0.3} \times 10^{-14}$ ergs cm^{-2} s^{-1}
E_{Ne}	0.95 ± 0.01 keV
σ_{Ne}	$0.084^{+0.008}_{-0.007}$ keV
$\mathrm{Flux_{Ne}}$	$2.1^{+0.1}_{-0.2} \times 10^{-14}$ ergs cm^{-2} s^{-1}
E_{Mg}	$1.32^{+0.02}_{-0.01} keV$
σ_{Mg}	0.07 ± 0.02
$\mathrm{Flux_{Mg}}$	$3.7^{+0.8}_{-0.7} \times 10^{-15}$ ergs cm^{-2} s^{-1}
E_{Si}	$1.88 \pm 0.03 keV$
σ_{Si}	< 0.07
$\mathrm{Flux_{Si}}$	$5^{+3}_{-2} \times 10^{-16}$ ergs cm^{-2} s^{-1}

doesn't lead to significant differences in the results). We fixed the absorption column of the Milky Way in this direction to 5.36×10^{20} cm^{-2}, and that of the SMC to 5.76×10^{20} cm^{-2} (Plucinsky et al. 2017) (allowing these to vary did not change the C-statistics or χ^2 significantly, as they are small). Thus our background model was `wabs * tbabs * (apec + gaussian + gaussian + gaussian + gaussian)`.

Fitting this model gave $kT = 1.2 \pm 0.3$ keV and Gaussian lines at $E_1 = 0.60 \pm 0.01$ keV (O complex, $\sigma = 0.065^{+0.008}_{-0.007}$ keV), $E_2 = 0.95 \pm 0.01$ keV (Ne complex, $\sigma = 0.084^{+0.008}_{-0.007}$ keV), $E_3 = 1.32 \pm 0.02$ keV (Mg complex, $\sigma = 0.07 \pm 0.02$ keV) and $E_4 = 1.88 \pm 0.03$ keV (Si line, $\sigma < 0.07$ keV) and a C-statistic value of 10.64 for 16 degrees of freedom (d.o.f). Using this simple empirical model, we found χ^2/d.o.f = 10.77/16. This corresponds to a null hypothesis probability

(that the data is drawn from the model) of $p = 0.82$, indicating that our background model is a good fit to the observed background spectrum as shown in Fig. 4.2. We also checked the fits to individual background regions using this model and found that all the parameters are similar within their error limits.

To check if the source emission can also be explained as only a spatial concentration of the same emission as the background, we fit this background model to the source spectrum (without background subtraction), permitting scaling of the background normalization. We also allowed for slight changes in the central energies of the emission lines, which could be due to different radial velocities. Fitting our background model alone to the source spectrum gave C-statistic/d.o.f. $= 132.17/19$ ($\chi^2 = 119.15$). This is a very poor fit ($p \sim 10^{-16}$) (shown in Fig. 4.3), indicating that additional components are required.

We also checked the validity of our method by applying this analysis technique for individual background regions. We extracted a spectrum from each background region and verified if each spectrum could be fit by a simple scaling of the combined background model discussed in Table 4.2. We found that the χ^2/d.o.f for background regions 1–6 were 15.24/13, 6.38/12, 22.67/10, 21.81/16, 9.87/13 and 22.41/11, respectively. These fits are much better than our fit of the source spectrum with the combined background model ($p \gtrsim 0.15$, except for regions 3 and 6 which have $p = 0.01, 0.02$, respectively.)

We next analyzed the spectrum by adding different models to our background model. We maintained the two-component absorption model, with fixed Galactic absorption (`wabs`, fixed to 5.36×10^{20} cm^{-2}), but allowed the SMC (`tbabs`) absorption to vary. The results of our analysis are summarized in Table 4.3. The simple power-law model gave $N_{H,SMC} = 9^{+8}_{-4} \times 10^{21}$ cm^{-2} and $\Gamma = 4.6^{+0.9}_{-0.5}$, with a C-statistic value of 22.66. Though this model is a better fit to the data with χ^2/d.o.f. $= 23.93/16$ ($p = 0.091$), such a large value of Γ has not been seen for non-thermal emission from pulsars or PWNe (Li et al. 2008), but is typical

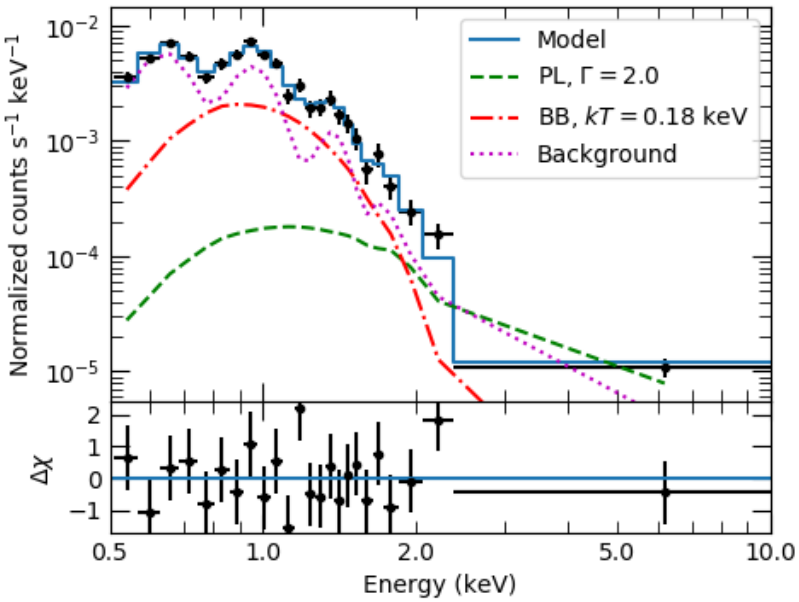

Figure 4.4: Blackbody + power-law fit to the observed spectrum. We model the source and background simultaneously. The best-fitting model gives $N_{H,SMC} = 5.6^{+10.7}_{-5.1} \times 10^{21}$ cm^{-2}, $T_{BB} = 2.1^{+0.4}_{-0.3} \times 10^6$ K, $R_{BB} = 8^{+7}_{-4}$ km. The power-law photon index is fixed to 2.0. The model gives χ^2/d.o.f = 17.33/15, and $p = 0.30$, indicating a good fit.

of the values found when power-law models are fit to spectra better described by a low-temperature BB or BB-like spectra, typical of NSs.

We, therefore, considered BB and BB-like models for the spectral fitting. We first fit with the `bbodyrad` model in XSPEC. This gave $N_{H,SMC} = 2^{+8}_{-2} \times 10^{21}$ cm^{-2}, $T_{BB} = (2.9 \pm 0.6) \times 10^6$ K, $R_{BB} = 3^{+4}_{-1}$ km and C-statistic value of 34.89. This model had χ^2/d.o.f. $= 32.41/16$ ($p = 0.0088$), a poor fit, and failed to explain the emission at higher energies.

Therefore, we added a PL with Γ fixed to 2 (typical of PWNe, Li et al. 2008) to include possible non-thermal emission from the magnetosphere and/or PWN that could account for the emission at higher energies. (We also tried allowing the power-law index to vary, but this led to the fitting parameters being poorly constrained, without improving the final fit.) As the black body fit is consistent with X-ray emission from an NS, we constrained the maximum

radius of the emitting region to 15 km. The best-fitting model, shown in Fig. 4.4, had $N_{H,SMC} = 5.6^{+10.7}_{-5.1} \times 10^{21}$ cm^{-2}, $T_{BB} = 2.1^{+0.4}_{-0.8} \times 10^{6}$ K, $R_{BB} = 8^{+7}_{-4}$ km, the flux from the power-law component, Flux$_{pl} = (3 \pm 1) \times 10^{-15}$ ergs cm^{-2} s^{-1} between 0.5 and 10 keV, and the C-statistic value = 18.11. This model gave χ^2/d.o.f = 17.33/15 i.e. $p = 0.30$, indicating an adequate fit. The unabsorbed $0.5 - 10$ keV thermal luminosity, $L_{BB} = 6^{+11}_{-2} \times 10^{33}$ ergs s^{-1}, was greater than the non-thermal luminosity, $L_{pl} = (1.4 \pm 0.4) \times 10^{33}$ ergs s^{-1}.

The harder X-ray component could also be fit with a hotter BB of $T_{BB,h} = 6^{+8}_{-1} \times 10^{6}$ K and $R_{BB,h} = 0.05 - 0.6$ km. This model could be interpreted as indicating the presence of hotspots at the magnetic poles of the NS. This model had similar C- & χ^2 statistics as the BB+PL model, but a higher AICc statistic due to one additional fitting parameter. The best-fit temperature was at the high end of the observed temperatures on NS (check § 4.4). Similar to the previous case, the softer component ($L_{x,c} = 1.3^{+0.8}_{-0.9} \times 10^{34}$ ergs s^{-1}) was more luminous than the harder component ($L_{x,h} = 1.0^{+0.6}_{-0.5} \times 10^{33}$ ergs s^{-1}).

To constrain the range of possible natures of this NS, we then tried fits with a variety of NS atmosphere models. We used the `nsmaxg` model in XSPEC which has spectral templates for different magnetic fields for hydrogen atmospheres, as well as for heavier elements (Mori and Ho 2007; Ho et al. 2008). We fixed the NS mass to 1.4 M$_\odot$ and radius to 12 km and vary the temperature and the normalization of the NS to fit the spectra. We fixed the upper limit of the normalization parameter to 1, indicating emission from the entire surface. We tried models with magnetic fields $B = 10^{10}$, 10^{12}, and 10^{13} G. These models failed to explain the emission at hard X-rays ($E > 2$ keV; $p \sim 0.01 - 0.02$ for all NS H atmosphere models). Therefore we added a power-law component with fixed photon index, 2, to the spectra to model possible magnetospheric or PWN emission. Adding a power-law reduced the C-statistic by ~ 4 while decreasing one degree of freedom (i.e. no significant change in AICc statistic, as seen in Table 4.3). With the power-law, the best-fitting models with different B had

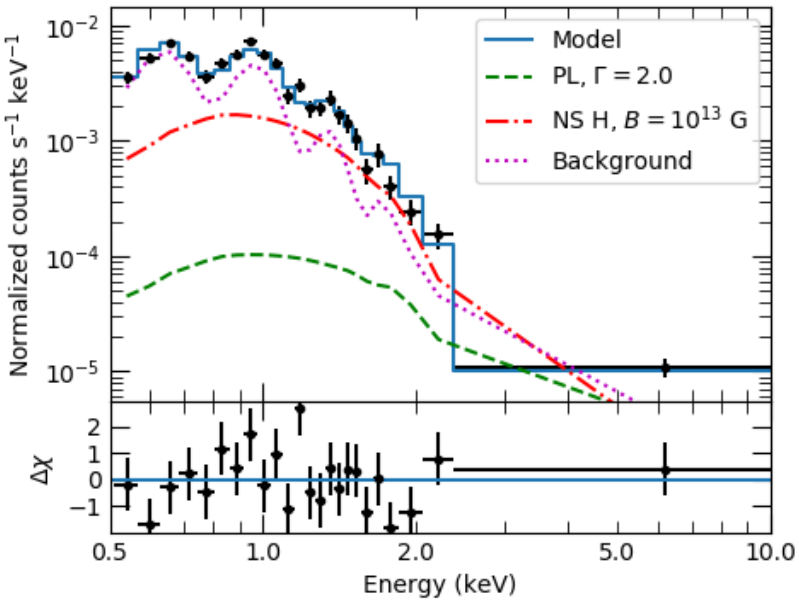

Figure 4.5: NS H atmosphere + power-law fit to the source spectrum and background. We use $M_{NS} = 1.4\mathrm{M}_{\odot}$, $R_{NS} = 12$km, $B = 10^{13}$ G, and photon index $\Gamma = 2.0$ for this spectral fit. The best-fit has $N_{H,SMC} = 2^{+3}_{-2} \times 10^{21}$ cm^{-2}, $T_{eff} = 1.74^{+0.19}_{-0.08} \times 10^{6}$ K, and $R_{em}/R_{NS} = 1.0^{+0.0}_{-0.3}$. With χ^2/d.o.f = 25.52/15, giving $p = 0.034$, this is a poor fit.

similar C-statistic values ($\sim 25 - 27$ for 15 d.o.f), $N_{\mathrm{H,SMC}}$ ($\sim 2 \times 10^{21}$ cm^{-2}), effective temperatures, ($T_{\mathrm{eff}} \sim 1.7 \times 10^{6}$ K) and radius of the emitting region ($R_{em}/R_{NS} \sim 1$). These models gave a thermal luminosity $L_{\mathrm{X,th}} \sim 4 \times 10^{33}$ ergs s^{-1} in the $0.5 - 10.0$ keV range. The large $\chi^2 \sim 26 - 27$ values for 15 d.o.f (i.e $p \sim 0.02 - 0.03$) indicated that NS H atmosphere models did not fit the data well, even after the addition of a non-thermal power-law component. We show the spectral fit with $B = 10^{13}$ G in Fig. 4.5, and residuals to the spectral fits for all three models in Fig. 4.6.

All the H atmosphere models left significant residuals around 1 keV. As the H atmosphere models have broader spectra than the BB models (which are more sharply curved), this might indicate a preference for a BB-like shape over the hydrogen atmosphere model shapes. However, considering the complex and bright background, we should consider whether these residuals are caused by

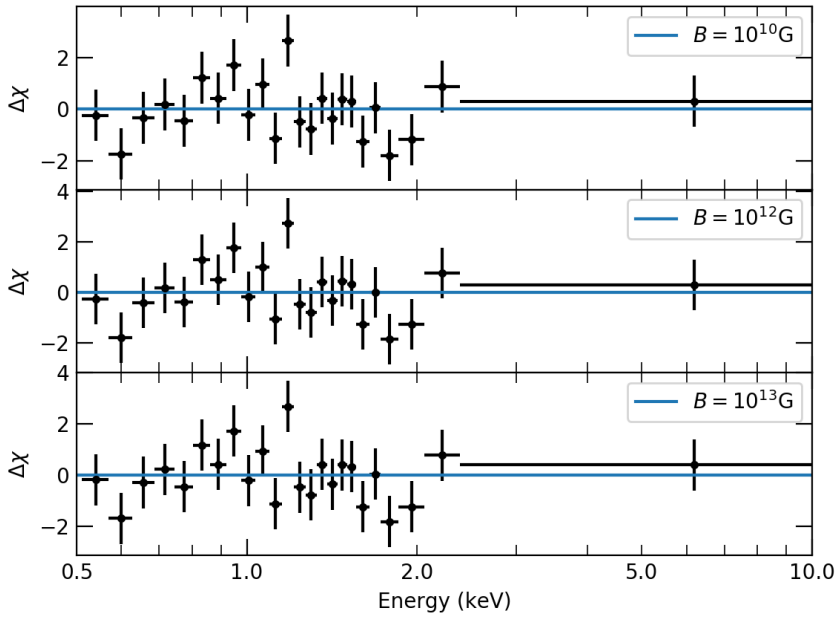

Figure 4.6: Residuals to fits with a thermal NS H atmosphere and non-thermal power-law, for three different surface magnetic fields ($B = 10^{10}, 10^{12}, 10^{13}$ G). The three models have similar residuals (at ∼1 and ∼1.8 keV), AICc values (~ 57), and χ^2 (~ 27 for 15 d.o.f, i.e. p-value $\sim 0.02 - 0.03$).

complexities in the background subtraction (see § 4.3.2).

If these spectral residuals at ~ 1 keV are indeed due to a sharper peak in the data than that of the absorbed NS H atmosphere model, they cannot be explained using multiple NS H atmospheres. Allowing for a lower temperature, $T_{\rm eff} \sim 8 \times 10^5$ K and larger absorption can replicate a narrower peak, but such a model would require an emitting region of $R_{em} > 25$ km, which is not feasible for a neutron star. Since heavier element atmosphere can have different spectral slopes (for example, a C atmosphere shows a sharper decline at $\sim$ 1–2 keV as compared to the H atmospheres; Mori and Ho 2007), we tried to fit the observed spectrum using the C, O, and Ne templates provided in `nsmaxg`.

We found that a carbon atmosphere with $B = 10^{12}$ G fit the X-ray spectrum best. This model could also explain the emission at the higher energies without an additional power-law component. Fig. 4.7 shows the best-fitting C atmosphere

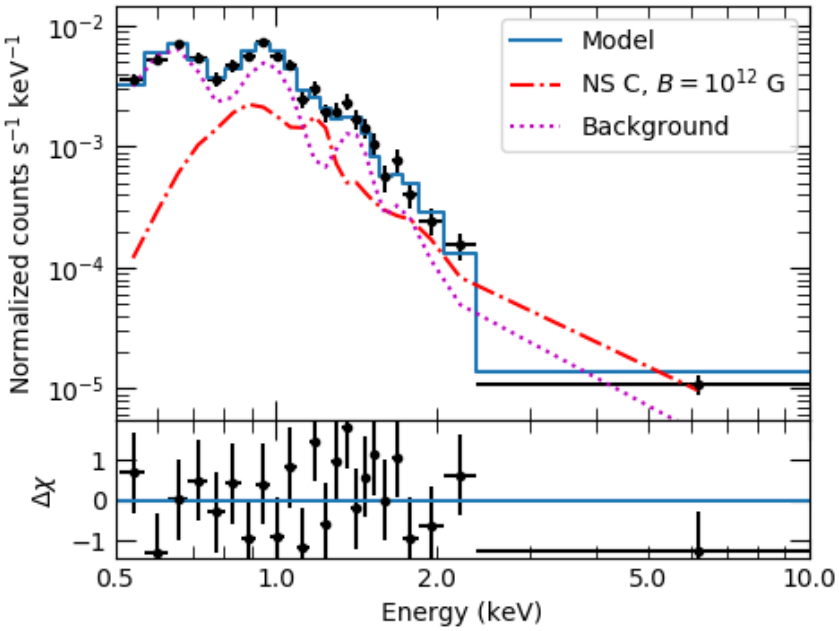

Figure 4.7: NS C atmosphere fit to the source spectrum on top of the background model. We use $M_{NS} = 1.4\mathrm{M}_{\odot}$, $R_{NS} = 12$km, and $B = 10^{12}$ G. The best-fitting model has $N_{H,SMC} = 9^{+12}_{-7} \times 10^{21}$ cm^{-2}, $T_{eff} = 3.0^{+0.5}_{-0.4} \times 10^{6}$ K, and $R_{em}/R_{NS} = 0.5^{+0.5}_{-0.2}$. With χ^2/d.o.f = 19.08/16, i.e. $p = 0.22$, this is a good fit.

model. This model gave $N_H = 9^{+12}_{-7} \times 10^{21}$ cm^{-2}, $T_{eff} = 3.0^{+0.5}_{-0.4} \times 10^{6}$ K and $R_{em}/R_{NS} = 0.5^{+0.5}_{-0.2}$ with a C-statistic value of 19.08. With χ^2/d.o.f = 18.85/16, i.e. $p = 0.28$ (which is comparable in quality to the `bbodyrad+pegpwrlw` fit), this model was an adequate fit. This model gave a thermal luminosity, $L_{X,th} = 8^{+10}_{-3} \times 10^{33}$ ergs s^{-1} between 0.5 and 10 keV. This fit was ~ 70 times better than the fit with the $B = 10^{13}$ G hydrogen atmosphere model, and ~ 8 times better than the fit to the `bbodyrad+pegpwrlw` model, based on AICc statistics. Using a non-magnetic carbon atmosphere model (e.g., `carbatm`; Suleimanov et al. 2014), or a $B = 10^{13}$ G carbon atmosphere gives a poorer fit. Using heavier elements like Ne or O gave no improvement over the hydrogen atmosphere models. Thus the spectral analysis favoured an NS with a 10^{12} G carbon atmosphere for the compact object in this SNR, though the complexities of background subtraction must be carefully considered (see § 4.3.2).

4.3.1 Simultaneous spectral analysis for individual years

We also checked if the changing response of the *Chandra* ACIS instrument over time affects the results of our spectral analyses significantly. As the ACIS instrument changes slowly over time, we summed the spectra within each calendar year to retain sufficient statistics. We loaded the spectra from individual years separately into XSPEC, and fit them simultaneously using the models discussed above. We summarize the results of our simultaneous spectral analysis in Table 4.4.

Both methods of spectral analysis (fitting the combined spectrum, and simultaneously fitting spectra loaded separately) resulted in similar parameter values for the different models used. The AICc statistics for the models used followed a similar trend, with the `(bbodyrad+pegpwrlw)`, and `NSMAXG` with $B = 10^{12}G$ C atmosphere, giving the best-fits (both these models have similar AICc values). We also noted that the change in the C-statistics by the addition of a PL or hotter BB to the single BB model was roughly equal in both cases (~ 17). The best-fitting C atmosphere model was ~ 6 times better than the 10^{13} G H atmosphere model with a power-law (and ~ 200 times better than the H atmosphere NS model alone).

Thus, a BB plus non-thermal power-law, or a neutron star with a carbon atmosphere, were the most favourable fits. However, this method of spectral analysis did not give much insight into the quality of the individual fits, as XSPEC's goodness simulations indicated that $< 5\%$ of the realizations have CvM statistics smaller than the best-fitting model in all cases. Another difference between the two methods of fitting was that adding a power-law to the H atmosphere models did not change the C-statistics and the AICc value appreciably (Δcstat ~ 5, ΔAICc < 1 corresponding to < 1.5 times better) while analyzing the combined spectrum, but when simultaneously modelling the individual spectra, Δ AICc ~ 8; i.e. adding a power-law improved the model by a factor of ~ 50.

4.3.2 Effects of altering background selection

Given the bright background, it is important to study how our choice of background spectrum affected our spectral modelling. To study the effect of changes in the background on the spectral parameters, we first modelled the spectra of each individual background region shown in Fig. 4.1. We used the background model described above (i.e., `wabs*tbabs*(apec + gaussian + gaussian + gaussian + gaussian)`) to model the individual background spectra. We found that grouping the background spectra such that each bin consisted of at least one photon per bin, and fitting them using C-statistics, gave the best constraints on the parameter values. We then used these various background models to analyze the combined source spectrum (modelling the background and source simultaneously). Using these different background models, we analyzed the change in the best-fitting parameters when the source is modelled using - `wabs*tbabs*bbodyrad`, `wabs*tbabs*(bbodyrad + pegpwrlw)`, `wabs*tbabs*(nsmaxg + pegpwrlw)` (H atmosphere, B=$10^{13}G$) and `wabs*tbabs*nsmaxg` (C atmosphere, B=$10^{12}G$). Our results are summarized in Table 4.5.

In general, we noticed that all the best-fitting parameters stayed within the same error limits even when the underlying background was modelled differently. However, we did notice that the C-statistics and χ^2 of the best-fitting models changed significantly. Inspecting the source spectra where `BB + PL` and `nsmaxg` with $B = 10^{12}$G C atmosphere models are not good fits, showed that varying the normalization and width of the background emission lines near the residuals significantly changes the fit quality. For example, when the background is modelled from region 1 alone, fixing σ_{Mg} to 0.07 (from Table 4.2) and allowing Flux_{Mg} to vary reduced the C-statistic by 12.72, while decreasing d.o.f by 1 (i.e ~ 50 times better according to AICc), giving χ^2/d.o.f = 19.02/15 (p-value = 0.21, i.e. a good fit). This signified that properly modelling the background was crucial to understand the quality of a spectral fit. However, we did notice

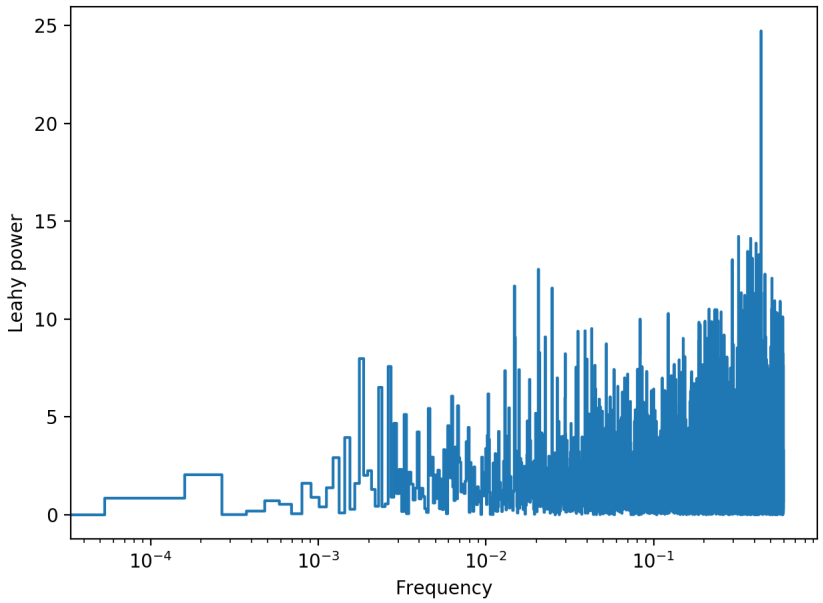

Figure 4.8: Leahy normalized power-spectrum of ObsID 6765 showing a peak at 0.44 Hz. The single trial probability of having a Leahy normalized power ≥ 24.7 is 4.27×10^{-6}. With 5573 frequency bins in this power spectra, this corresponds to a false alarm probability of 0.024.

that in all cases, a BB model with a power-law and a neutron star with a C atmosphere are still better fits than a simple BB or an NS with an H atmosphere. The NS H atmosphere plus power-law model has a reduced χ^2 (χ^2_ν) > 1.5 for all the different background models used, due to residuals at ~ 1 keV. Thus these residuals seem to be real, and not likely due to incorrect modelling of the background.

4.3.3 Search for X-ray pulsations

Pulsations in the X-ray light curve would reveal the presence of hotspots and their geometry. We checked for periodicity in individual observations where the time difference between successive frames (i.e. the time resolution), Δt is smaller than 1 s. For 13 observations, $\Delta t = 0.84$ s, allowing us to probe frequencies up to 0.6 Hz. We extracted barycentre-corrected light curves from each of these observations with the smallest allowed bin time (=Δt) using the CIAO 4.10

tools `axbary` and `dmextract`. We then constructed power spectra using the tool `apowerspectrum` of CIAO 4.10 and normalized them according to Leahy et al. (1983). Leahy-normalized power-spectra follow a χ^2 distribution with two degrees of freedom. We found a strong pulsation candidate at 0.44 Hz ($P = 2.28$ s) for ObsID 6765 (Fig. 4.8). This frequency had a Leahy-normalized power of 24.7. The single-trial probability of having Leahy-normalized power ≥ 24.7 is 4.27×10^{-6} ($\sim 4.6\sigma$). Given that this power spectrum had 5573 frequency bins, this corresponds to a false alarm probability of 0.024. However, we did not find any similarly strong signal in the remaining 12 power spectra (i.e all signals in the remaining 12 power spectra had false alarm probability > 0.35, indicating that these are likely due to Poisson noise). Considering searches over all these power spectra, the false-alarm probability rose to 0.31. We ran a Z_n^2 test on the ObsID 6765 using the phase calculated with a constant period $P = 2.28$s but did not find any rotational variability (significance of variability $< 2\sigma$). A single long-exposure observation would allow a deeper search for pulsations.

4.4 Discussion

4.4.1 Absorption

Most of our fits prefer a larger inferred absorption column (up to $\sim 10^{22}$ cm^{-2} in some cases) than observed for SNR 1E0102.2-7219 (5.76×10^{20} cm^{-2} of SMC absorption plus 5.36×10^{20} cm^{-2} of Galactic absorption Plucinsky et al. 2017; , consistent with the more recent analysis of Alan et al. 2019, which gives $N_{H,Gal} = 4.5 \times 10^{20}$ cm^{-2}, $N_{H,SMC} = 8 \times 10^{20}$ cm^{-2}). Recent calculations of the likely internal absorption column to the central NS produced by a $\sim$ 2000-year-old SNR are much smaller (Alp et al. 2018). However, we identify three caveats to this apparent discrepancy. First, the constraints on N_H are generally quite weak, such that the observed SNR N_H cannot be ruled out. Second, any contribution by SNR ejecta to the absorption will have much higher

abundances than the SMC in general. Third, the low-ionization gaseous ring (shell?) around the NS discovered by Vogt et al. (2018) may be thick enough to provide substantial extinction, though its nature and density have not yet been quantified. Such an optical feature/nebula is only found around one other CCO, CXOU J085201.4-461753 in SNR G266.2-1.2/Vela Jr. (Pavlov et al. 2001b; Pellizzoni et al. 2002; Mignani et al. 2019). However, whether this optical nebula is even associated with the CCO in Vela Jr. is not known.

4.4.2 Atmosphere

We found significant residuals when fitting the NS with any hydrogen atmosphere model. However, we found significantly better fits when using a (10^{12} G) C atmosphere, or a BB+PL. This suggests that either this NS hosts a C atmosphere, or that the atmosphere is described by some combination of composition, depth (e.g. an optically thin H atmosphere, which could have accumulated over 2000 years), and/or magnetic field, which we have not tried, and which might be reasonably represented by a BB. (Although we have tried a number of models, we cannot claim to have exhausted all the possibilities, especially if the surface is not homogeneous.)

A (non-magnetic) carbon atmosphere spectrum well-describes that of the youngest known NS, the CCO in the Cassiopeia A SNR (Ho and Heinke 2009). Similarly, a carbon atmosphere spectrum can also fit the spectrum of three other CCOs, two with ages of 1–2 kyr and one much older at 27 kyr (Klochkov et al. 2013, 2016; Doroshenko et al. 2018). As shown recently by Wijngaarden et al. (2019), a carbon atmosphere can be present on an NS of sufficient youth ($\lesssim$ 1000 yr), as its high temperature burns any surface hydrogen or helium. After this age, the temperature becomes low enough to allow accumulation of hydrogen even at very low accretion rates and thus the formation of a hydrogen atmosphere. With an age of 2000$\pm$600 yr, E0102 exists at the transition between a carbon atmosphere or a thin hydrogen atmosphere, with the latter being just

physically thick enough to have an optical thickness $\tau_\nu \sim 1$, such as that which seems to exist on (much older) X-ray isolated NSs such as RX J0720.4−3125 (Motch et al. 2003) and RX J1856.5−3754 (Ho et al. 2007).

In contrast to the above CCOs that are fit with a carbon atmosphere spectrum which assumes no or low magnetic fields, our best-fit carbon spectrum assumes $B = 10^{12}$ G. Spin and spectral properties of three other CCOs (Mereghetti et al. 2002; Sanwal et al. 2002; Halpern and Gotthelf 2010a; Gotthelf et al. 2013) indicate these three CCOs have $B \sim 10^{10} - 10^{11}$ G. A low magnetic field currently could be due to a stronger field that was buried by initial fallback of supernova material and is only now emerging at the surface (Ho 2011; Ho et al. 2015). The emergence timescale depends on the amount of material accreted, such that E0102 could have accreted less and thus its field has already emerged to values typical of pulsars. Alternatively, E0102 could be a magnetar with a subsurface field that is $\gtrsim 10^{14}$ G and a surface field that is still emerging. If E0102 is a magnetar, it may undergo a magnetar outburst in the future. This is an interesting prospect given the extensive monitoring of SNR 1E 0102.2−7219 as a calibration source for telescopes such as *Chandra* and *NICER*.

4.4.3 Nature of the neutron star

We also look into the general properties of CCOs, magnetars and young pulsars to further study the nature of E0102 and classify the NS

de Luca (2008, 2017) and Halpern and Gotthelf (2010a) summarize all known CCOs. We see that most CCOs have thermal luminosities $\sim 10^{33}$ ergs s^{-1}). XMMU J173203.3-344518 in SNR G353.6-0.7 has a thermal luminosity, 1.3×10^{34} ergs s^{-1}, comparable with that of E0102, though it requires relatively extreme cooling parameters (Klochkov et al. 2015). Its X-ray spectrum can be best-fit using a two temperature BB ($kT_1 \approx 0.4$ keV, $R_1 \approx 1.5$ km, $kT_2 \approx 0.6 - 0.9$ keV, $R_2 \approx 0.2 - 0.4$ km; Halpern and Gotthelf 2010b) or a non-magnetic NS

with a C atmosphere ($kT \approx 0.19$ keV, $R \approx 13$ km; Klochkov et al. 2013). The observed lack of pulsations supports the C atmosphere model where the entire NS surface emits radiation. Such a non-magnetized C atmosphere, with $kT \sim 0.15$ keV and emission from the entire NS, has also been proposed for the CCOs CXOU J232327.9+584842 (in the SNR Cas A, Ho and Heinke 2009), CXOU J160103.1-513353 (in G330.2+1.0, Doroshenko et al. 2018) and CXOU J181852.0-150213 (in G15.9+0.2, Klochkov et al. 2016). X-ray emission of other CCOs can be adequately fit ($\chi^2_\nu \leq 1.1$) using a BB ($kT \sim 0.5$ keV) or a non-magnetic NS atmosphere model ($kT \sim 0.3$ keV) (Gotthelf et al. 2013; Halpern and Gotthelf 2010a; Lovchinsky et al. 2011). However, a second BB ($kT_1 = 0.2 - 0.4$ keV, $R_1 = 2 - 4$ km, $kT_2 = 0.5 - 0.9$ keV, $R_2 \lesssim 1$ km) or NS atmosphere component often improves the fit.

Timing solutions of CCOs showing rotational variability (PSR J0821-4300, PSR 1852+0040 and 1E 1207.4-5209) reveal periods between 0.1 and 0.4s, as well as surface $B < 10^{11}$ G, indicating that CCOs have relatively low B fields (Gotthelf et al. 2013; Halpern and Gotthelf 2010a). The E0102 NS cannot be fit using a single BB or NS atmosphere model ($\chi^2_\nu \sim 2$), and the C atmosphere fit needs a higher magnetic field ($B = 10^{12}$) and relatively high temperature ($kT \sim 0.3$ keV) for a good fit. Although other CCOs show no indications of radio pulsations or synchrotron nebulae, it is not clear whether their observed spin-downs correctly indicate their surface B fields. For example, the high pulsed fraction of the NS in Kes 79 strongly indicates a high surface B field, possibly in a strongly multipolar configuration (Bogdanov 2014). It has been suggested that the low measured fields in CCOs are due to burial of the field by fallback (e.g. Ho 2011), in which case a normal B field for E0102 would not be truly unusual (though it would raise questions about why it has not shown radio pulsar behavior).

The thermal emission of magnetars with $B \sim 10^{14}$–10^{15} G in their quiescent state is very similar to that of CCOs, and generally cannot be distinguished by

X-ray spectra alone. We use the McGill online magnetar catalog (Olausen and Kaspi 2014) to study and compare the X-ray properties of magnetars. Magnetars of age $\mathcal{O}(10^3$ yrs) have thermal X-ray luminosities, $L_{2-10\ \mathrm{keV}} \sim 10^{33} - 10^{35}$ ergs s^{-1} during their quiescent state, encompassing the E01012 NS's luminosity (see Fig. 4.9). Like CCOs, the X-ray spectra of magnetars can also be fit using two BB components, or a BB+PL. The observable differences between magnetars and CCOs come from X-ray variability — magnetars typically show fast, bright outbursts, and/or show pulsations (with periods $\sim 2 - 12$ s) revealing rapid spin-down indicative of high B fields. Our tentative 2.28 s periodic signal is near the lower limit of the rotation period for known magnetars. We did not identify any long-term X-ray variability from E0102 over the years 2003–2017. From Viganò et al. (2013), we see that the expected outburst rate for magnetars of age 2000 years is ~ 0.05/yr. Thus the non-detection of an X-ray outburst does not rule out the possibility that E0102 could be a magnetar in quiescence.

A thermal component has been detected in very few young (ages below 10^4 years) pulsars with "normal" B-field strengths, $B < 10^{12}$ G, due in part to the bright non-thermal pulsed and pulsar wind X-ray emission. Only four radio pulsars have measured thermal X-ray spectral components (each also has non-thermal components) and inferred ages $< 10^4$ years; these are PSR J1119-6127 (Gonzalez et al. 2005, τ=1600 years), PSR J1357-6429 (Zavlin 2007, τ=7300 years), PSR J1734-3333 (Olausen et al. 2013, τ=8100 years), and PSR B1509-58 (Hu et al. 2017, τ=1700 years). Interestingly, these four young pulsars all show high magnetic fields; estimating B from P and $\dot{P}$, $B = 4 \times 10^{13}$ G, 8×10^{12} G, 5×10^{13} G, and 1.5×10^{13} G respectively. Blackbody fits to their thermal components give $T = 2.4^{+0.3}_{-0.2} \times 10^6$ K, $R = 3.4^{+1.8}_{-0.3}$ km, $L_{X,bb} = 2^{+2.5}_{-0.4} \times 10^{33}$ ergs s^{-1} for J1119, $T = (1.7 \pm 0.2) \times 10^6$ K, $R = 2.5 \pm 0.5$ km, $L_{X,bb} \sim 2 \times 10^{32}$ ergs s^{-1} for J1357, $T = (3.5 \pm 0.7) \times 10^6$ K, $R = 0.45^{+0.55}_{-0.20}$ km, $L_{X,bb} \sim 2 \times 10^{32}$ ergs s^{-1} for J1734, and $T = (1.7 \pm 0.1) \times 10^6$ K, $R \sim 9$ km, $L_{X,bb} \sim 9 \times 10^{33}$ ergs s^{-1} for B1509.

Unusually, the thermal components show extremely strong pulsations in two of these (48–74% pulsed fraction for J1119 Gonzalez et al. 2005; Ng et al. 2012, >50% pulsed fraction for J1357; J1734 has only an upper limit on the pulsed fraction of <60%, and pulsation searches on B1509's thermal component were not possible due to the strong pulsed nonthermal emission). Such strong pulsations cannot be achieved for any hotspot geometry without substantial radiative beaming, which requires higher B fields $> 10^{14}$ G (Bogdanov 2014). Indeed, J1119 (estimated $B = 8 \times 10^{12}$ G) underwent a series of transient magnetar bursts (Archibald et al. 2016), strongly indicating that J1119, and possibly the others, have magnetar-strength internal B fields (e.g. Ho 2011; Viganò and Pons 2012; Bernal et al. 2013). The E0102 NS has a higher thermal luminosity than these high-B young pulsars, and an apparently larger emitting radius. It appears that if E0102 NS is a radio pulsar, it is likely to resemble these high-B pulsars, and may be a hidden magnetar.

In Figure 4.9, we show the luminosity and age of E0102, as well as those of CCOs (see Reynolds et al. 2006; Klochkov et al. 2016; and references in Luo et al. 2015), magnetars and rotation-powered pulsars (Chang et al. 2012; Olausen et al. 2013; Viganò et al. 2013; Hu et al. 2017). The shaded region indicates luminosity as a function of age for theoretical models of NS cooling, assuming a $1.4M_{\odot}$ NS built using the APR equation of state and a light element envelope: the upper boundary considers slower cooling due to superconducting protons while the lower boundary considers more rapid cooling due to Cooper pair formation and breaking of superfluid neutrons; meanwhile the solid line is for the same model as the upper boundary but with an iron envelope and $1.2M_{\odot}$ NS (see Luo et al. 2015, and the references therein, for details).

Regardless of the atmosphere model we use, we find a very high thermal luminosity for the E0102 NS, which we can explain either through a slow loss of heat from the supernova explosion, or decay of an initially strong magnetic field. Our carbon atmosphere NS spectral model gives a bolometric thermal

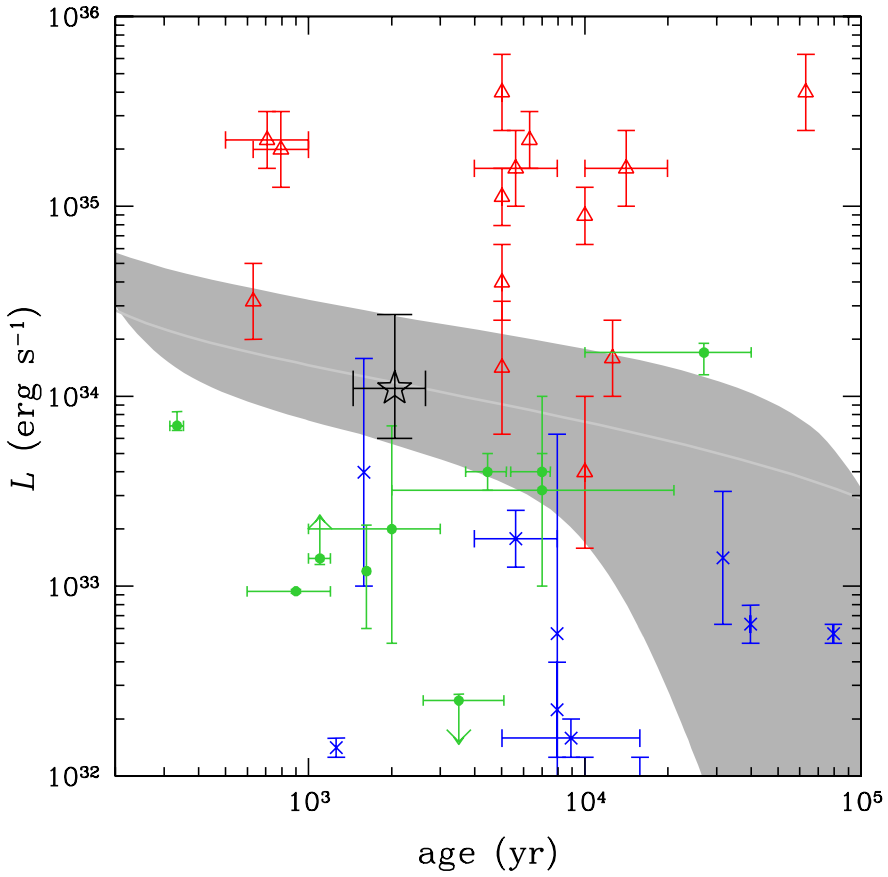

Figure 4.9: Thermal luminosity vs. age of E0102 (black) w.r.t known pulsars (blue), CCOs (green) and magnetars (red). The shaded region shows the cooling scenario for $M = 1.4\mathrm{M}_{\odot}$, $R = 11.6$ km and a light elements envelope. The upper bound of this region is obtained by only considering superconducting protons and the lower bound is is achieved by the superfluidity of neutrons as well. Cooling curves for heavy element envelopes do not explain the luminosity of E0102 well. E0102 is brighter than CCOs and pulsars but less luminous than magnetars of similar age.

luminosity $L_{bol} = 1.1^{+1.6}_{-0.5} \times 10^{34}$ ergs s^{-1}. Comparing E0102's parameters to other known young NSs, we are struck by E0102's relatively high inferred temperature and thermal luminosity. Hu et al. (2017), Halpern and Gotthelf (2010a), and Viganò et al. (2013) give useful context for the thermal luminosities of young pulsars, CCOs, and magnetars with respect to their age. E0102's thermal luminosity is larger than most rotation-powered pulsars. Only young CCOs like PSR J1852+0040 (SNR G33.6+0.1), PSR J0821-4300 (SNR Puppis A) and

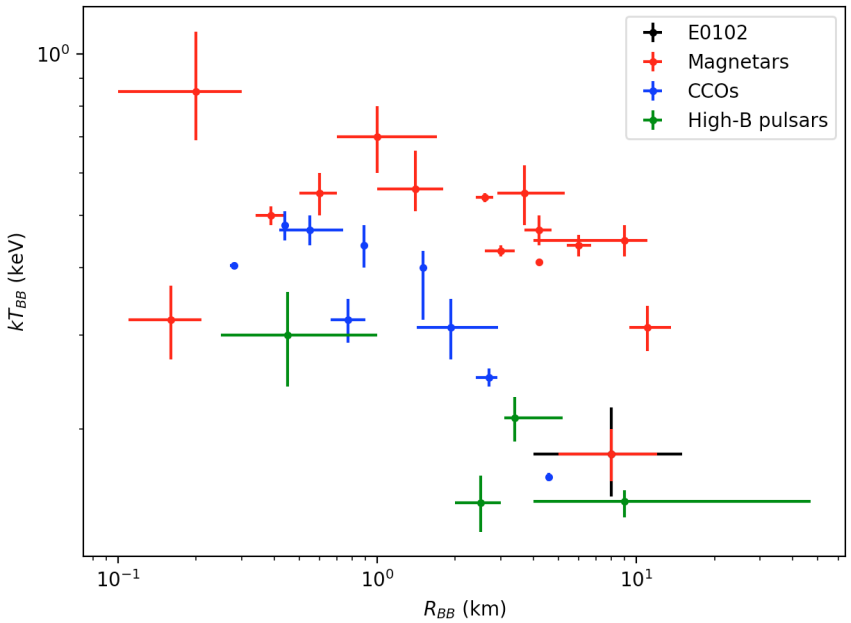

Figure 4.10: Comparison of kT and R_{BB} on fitting a BB model to different classes of NS. Magnetars are usually hotter and brighter than CCOs and high-B pulsars. The leftmost magnetar ($R_{BB} \sim 0.2$, $kT \sim 0.3$ keV is a low magnetic field ($B = 6 \times 10^{12}$ G) faint ($L_{bol} \sim 4 \times 10^{31}$ ergs s^{-1}) system, SGR 0418+5729 (Rea et al. 2013). The position of E0102 is consistent with that of some CCOs, high-B pulsars, and magnetars.

PSR J1210-5226 (SNR G296.5+10.0), the young high-B pulsars B1509-58 and J1119-6127, and magnetars have thermal emission within the error limits of E0102's luminosity. Comparing the E0102 NS with the cooling curves in Luo et al. (2015) (Fig. 4.9) for different envelope composition and conductivity of protons and neutrons, and those of Viganò et al. (2013) for different magnetic field and envelope composition, the large thermal luminosity may be explained by decay of a strong magnetic field (as in the magnetars), or by the slow cooling of an NS envelope composed of lighter elements.

We compare the emitting radius and temperature of the observed BB radiation from CCOs, high-B pulsars, and magnetars in Fig. 4.10. Unfortunately, this does not clearly distinguish between the three groups of NSs. Although E0102's properties are somewhat unusual for each class, there are members of each class with similar properties.

4.5 Summary and conclusions

In this work, we have used the combined spectra from the *Chandra* ACIS-S observations of SNR 1E 0102-7219 to argue that the compact object detected by (Vogt et al. 2018) in the SNR is a neutron star, and to constrain its nature and properties. The observed X-ray spectrum of this source cannot be explained as a concentration of SNR emission, clearly requiring an additional soft BB-like source, confirming the detection by Vogt et al. (2018) of a neutron star in this SNR. The emission at higher energies cannot be modelled by a simple BB, requiring an additional non-thermal power-law component. Among the NS models, we see that H atmosphere models at any B-field strength fail to fully model the X-ray spectra. Adding a power-law component successfully models the emission at higher energies, but the residuals around ~ 1 keV are still not explained. A 10^{12} G carbon atmosphere NS model better fits these residuals, as well as emission at the higher energies.

The best-fit temperature and luminosity of this compact object in E0102 are higher than most NSs observed. Comparing the thermal luminosity to other pulsars indicates that it is unlikely that this compact object is powered by rotation. The high temperature and the presence of hotspots suggest that this source is powered by its high magnetic fields, like the magnetars and some high-B radio pulsars. However, there are a few observed low-B NSs with inferred ages $< 10^4$ years and similar temperatures, so the emission we see may be heat from the supernova explosion that formed this NS. Identifying and studying young neutron stars like this one is essential to understand the physical mechanisms responsible for the high thermal luminosity.

The greatest challenge in studying this NS is the bright background emission from the SNR itself. Though the parameter values do not change significantly when using different background models, the C-statistic and the χ^2 value indicate the quality of the fits change significantly. The proposed Lynx X-ray mission

(The Lynx Team 2018), with higher effective area, greatly improved spectral resolution, and similar angular resolution as *Chandra* would permit a more powerful analysis of such compact objects in bright SNRs. Lynx's high spectral resolution would allow us to identify and filter out the background emission lines from the source spectra. It is also possible that Lynx could measure spectral features (e.g. edges) in NS spectra, identifying the nature of the NS atmosphere. Lynx's higher effective area could also detect X-ray pulsations (if present), permitting the measurement of P and $\dot{P}$, and thus constraining the magnetic field strength. The higher effective area would also allow the expansion of the study of NS surfaces to nearby galaxies would add greatly to our understanding of NSs.

Table 4.3: Summary of modelling the combined spectrum of the compact object in SNR 1E 0102.2-7219

Model	Parameters	Parameter Values	cstat	AICc	χ^2/d.o.f (p-value)
WABS*TBABS*BBODYRAD	f	$0.21^{+0.03}_{-0.04}$	34.89	60.49	32.41/16 (0.0088)
	$N_{H,SMC}$	$2^{+8*}_{-2} \times 10^{21}$ cm^{-2}			
	T_{BB}	$(2.9 \pm 0.6) \times 10^6$ K			
	R_{BB}	3^{+4}_{-1} km			
WABS*TBABS*(BBODYRAD + PEGPWRLW)	f	0.19 ± 0.04	18.11	48.97	17.33/15 (0.30)
	$N_{H,SMC}$	$5.6^{+10.7}_{-5.1} \times 10^{21}$ cm^{-2}			
	T_{BB}	$2.1^{+0.4}_{-0.3} \times 10^6$ K			
	R_{BB}	8^{+7**}_{-4} km			
	Γ	2.0			
	Flux$_{pl}$	$(3 \pm 1) \times 10^{-15}$ ergs cm^{-2} s^{-1}			

Note: All the above models were added to the previously specified background model and fit to the observed X-ray spectra without background subtraction. "f" represents the normalization constant multiplied to the background model before being added to the above models, "$N_{H,SMC}$" represents the absorption within the SMC, "T_{BB}, T_{eff}", "R_{BB}, R_{em} are the effective temperature and emitting radius of the BB, NS respectively, and "Flux$_{pl}$" represents the unabsorbed flux from the power-law component between 0.2 and 10.0 keV. We fixed the absorption column due to Milky way in the direction of SMC to 5.36×10^{20} cm^{-2} (Plucinsky et al. 2017). For the NS atmosphere models, we fixed the radius of the NS $R_{NS} = 12$ km. We see that the source is best modelled by an NS with a C atmosphere, or a simple BB with a harder PL or a hotter BB component.

* Lower error bound reaches the lower hard limit.

** Upper error bound exceeds the upper hard limit.

Table 4.3 Continued: Summary of modelling the combined spectrum of the compact object in SNR 1E 0102.2-7219.

Model	Parameters	Parameter Values	cstat	AICc	χ^2/d.o.f (p-value)
WABS*TBABS*(BBODYRAD + BBODYRAD)	f	0.20 ± 0.03	16.72	53.64	16.30/14 (0.30)
	$N_{H,SMC}$	$1.0^{+0.6}_{-0.9} \times 10^{22}$ cm^{-2}			
	$T_{BB,c}$	$1.8^{+0.6}_{-0.1} \times 10^{6}$ K			
	$R_{BB,c}$	$15^{+0.0**}_{-10}$ km			
	$T_{BB,h}$	$6^{+8}_{-1} \times 10^{6}$ K			
	$R_{BB,h}$	$0.29^{+0.30}_{-0.24}$ km			
WABS*TBABS*(NSMAXG) (H atmosphere, $B = 10^{10}G$)	f	0.20 ± 0.03	30.46	56.06	30.43/16 (0.016)
	$N_{H,SMC}$	$2^{+4*}_{-2} \times 10^{21}$ cm^{-2}			
	T_{eff}	$1.7^{0.4}_{-0.1} \times 10^{6}$ K			
	(R_{em}/R_{NS})	$1.0^{+0.0**}_{-0.5}$			
WABS*TBABS*(NSMAXG + PEGPWRLW) (H atmosphere, $B = 10^{10}G$)	f	0.20 ± 0.03	25.40	56.25	26.25/15 (0.036)
	$N_{H,SMC}$	$1^{+4*}_{-1} \times 10^{21}$ cm^{-2}			
	T_{eff}	$1.6^{+0.2}_{-0.1} \times 10^{6}$ K			
	(R_{em}/R_{NS})	$1.0^{+0.0**}_{-0.3}$			
	Γ	2.0			
	Flux$_{pl}$	$(1.6^{+1.4}_{-1.2}) \times 10^{-15}$ ergs cm^{-2} s^{-1}			
WABS*TBABS*(NSMAXG) (H atmosphere, $B = 10^{12}G$)	f	0.20 ± 0.03	31.64	57.24	31.67/16 (0.011)
	$N_{H,SMC}$	$2^{+4*}_{-2} \times 10^{21}$ cm^{-2}			
	T_{eff}	$1.74^{+0.42}_{-0.06} \times 10^{6}$ K			
	(R_{em}/R_{NS})	$1.0^{+0.0**}_{-0.5}$			

Table 4.3 Continued: Summary of modelling the combined spectrum of the compact object in SNR 1E 0102.2-7219.

Model	Parameters	Parameter Values	cstat	AICc	χ^2/d.o.f (p-value)
WABS*TBABS*(NSMAXG + PEGPWRLW) (H atmosphere, $B = 10^{12}G$)	f	$0.20^{0.03}_{-0.04}$	26.86	57.72	27.87/15 (0.022)
	$N_{H,SMC}$	$1^{+4*}_{-1} \times 10^{21}$ cm^{-2}			
	T_{eff}	$1.7^{+0.2}_{-0.1} \times 10^6$ K			
	(R_{em}/R_{NS})	$1.0^{+0.0**}_{-0.3}$			
	Γ	2.0			
	Flux$_{pl}$	$(1.6 \pm 1.3) \times 10^{-15}$ ergs cm^{-2} s^{-1}			
WABS*TBABS*(NSMAXG) (H atmosphere, $B = 10^{13}G$)	f	$0.20^{+0.03}_{-0.04}$	28.99	54.49	29.47/16 (0.021)
	$N_{H,SMC}$	$2^{+4*}_{-2} \times 10^{21}$ cm^{-2}			
	T_{eff}	$1.8^{+0.3}_{-0.1} \times 10^6$ K			
	$(R_{em}/R_{NS})^2$	$1.0^{+0.0**}_{-0.4}$			
WABS*TBABS*(NSMAXG + PEGPWRLW) (H atmosphere, $B = 10^{13}G$)	f	0.19 ± 0.03	25.52	56.37	26.37/15 (0.034)
	$N_{H,SMC}$	$2^{+3*}_{-2} \times 10^{21}$ cm^{-2}			
	T_{eff}	$1.74^{+0.19}_{-0.08} \times 10^6$ K			
	(R_{em}/R_{NS})	$1.0^{+0.0**}_{-0.3}$			
	Γ	2.0			
	Flux$_{pl}$	$(1.4^{+1.4}_{-1.3}) \times 10^{-15}$ ergs cm^{-2} s^{-1}			
WABS*TBABS*(NSMAXG) (C atmosphere, $B = 10^{12}G$)	f	$0.21^{+0.03}_{-0.04}$	19.08	44.69	18.85/16 (0.28)
	$N_{H,SMC}$	$9^{+12}_{-7} \times 10^{21}$ cm^{-2}			
	T_{eff}	$3.0^{+0.5}_{-0.4} \times 10^6$ K			
	(R_{em}/R_{NS})	$0.5^{+0.5}_{-0.2}$			

Table 4.4: Spectral analysis by simultaneously modelling the the individual spectra of NS in SN 1E 0102.2-7219.

Model	Parameters	Parameter Values	cstat (d.o.f)	AICc	log (CvM) (goodness)
WABS*TBABS*BBODYRAD	f	$0.20^{+0.04}_{-0.02}$	577.56 (675)	593.77	−10.80 (3%)
	$N_{H,SMC}$	$< 3^{*} \times 10^{22}$ cm^{-2}			
	T_{BB}	$3.1^{+0.6}_{-0.4} \times 10^{6}$ K			
	R_{BB}	3 ± 1 km			
WABS*TBABS*(BBODYRAD + PEGPWRLW)	f	$0.16^{+0.05}_{-0.04}$	557.27 (674)	575.54	−10.85 (2%)
	$N_{H,SMC}$	$3^{+11*}_{-3} \times 10^{21}$ cm^{-2}			
	T_{BB}	$2.1^{+0.5}_{-0.4} \times 10^{6}$ K			
	R_{BB}	7^{+8**}_{-3} km			
	Γ	2.0			
	Flux$_{pl}$	$(5 \pm 2) \times 10^{-15}$ ergs cm^{-2} s^{-1}			

Note: Variables and notations used have the same meaning as in Table 4.3. The last column indicates the value of the Cramer von-Mises statistic (Cramér 1928; von Mises 1931) and the goodness value corresponding to it. The goodness value indicates the fraction of the realizations of the model which have a CvM statistic smaller than that of the data. A large value (say 95%) indicates that the observed spectrum can be rejected (with 95% confidence). We note that the best-fitting values of the parameters are similar to their corresponding values in Table 4.3.

Table 4.4 Continued: Spectral analysis by simultaneously modelling the individual spectra of NS in SN 1E 0102.2-7219.

Model	Parameters	Parameter Values	cstat (d.o.f)	AICc	log (CvM) (goodness)
WABS*TBABS*(BBODYRAD + BBODYRAD)	f	$0.16^{+0.05}_{-0.04}$	560.97 (673)	581.29	−10.83 (2%)
	$N_{H,SMC}$	$2^{+10*}_{-2} \times 10^{21}$ cm^{-2}			
	$T_{BB,c}$	$2.2^{+0.6}_{-0.5} \times 10^{6}$ K			
	$R_{BB,c}$	6^{+5}_{-1} km			
	$T_{BB,h}$	$> 5 \times 10^{6}$ K			
	$R_{BB,h}$	< 0.29 km			
WABS*TBABS*(NSMAXG) (H atmosphere, $B = 10^{10}G$)	f	$0.19^{+0.04}_{-0.03}$	573.32 (675)	589.53	−10.82 (2%)
	$N_{H,SMC}$	$< 5^{*} \times 10^{21}$ cm^{-2}			
	T_{eff}	$1.8^{+0.5}_{-0.2} \times 10^{6}$ K			
	(R_{em}/R_{NS})	$0.9^{+0.1**}_{-0.3}$			
WABS*TBABS*(NSMAXG + PEGPWRLW) (H atmosphere, $B = 10^{10}G$)	f	$0.18^{+0.04}_{-0.02}$	562.42 (674)	580.69	−10.78 (3%)
	$N_{H,SMC}$	$< 3^{*} \times 10^{21}$ cm^{-2}			
	T_{eff}	$1.6^{+0.3}_{-0.1} \times 10^{6}$ K			
	(R_{em}/R_{NS})	$1.0^{+0.0**}_{-0.3}$			
	Γ	2.0			
	Flux$_{pl}$	$(3 \pm 2) \times 10^{-15}$ ergs cm^{-2} s^{-1}			
WABS*TBABS*(NSMAXG) (H atmosphere, $B = 10^{12}G$)	f	$0.19^{+0.04}_{-0.03}$	574.35 (675)	590.56	−10.82 (2%)
	$N_{H,SMC}$	$2^{+4*}_{-2}) \times 10^{21}$ cm^{-2}			
	T_{eff}	$1.8^{+0.6}_{-0.1} \times 10^{6}$ K			
	(R_{em}/R_{NS})	$1.0^{+0.0**}_{-0.6}$			

Table 4.4 Continued: Spectral analysis by simultaneously modelling the the individual spectra of NS in SN 1E 0102.2-7219.

Model	Parameters	Parameter Values	cstat (d.o.f)	AICc	log (CvM) (goodness)
WABS*TBABS*(NSMAXG + PEGPWRLW) (H atmosphere, $B = 10^{12}G$)	f	$0.18^{+0.04}_{-0.03}$	563.66 (674)	581.92	−10.75 (3%)
	$N_{H,SMC}$	$(1^{+3*}_{-1}) \times 10^{21}$ cm^{-2}			
	T_{eff}	$1.7^{+0.3}_{-0.1} \times 10^6$ K			
	(R_{em}/R_{NS})	$1.0^{+0.0**}_{-0.3}$			
	Γ	2.0			
	Flux$_{pl}$	$(3 \pm 2) \times 10^{-15}$ ergs cm^{-2} s^{-1}			
WABS*TBABS*(NSMAXG) (H atmosphere, $B = 10^{13}G$)	f	0.19 ± 0.04	571.99 (675)	588.20	−10.82/16 (2%)
	$N_{H,SMC}$	$1^{+5*}_{-1} \times 10^{21}$ cm^{-2}			
	T_{eff}	$1.9^{+0.4}_{-0.1} \times 10^6$ K			
	$(R_{em}/R_{NS})^2$	$0.9^{+0.1**}_{-0.4}$			
WABS*TBABS*(NSMAXG + PEGPWRLW) (H atmosphere, $B = 10^{13}G$)	f	$0.18^{0.04}_{-0.03}$	561.78 (674)	580.04	−10.79 (3%)
	$N_{H,SMC}$	$(4^{+15}_{-4}) \times 10^{21}$ cm^{-2}			
	T_{eff}	$1.7^{+0.3}_{-0.1} \times 10^6$ K			
	(R_{em}/R_{NS})	$1.0^{+0.0**}_{-0.3}$			
	Γ	2.0			
	Flux$_{pl}$	$(3 \pm 2) \times 10^{-15}$ ergs cm^{-2} s^{-1}			
WABS*TBABS*(NSMAXG) (C atmosphere, $B = 10^{12}G$)	f	$0.18^{+0.05}_{-0.04}$	560.44 (675)	576.65	−10.82/16 (2%)
	$N_{H,SMC}$	$3^{+17}_{-3} \times 10^{21}$ cm^{-2}			
	T_{eff}	$3.4^{+0.3}_{-0.7} \times 10^6$ K			
	(R_{em}/R_{NS})	$0.3^{+0.4}_{-0.1}$			

Table 4.5: Best-fitting spectral parameters for different background regions

Model	Parameters	Parameter values on modelling background from Region 1	Region 2	Region 3
WABS*TBABS*BBODYRAD	f	1.6 ± 0.3	1.4 ± 0.2	1.5 ± 0.2
	$N_{H,SMC}$	$3^{+22*}_{-3} \times 10^{21}$ cm^{-2}	$2^{+6*}_{-2} \times 10^{21}$ cm^{-2}	$1^{+4*}_{-1} \times 10^{21}$ cm^{-2}
	T_{BB}	$2.5^{+0.5}_{-0.9} \times 10^{6}$ K	$(3.1 \pm 0.6) \times 10^{6}$ K	$3.1^{+0.4}_{-0.3} \times 10^{6}$ K
	R_{BB}	4^{+7}_{-2} km	2^{+3}_{-1} km	3^{+2}_{-1} km
	C-statistic	30.05	37.47	57.28
	χ^2/d.o.f	30.18/16	36.74/16	56.92/16
WABS*TBABS*(BBODYRAD + PEGPWRLW	f	$1.4^{+0.4}_{-0.3}$	$1.3^{+0.2}_{-0.3}$	$1.4^{+0.2}_{-0.3}$
	$N_{H,SMC}$	$2^{+13*}_{-2} \times 10^{21}$ cm^{-2}	$8^{+8}_{-7} \times 10^{21}$ cm^{-2}	$1.0^{+0.4}_{-0.6} \times 10^{22}$ cm^{-2}
	T_{BB}	$2.3^{+0.3}_{-0.5} \times 10^{6}$ K	$1.9^{+0.6}_{-0.2} \times 10^{6}$ K	$1.9^{+0.3}_{-0.1} \times 10^{6}$ K
	R_{BB}	6^{+9}_{-3} km	11^{+4**}_{-7} km	15^{+0**}_{-8} km
	Flux$_{pl,\Gamma=2}$ (ergs cm^{-2} s^{-1})	$(2 \pm 1) \times 10^{-15}$	$3^{+2}_{-1} \times 10^{-15}$	$4^{+2}_{-1} \times 10^{-15}$ s^{-1}
	C-statistic	24.04	19.18	21.94
	χ^2/d.o.f	25.03/15	18.36/15	21.30/15

Table 5.5 Continued: best-fitting spectral parameters for different background regions

Model	Parameters	Parameter values on modelling background from Region 1	Region 2	Region 3
WABS*TBABS*BBODYRAD	f	0.8 ± 0.1	1.3 ± 0.2	$1.1^{+0.2}_{-0.1}$
	$N_{H,SMC}$	$< 8^* \times 10^{21}$ cm^{-2}	$1^{+6*}_{-1} \times 10^{21}$ cm^{-2}	$< 4^* \times 10^{21}$ cm^{-2}
	T_{BB}	$2.8^{+0.7}_{-0.5} \times 10^6$ K	$(2.6 \pm 0.4) \times 10^6$ K	$(3.3 \pm 0.4) \times 10^6$ K
	R_{BB}	3^{+3}_{-1} km	4^{+4}_{-1} km	$2.4^{+1.1}_{-0.7}$ km
	C-statistic	33.29	38.16	44.45
	χ^2/d.o.f	29.93/16	36.55/16	44.29/16
WABS*TBABS*(BBODYRAD + PEGPWRLW	f	$0.6^{+0.2}_{-0.1}$	$1.1^{+0.2}_{-0.3}$	$1.0^{+0.2}_{-0.3}$
	$N_{H,SMC}$	$2^{+7*}_{-2} \times 10^{21}$ cm^{-2}	$2^{+6*}_{-2} \times 10^{21}$ cm^{-2}	$4.1^{+8.6}_{-3.5} \times 10^{21}$ cm^{-2}
	T_{BB}	$(2.2 \pm 0.4) \times 10^6$ K	$2.1^{+0.4}_{-0.3} \times 10^6$ K	$2.2^{+0.3}_{-0.4} \times 10^6$ K
	R_{BB}	6^{+7}_{-3} km	7^{+5}_{-3} km	7^{+5}_{-3} km
	Flux$_{pl,\Gamma=2}$ (ergs cm^{-2} s^{-1})	$(3 \pm 1) \times 10^{-15}$	$(3 \pm 1) \times 10^{-15}$	$4^{+1}_{-2} \times 10^{-15}$
	C-statistic	18..24	23.59	20.39
	χ^2/d.o.f	17.30/15	23.83/15	19.85/15

Table 4.5 Continued: Best-fitting spectral parameters for different background regions

Model	Parameters	Parameter values on modelling background from Region 1	Region 2	Region 3
WABS*TBABS*(NSMAXG + PEGPWRLW) (H ATMOSPHERE, $B = 10^{13}$G)	f	$1.5^{+0.3}_{-0.2}$	$1.4^{+0.2}_{-0.1}$	$1.4^{+0.3}_{-0.2}$
	$N_{H,SMC}$	$1^{+3*}_{-1} \times 10^{21}$ cm^{-2}	$2.5^{+3.8}_{-2.3} \times 10^{21}$ cm^{-2}	$2.3^{+2.7}_{-1.8} \times 10^{21}$ cm^{-2}
	T_{eff}	$1.7^{+0.2}_{-0.1} \times 10^{6}$ K	$1.74^{+0.20}_{-0.08} \times 10^{6}$ K	$(1.8 \pm 0.1) \times 10^{6}$ K
	(R_{em}/R_{NS})	$1^{+0.0**}_{-0.3}$	$1^{+0.0**}_{-0.3}$	$1^{+0.0**}_{-0.2}$
	Flux$_{pl,\Gamma=2}$ (ergs cm^{-2} s^{-1})	$(1 \pm 1^{*}) \times 10^{-15}$	$1.5^{+1.5}_{-1.2} \times 10^{-15}$	$1.8^{+1.4}_{-1.3} \times 10^{-15}$ s^{-1}
	C-statistic	29.03	26.47	38.71
	χ^2/d.o.f	31.56/15	27.48/16	41.57/16
WABS*TBABS*NSMAXG (C ATMOSPHERE, $B = 10^{12}$G)	f	$1.6^{+0.2}_{-0.4}$	1.4 ± 0.2	1.5 ± 0.2
	$N_{H,SMC}$	$3^{+8*}_{-3} \times 10^{21}$ cm^{-2}	$9^{+9}_{-7} \times 10^{21}$ cm^{-2}	$7^{+7}_{-4} \times 10^{21}$ cm^{-2}
	T_{eff}	$(3.3 \pm 0.4) \times 10^{6}$ K	$3.0^{+0.4}_{-0.3} \times 10^{6}$ K	$3.1^{+0.4}_{-0.2} \times 10^{6}$ K
	(R_{em}/R_{NS})	$0.3^{+0.2}_{-0.1}$	$0.4^{+0.5}_{-0.1}$	$0.4^{+0.3}_{-0.1}$
	C-statistic	31.37	18.03	26.03
	χ^2/d.o.f	30.99/16	17.89/16	25.58/16

Table 4.5 Continued: Best-fitting spectral parameters for different background regions

Model	Parameters	Parameter values on modelling background from Region 4	Region 5	Region 6
WABS*TBABS*(NSMAXG + PEGPWRLW) (H ATMOSPHERE, $B = 10^{13}$G)	f	0.7 ± 0.1	1.2 ± 0.2	1.0 ± 0.2
	$N_{H,SMC}$	$1^{+3*}_{-1} \times 10^{21}$ cm^{-2}	$< 2^{*} \times 10^{21}$ cm^{-2}	$(2 \pm 2^{*}) \times 10^{21}$ cm^{-2}
	T_{eff}	$1.7^{+0.2}_{-0.1} \times 10^{6}$ K	$1.75^{+0.15}_{-0.07} \times 10^{6}$ K	$1.8^{+0.2}_{-0.1} \times 10^{6}$ K
	(R_{em}/R_{NS})	$1^{0.0*}_{-0.3}$	$1^{+0.0**}_{-0.2}$	$1^{+0.0**}_{-0.2}$
	$\text{Flux}_{pl,\Gamma=2}$ (ergs cm^{-2} s^{-1})	$1.6^{+1.4}_{-1.2} \times 10^{-15}$	$(1 \pm 1^{*}) \times 10^{-15}$	$1.7^{+1.5}_{-1.3} \times 10^{-15}$
	C-statistic	23.19	32.80	28.48
	χ^2/d.o.f	23.18/15	36.32/16	30.04/16
WABS*TBABS*NSMAXG (C ATMOSPHERE, $B = 10^{12}$G)	f	$0.9^{+0.1}_{-0.3}$	1.2 ± 0.2	$1.0^{+0.2}_{-0.1}$
	$N_{H,SMC}$	$2.11^{+0.55}_{-2.06} \times 10^{22}$ cm^{-2}	$3^{+7*}_{-3} \times 10^{21}$ cm^{-2}	$6^{+6}_{-4} \times 10^{21}$ cm^{-2}
	T_{eff}	$2.55^{+0.88}_{-0.09} \times 10^{6}$ K	$(3.2 \pm 0.3) \times 10^{6}$ K	$3.2^{+0.3}_{-0.2} \times 10^{6}$ K
	(R_{em}/R_{NS})	$1.0^{+0.0**}_{-0.7}$	$0.3^{+0.3}_{-0.1}$	$0.4^{+0.2}_{-0.1}$
	C-statistic	17.38	26.57	25.12
	χ^2/d.o.f	16.88/16	27.10/16	24.36/16

Chapter 5

Summary and conclusions

In this thesis we looked into the *Chandra* observations of four systems - the binary MSP 47 Tuc W, the candidate AGN in Henize 2–10 and candidate NS in SNR 1E0102.2-7219, each posing a different challenge in terms of analyzing the X-ray spectra and light curve. Through these works, we showed different ways in which we can properly account for the effects of statistical noise due to low counts, the response of instruments and bright background. Throughout this thesis, we used C-statistics for fitting the X-ray spectra rather than χ^2, since it allowed a finer binning of the data and is inherently designed for Poisson data. We use the AICc statistics for comparing spectral models with different numbers of degrees of freedom, as well as χ^2 and CvM statistics to test their goodness-of-fit.

Our analysis of the *Chandra* ACIS 2002 and 2014-15 X-ray light curves and spectra in Chap. 2 showed that the smaller effective area of the *Chandra* HRC detectors, especially at at higher energies (> 2 keV) was the reason for non-detection of X-ray variability in the 2004-05 *Chandra* observations of MSP 47 Tuc W. Studying the X-ray spectra revealed the presence of two components – a dominant IBS that could be fit with a power law of $\Gamma \sim 1.1$, and a thermal component which can be fit by a BB or an unmagnetized NS H atmosphere, with effective temperature $\sim 10^6$ K and emitting radius < 1.5 km, typical

of old MSPs with heated magnetic caps. Using the X-ray and optical light curves of 47 Tuc W, we probed the structure of the IBS and the heating of the companion star. Our analysis shows that the IBS is dominated by the wind from the companion, i.e. the IBS is wrapped around the MSP, and that the companion star is directly heated from the high energy particles of the pulsar wind nebula rather than from the IBS. Thus the observed dips in the X-ray light curve corresponding to the radio eclipses are due to Doppler beaming of radiation away from us.

In Chap. 3, we used minimally binned X-ray spectra of candidate AGN in Henize 2–10 and NGC 4178 to classify them as SNRs. We saw that a two-temperature collisionally ionized thermal plasma model or a non-equilibrium ionized plasma model, typical of young SNRs like Cas A, are $\sim 10^5$ times more likely fits to the observed X-ray spectrum of candidate AGN in Henize 2-10 as compared to a simple power-law model. We also found similar albeit less statistically significant results for the X-ray spectrum of the candidate AGN in NGC 4178, where the collisionally ionized plasma model was ~ 17 times better than a simple power-law model. Analyzing the minimally binned X-ray spectra allowed us to identify the Kα lines of Mg XI and Si XIII, which could not be detected in the broader binned spectral analysis of Henize 2–10 in Reines et al. (2016) and hardness ratio test of Secrest et al. (2012). Given the moderate resolution of CCDs, identification of generalized hardness ratios that can distinguish continuum dominated spectra from line dominated emission would allow us identify mis-classified candidate AGN even when they are faint.

We also provided further evidence for a NS in the SNR 1E0102.2-7219 in Chap. 4. Even when the background was extremely bright (contributing $\sim 50\%$ of the emission from the source region), we were able to show that a BB+PL model and a $B = 10^{12}$ G NS model with a C atmosphere best fit the observed X-ray spectra of the source and that the NS H atmosphere models gave poor fits. We also noted that the thermal luminosity of the NS is much higher than

other known CCOs and young pulsars and thus showed that the NS is powered by a decaying strong magnetic field or is slowly cooling after the supernova explosion.

Though the *Chandra* instrument has an excellent angular resolution, essential to study compact sources in dense environments like GCs, the nuclei of dwarf galaxies, and bright young SNRs, the small effective area limited our X-ray analysis. A higher effective area with similar the angular resolution (like the Lynx concept The Lynx Team 2018) would allow us to study the above sources in more detail. Higher numbers of X-ray photons would allow a better modeling of the IBS and study the thermal emission from the NS. The Lynx mission would also be able to identify line emission from SNRs more easily and thus distinguish them from AGN. Such identification of line emission from young SNRs could also allow us to filter out these energies when we want to study the underlying emission from its NS.

Bibliography

A. de Luca, P. A. Caraveo, S. Mereghetti, M. Negroni, and G. F. Bignami (2005). "On the Polar Caps of the Three Musketeers." In: *ApJ* 623, pp. 1051–1069. DOI: 10.1086/428567.

A. de Luca, P. A. Caraveo, S. Mereghetti, A. Tiengo, and G. F. Bignami (2006). "A Long-Period, Violently Variable X-ray Source in a Young Supernova Remnant." In: *Science* 313, pp. 814–817. DOI: 10.1126/science.1129185.

Abel, N. P. and S. Satyapal (2008). "[Ne V] Emission in Optically Classified Starbursts." In: *ApJ* 678, 686-692, pp. 686–692. DOI: 10.1086/529013.

Akaike, H. (1973). " Information theory and the maximum likelihood principle." In: *2nd International Symposium on Information Theory*. Ed. by B. N. Petro and F. Csäki. Akadémiai Kiadó:Budapest, pp. 267–281.

Akaike, H. (1974). "A New Look at the Statistical Model Identification." In: *IEEE Transactions on Automatic Control* 19, pp. 716–723.

Al Noori, Hind, Mallory S. E. Roberts, Rodrigo A. Torres, Maura A. McLaughlin, Peter A. Gentile, Jason W. T. Hessels, Paul S. Ray, Matthew Kerr, and Rene P. Breton (2018). "X-Ray and Optical Studies of the Redback System PSR J2129-0429." In: *ApJ* 861.2, 89, p. 89. DOI: 10.3847/1538-4357/aac828.

Alan, Neslihan, Sangwook Park, and Selçuk Bilir (2019). "A Detailed Archival CHANDRA Study of the Young Core-collapse Supernova Remnant 1E 0102.2-7219 in the Small Magellanic Cloud." In: *ApJ* 873, 53, p. 53. DOI: 10.3847/1538-4357/aaf882.

Alcock, C. and A. Illarionov (1980). "The surface chemistry of stars. I - Diffusion of heavy ions in white dwarf envelopes. II - Fractionated accretion of interstellar matter." In: *ApJ* 235, pp. 534–553. DOI: 10.1086/157656.

Allard, F., D. Homeier, and B. Freytag (2012). "Models of very-low-mass stars, brown dwarfs and exoplanets." In: *Philosophical Transactions of the Royal Society of London Series A* 370, pp. 2765–2777. DOI: 10.1098/rsta.2011.0269.

Alp, D., J. Larsson, C. Fransson, M. Gabler, A. Wongwathanarat, and H.-T. Janka (2018). "X-Ray Absorption in Young Core-collapse Supernova Remnants." In: *ApJ* 864, 175, p. 175. DOI: 10.3847/1538-4357/aad737.

Alpar, M. A., A. F. Cheng, M. A. Ruderman, and J. Shaham (1982). "A new class of radio pulsars." In: *Nature* 300.5894, pp. 728–730. DOI: 10.1038/300728a0.

Ambrosino, F. et al. (2017). "Optical pulsations from a transitional millisecond pulsar." In: *Nature Astronomy* 1, pp. 854–858. DOI: 10.1038/s41550-017-0266-2.

Anders, E. and M. Ebihara (1982). "Solar-system abundances of the elements." In: *Geochimica et Cosmochimica Acta* 46, pp. 2363–2380. DOI: 10.1016/0016-7037(82)90208-3.

Ångström, A.J. (1853). *Optiska undersökningar*. Svenska Vetenskapakademien. URL: https://books.google.ca/books?id=4mxpmgEACAAJ.

Archibald, A. M. et al. (2009). "A Radio Pulsar/X-ray Binary Link." In: *Science* 324, p. 1411. DOI: 10.1126/science.1172740.

Archibald, A. M. et al. (2015). "Accretion-powered Pulsations in an Apparently Quiescent Neutron Star Binary." In: *ApJ* 807, 62, p. 62. DOI: 10.1088/0004-637X/807/1/62.

Archibald, R. F., V. M. Kaspi, S. P. Tendulkar, and P. Scholz (2016). "A Magnetar-like Outburst from a High-B Radio Pulsar." In: *ApJ* 829, L21, p. L21. DOI: 10.3847/2041-8205/829/1/L21.

Baade, W. and F. Zwicky (1934). "On Super-novae." In: *Proceedings of the National Academy of Science* 20, pp. 254–259. DOI: 10.1073/pnas.20.5.254.

Backer, D. C., S. R. Kulkarni, C. Heiles, M. M. Davis, and W. M. Goss (1982). "A millisecond pulsar." In: *Nature* 300.5893, pp. 615–618. DOI: 10.1038/300615a0.

Badenes, Carles, Kazimierz J. Borkowski, John P. Hughes, Una Hwang, and Eduardo Bravo (2006). "Constraints on the Physics of Type Ia Supernovae from the X-Ray Spectrum of the Tycho Supernova Remnant." In: *ApJ* 645.2, pp. 1373–1391. DOI: 10.1086/504399.

Bahramian, Arash et al. (2017). "The ultracompact nature of the black hole candidate X-ray binary 47 Tuc X9." In: *MNRAS* 467.2, pp. 2199–2216. DOI: 10.1093/mnras/stx166.

Baldassare, V. F., A. E. Reines, E. Gallo, and J. E. Greene (2015). "A ∼50,000 $M_{\odot}$ Solar Mass Black Hole in the Nucleus of RGG 118." In: *ApJ* 809, L14, p. L14. DOI: 10.1088/2041-8205/809/1/L14.

Baldassare, V. F., A. E. Reines, E. Gallo, J. E. Greene, O. Graur, M. Geha, K. Hainline, C. M. Carroll, and R. C. Hickox (2016). "Multi-epoch Spectroscopy of Dwarf Galaxies with AGN Signatures: Identifying Sources with Persistent Broad Hα Emission." In: *ApJ* 829, 57, p. 57. DOI: 10.3847/0004-637X/829/1/57.

Baldwin, J. A., M. M. Phillips, and R. Terlevich (1981). "Classification parameters for the emission-line spectra of extragalactic objects." In: *PASP* 93, pp. 5–19. DOI: 10.1086/130766.

Barth, A. J., J. E. Greene, and L. C. Ho (2005). "Dwarf Seyfert 1 Nuclei and the Low-Mass End of the M_{BH} - σ Relation." In: *ApJ* 619, pp. L151–L154. DOI: 10.1086/428365.

Barth, A. J., L. C. Ho, R. E. Rutledge, and W. L. W. Sargent (2004). "POX 52: A Dwarf Seyfert 1 Galaxy with an Intermediate-Mass Black Hole." In: *ApJ* 607, pp. 90–102. DOI: 10.1086/383302.

Bassa, C. G. et al. (2014). "A state change in the low-mass X-ray binary XSS J12270-4859." In: *MNRAS* 441, pp. 1825–1830. DOI: 10.1093/mnras/stu708.

Becker, W. and J. Trümper (1993). "Detection of pulsed X-rays from the binary millisecond pulsar J0437 - 4715." In: *Nature* 365, pp. 528–530. DOI: 10.1038/365528a0.

Becker, Werner, ed. (2009). *Neutron Stars and Pulsars*. Vol. 357. DOI: 10.1007/978-3-540-76965-1.

Bednarek, W. (2014). "Modulated gamma-ray emission from compact millisecond pulsar binary systems." In: *A&A* 561, A116, A116. DOI: 10.1051/0004-6361/201322595.

Benvenuto, O. G., M. A. De Vito, and J. E. Horvath (2014). "Understanding the Evolution of Close Binary Systems with Radio Pulsars." In: *ApJ* 786, L7, p. L7. DOI: 10.1088/2041-8205/786/1/L7.

Benvenuto, O. G., M. A. De Vito, and J. E. Horvath (2015). "The Quasi-Roche Lobe Overflow State in the Evolution of Close Binary Systems Containing a Radio Pulsar." In: *ApJ* 798, 44, p. 44. DOI: 10.1088/0004-637X/798/1/44.

Bernal, C. G., D. Page, and W. H. Lee (2013). "Hypercritical Accretion onto a Newborn Neutron Star and Magnetic Field Submergence." In: *ApJ* 770, 106, p. 106. DOI: 10.1088/0004-637X/770/2/106.

Bhattacharya, D. and E. P. J. van den Heuvel (1991). "Formation and evolution of binary and millisecond radio pulsars." In: *Phys. Rep.* 203.1-2, pp. 1–124. DOI: 10.1016/0370-1573(91)90064-S.

Bhattacharya, S., C. O. Heinke, A. I. Chugunov, P. C. C. Freire, A. Ridolfi, and S. Bogdanov (2017). "Chandra studies of the globular cluster 47 Tucanae: A deeper X-ray source catalogue, five new X-ray counterparts to millisecond

radio pulsars, and new constraints to r-mode instability window." In: *MNRAS* 472, pp. 3706–3721. DOI: 10.1093/mnras/stx2241.

Blair, William P., Jon A. Morse, John C. Raymond, Robert P. Kirshner, John P. Hughes, Michael A. Dopita, Ralph S. Sutherland, Knox S. Long, and P. Frank Winkler (2000). "Hubble Space Telescope Observations of Oxygen-rich Supernova Remnants in the Magellanic Clouds. II. Elemental Abundances in N132D and 1E 0102.2-7219." In: *ApJ* 537, pp. 667–689. DOI: 10.1086/309077.

Bogdanov, S. (2014). "Modeling the X-Rays from the Central Compact Object PSR J1852+0040 in Kesteven 79: Evidence for a Strongly Magnetized Neutron Star." In: *ApJ* 790, 94, p. 94. DOI: 10.1088/0004-637X/790/2/94.

Bogdanov, S., A. M. Archibald, J. W. T. Hessels, V. M. Kaspi, D. Lorimer, M. A. McLaughlin, S. M. Ransom, and I. H. Stairs (2011). "A Chandra X-Ray Observation of the Binary Millisecond Pulsar PSR J1023+0038." In: *ApJ* 742, 97, p. 97. DOI: 10.1088/0004-637X/742/2/97.

Bogdanov, S., J. E. Grindlay, C. O. Heinke, F. Camilo, P. C. C. Freire, and W. Becker (2006). "Chandra X-Ray Observations of 19 Millisecond Pulsars in the Globular Cluster 47 Tucanae." In: *ApJ* 646, pp. 1104–1115. DOI: 10.1086/505133.

Bogdanov, S., J. E. Grindlay, and M. van den Berg (2005). "An X-Ray Variable Millisecond Pulsar in the Globular Cluster 47 Tucanae: Closing the Link to Low-Mass X-Ray Binaries." In: *ApJ* 630, pp. 1029–1036. DOI: 10.1086/432249.

Bogdanov, S., C. O. Heinke, F. Özel, and T. Güver (2016). "Neutron Star Mass-Radius Constraints of the Quiescent Low-mass X-Ray Binaries X7 and X5 in the Globular Cluster 47 Tuc." In: *ApJ* 831, 184, p. 184. DOI: 10.3847/0004-637X/831/2/184.

Bogdanov, S., M. van den Berg, C. O. Heinke, H. N. Cohn, P. M. Lugger, and J. E. Grindlay (2010). "A Chandra X-ray Observatory Study of PSR

J1740-5340 and Candidate Millisecond Pulsars in the Globular Cluster NGC 6397." In: *ApJ* 709, pp. 241–250. DOI: 10.1088/0004-637X/709/1/241.

Bogdanov, S. et al. (2015). "Coordinated X-Ray, Ultraviolet, Optical, and Radio Observations of the PSR J1023+0038 System in a Low-mass X-Ray Binary State." In: *ApJ* 806, 148, p. 148. DOI: 10.1088/0004-637X/806/2/148.

Boltzmann, L. (1872). *Weitere Studien über das Wärmegleichgewicht unter Gasmolekülen: vorgelegt in der Sitzung am 10. October 1872*. k. und k. Hof- und Staatsdr. URL: https://books.google.ca/books?id=Fmy5PgAACAAJ.

Booth, C. M. and J. Schaye (2013). "The interaction between feedback from active galactic nuclei and supernovae." In: *Scientific Reports*, 1738, p. 1738. DOI: 10.1038/srep01738.

Bradt, Hale (2014). *Astrophysics Processes*. ISBN: 9781139469586.

Breton, R. P., S. A. Rappaport, M. H. van Kerkwijk, and J. A. Carter (2012). "KOI 1224: A Fourth Bloated Hot White Dwarf Companion Found with Kepler." In: *ApJ* 748, 115, p. 115. DOI: 10.1088/0004-637X/748/2/115.

Breton, R. P., M. H. van Kerkwijk, M. S. E. Roberts, J. W. T. Hessels, F. Camilo, M. A. McLaughlin, S. M. Ransom, P. S. Ray, and I. H. Stairs (2013). "Discovery of the Optical Counterparts to Four Energetic Fermi Millisecond Pulsars." In: *ApJ* 769.2, 108, p. 108. DOI: 10.1088/0004-637X/769/2/108.

Brown, Edward F., Lars Bildsten, and Robert E. Rutledge (1998). "Crustal Heating and Quiescent Emission from Transiently Accreting Neutron Stars." In: *ApJ* 504, pp. L95–L98. DOI: 10.1086/311578.

Burrows, David N., Joanne E. Hill, John A. Nousek, Alan A. Wells, Guido Chincarini, Anthony F. Abbey, Andrew P. Beardmore, J. Bosworth, Heinrich W. Bräuninger, and Wolfgang Burkert (2004). "The Swift X-Ray Telescope." In: *X-Ray and Gamma-Ray Instrumentation for Astronomy XIII*. Ed. by Kathryn A. Flanagan and Oswald H. W. Siegmund. Vol. 5165. Society of Photo-Optical Instrumentation Engineers (SPIE) Conference Series, pp. 201–216. DOI: 10.1117/12.504868.

Cadelano, M., C. Pallanca, F. R. Ferraro, M. Salaris, E. Dalessandro, B. Lanzoni, and P. C. C. Freire (2015). "Optical Identification of He White Dwarfs Orbiting Four Millisecond Pulsars in the Globular Cluster 47 Tucanae." In: *ApJ* 812, 63, p. 63. DOI: 10.1088/0004-637X/812/1/63.

Callanan, P. J., J. van Paradijs, and R. Rengelink (1995). "The orbital light curve of PSR 1957 + 20." In: *ApJ* 439, pp. 928–932. DOI: 10.1086/175229.

Cameron, P. B., R. E. Rutledge, F. Camilo, L. Bildsten, S. M. Ransom, and S. R. Kulkarni (2007). "Variability of 19 Millisecond Pulsars in 47 Tucanae with Chandra HRC-S." In: *ApJ* 660, pp. 587–594. DOI: 10.1086/512229.

Camilo, F., D. R. Lorimer, P. Freire, A. G. Lyne, and R. N. Manchester (2000). "Observations of 20 Millisecond Pulsars in 47 Tucanae at 20 Centimeters." In: *ApJ* 535, pp. 975–990. DOI: 10.1086/308859.

Cash, W. (1979). "Parameter estimation in astronomy through application of the likelihood ratio." In: *ApJ* 228, pp. 939–947. DOI: 10.1086/156922.

Cavanaugh, Joseph E. (1997). "Unifying the derivations for the Akaike and corrected Akaike information criteria." In: *Statistics & Probability Letters* 33.2, pp. 201–208. ISSN: 0167-7152. DOI: 10.1016/S0167-7152(96)00128-9.

Chang, Chulhoon, George G. Pavlov, Oleg Kargaltsev, and Yurii A. Shibanov (2012). "X-Ray Observations of the Young Pulsar J1357—6429 and Its Pulsar Wind Nebula." In: *ApJ* 744.2, 81, p. 81. DOI: 10.1088/0004-637X/744/2/81.

Chang, P., L. Bildsten, and P. Arras (2010). "Diffusive Nuclear Burning of Helium on Neutron Stars." In: *ApJ* 723, pp. 719–728. DOI: 10.1088/0004-637X/723/1/719.

Chang, Philip, Phil Arras, and Lars Bildsten (2004). "Hydrogen Burning on Magnetar Surfaces." In: *ApJ* 616, pp. L147–L150. DOI: 10.1086/426789.

Chilingarian, I. V., I. Y. Katkov, I. Y. Zolotukhin, K. A. Grishin, Y. Beletsky, K. Boutsia, and D. J. Osip (2018). "A Population of Bona Fide Intermediate Mass Black Holes Identified as Low Luminosity Active Galactic Nuclei." In: *ArXiv e-prints*. arXiv: 1805.01467.

Compton, A. H. (1923). "A Quantum Theory of the Scattering of X-rays by Light Elements." In: *Physical Review* 21, pp. 483–502. DOI: 10.1103/PhysRev.21.483.

Coti Zelati, Francesco, Alessandro Papitto, Domitilla de Martino, David A. H. Buckley, Alida Odendaal, Jian Li, Thomas D. Russell, Diego F. Torres, Simona M. Mazzola, and Enrico Bozzo (2019). "Prolonged sub-luminous state of the new transitional pulsar candidate CXOU J110926.4-650224." In: *A&A* 622, A211, A211. DOI: 10.1051/0004-6361/201834835.

Cramér, Harald (1928). "On the composition of elementary errors." In: *Scandinavian Actuarial Journal* 1928.1, pp. 13–74. DOI: 10.1080/03461238.1928.10416862.

Cresci, G., L. Vanzi, E. Telles, G. Lanzuisi, M. Brusa, M. Mingozzi, M. Sauvage, and K. Johnson (2017). "The MUSE view of He 2-10: No AGN ionization but a sparkling starburst." In: *A&A* 604, A101, A101. DOI: 10.1051/0004-6361/201730876.

D. de Martino, M. Falanga, J.-M. Bonnet-Bidaud, T. Belloni, M. Mouchet, N. Masetti, I. Andruchow, S. A. Cellone, K. Mukai, and G. Matt (2010). "The intriguing nature of the high-energy gamma ray source XSS J12270-4859." In: *A&A* 515, A25, A25. DOI: 10.1051/0004-6361/200913802.

D. de Martino et al. (2013). "X-ray follow-ups of XSS J12270-4859: a low-mass X-ray binary with gamma-ray Fermi-LAT association." In: *A&A* 550, A89, A89. DOI: 10.1051/0004-6361/201220393.

D'Aì, A. et al. (2016). "Evidence for the magnetar nature of 1E 161348-5055 in RCW 103." In: *MNRAS* 463, pp. 2394–2404. DOI: 10.1093/mnras/stw2023.

D'Amico, N., A. Possenti, R. N. Manchester, J. Sarkissian, A. G. Lyne, and F. Camilo (2001). "An Eclipsing Millisecond Pulsar with a Possible Main-Sequence Companion in NGC 6397." In: *ApJ* 561, pp. L89–L92. DOI: 10.1086/324562.

Dashyan, G., J. Silk, G. A. Mamon, Y. Dubois, and T. Hartwig (2018). "AGN feedback in dwarf galaxies?" In: *MNRAS* 473, pp. 5698–5703. DOI: 10.1093/mnras/stx2716.

Djorgovski, S. and C. R. Evans (1988). "Photometry and the light curve of the optical counterpart of the eclipsing millisecond pulsar 1957+20." In: *ApJ* 335, pp. L61–L65. DOI: 10.1086/185340.

Dopita, M. A., I. R. Tuohy, and D. S. Mathewson (1981). "An oxygen-rich young supernova remnant in the Small Magellanic Cloud." In: *ApJ* 248, pp. L105–L108. DOI: 10.1086/183635.

Doroshenko, V., V. Suleimanov, and A. Santangelo (2018). "CXOU J160103.1-513353: another central compact object with a carbon atmosphere?" In: *A&A* 618, A76, A76. DOI: 10.1051/0004-6361/201833271.

Du, P., J.-M. Wang, and Z.-X. Zhang (2017). "Hidden Broad-line Regions in Seyfert 2 Galaxies: From the Spectropolarimetric Perspective." In: *ApJ* 840, L6, p. L6. DOI: 10.3847/2041-8213/aa6d7b.

Edmonds, P. D., R. L. Gilliland, F. Camilo, C. O. Heinke, and J. E. Grindlay (2002). "A Millisecond Pulsar Optical Counterpart with Large-Amplitude Variability in the Globular Cluster 47 Tucanae." In: *ApJ* 579, pp. 741–751. DOI: 10.1086/342985.

Elder, F. R., A. M. Gurewitsch, R. V. Langmuir, and H. C. Pollock (1947). "Radiation from Electrons in a Synchrotron." In: *Physical Review* 71, pp. 829–830. DOI: 10.1103/PhysRev.71.829.5.

Filippenko, A. V. and W. L. W. Sargent (1989). "Discovery of an extremely low luminosity Seyfert 1 nucleus in the dwarf galaxy NGC 4395." In: *ApJ* 342, pp. L11–L14. DOI: 10.1086/185472.

Filippenko, Alexei V. (1989). "The "Seyfert 1" Optical Spectra of the Type II Supernovae 1987F and 1988I." In: *AJ* 97, p. 726. DOI: 10.1086/115018.

Finkelstein, Steven L. et al. (2006). "Optical Structure and Proper-Motion Age of the Oxygen-rich Supernova Remnant 1E 0102-7219 in the Small Magellanic Cloud." In: *ApJ* 641, pp. 919–929. DOI: 10.1086/500570.

Foster, A. R., L. Ji, R. K. Smith, and N. S. Brickhouse (2012). "Updated Atomic Data and Calculations for X-Ray Spectroscopy." In: *ApJ* 756.2, 128, p. 128. DOI: 10.1088/0004-637X/756/2/128.

Freire, P. C. C. (2005). "Eclipsing Binary Pulsars." In: *Binary Radio Pulsars*. Ed. by F. A. Rasio and I. H. Stairs. Vol. 328. Astronomical Society of the Pacific Conference Series, p. 405. eprint: astro-ph/0404105.

Freire, P. C. C. et al. (2017). "Long-term observations of the pulsars in 47 Tucanae - II. Proper motions, accelerations and jerks." In: *MNRAS* 471, pp. 857–876. DOI: 10.1093/mnras/stx1533.

Fruscione, Antonella et al. (2006). "CIAO: Chandra's data analysis system." In: *Society of Photo-Optical Instrumentation Engineers (SPIE) Conference Series*. Vol. 6270. Society of Photo-Optical Instrumentation Engineers (SPIE) Conference Series, p. 62701V. DOI: 10.1117/12.671760.

Gaensler, B. M. and P. O. Slane (2006). "The Evolution and Structure of Pulsar Wind Nebulae." In: *ARA&A* 44, pp. 17–47. DOI: 10.1146/annurev.astro.44.051905.092528.

Garmire, Gordon P., Mark W. Bautz, Peter G. Ford, John A. Nousek, and Jr. Ricker George R. (2003). "Advanced CCD imaging spectrometer (ACIS) instrument on the Chandra X-ray Observatory." In: *X-Ray and Gamma-Ray Telescopes and Instruments for Astronomy*. Ed. by Joachim E. Truemper and Harvey D. Tananbaum. Vol. 4851. Society of Photo-Optical Instrumentation Engineers (SPIE) Conference Series, pp. 28–44. DOI: 10.1117/12.461599.

Gavriil, F. P., M. E. Gonzalez, E. V. Gotthelf, V. M. Kaspi, M. A. Livingstone, and P. M. Woods (2008). "Magnetar-Like Emission from the Young Pulsar in Kes 75." In: *Science* 319, p. 1802. DOI: 10.1126/science.1153465.

Ghisellini, Gabriele (2013). *Radiative Processes in High Energy Astrophysics*. Lecture Notes in Physics. Springer International Publishing. ISBN: 978-3-319-00612-3. DOI: 10.1007/978-3-319-00612-3.

Giacconi, Riccardo, Herbert Gursky, Frank R. Paolini, and Bruno B. Rossi (1962). "Evidence for x Rays From Sources Outside the Solar System." In: *Phys. Rev. Lett.* 9.11, pp. 439–443. DOI: 10.1103/PhysRevLett.9.439.

Gonzalez, M. E., V. M. Kaspi, F. Camilo, B. M. Gaensler, and M. J. Pivovaroff (2005). "Unusual Pulsed X-Ray Emission from the Young, High Magnetic Field Pulsar PSR J1119-6127." In: *ApJ* 630, pp. 489–494. DOI: 10.1086/432032.

Gotthelf, E. V., J. P. Halpern, and J. Alford (2013). "The Spin-down of PSR J0821-4300 and PSR J1210-5226: Confirmation of Central Compact Objects as Anti-magnetars." In: *ApJ* 765, 58, p. 58. DOI: 10.1088/0004-637X/765/1/58.

Greene, J. E. and L. C. Ho (2004). "Active Galactic Nuclei with Candidate Intermediate-Mass Black Holes." In: *ApJ* 610, pp. 722–736. DOI: 10.1086/421719.

Greene, J. E. and L. C. Ho (2005). "Estimating Black Hole Masses in Active Galaxies Using the Hα Emission Line." In: *ApJ* 630, pp. 122–129. DOI: 10.1086/431897.

Greene, J. E. and L. C. Ho (2007). "A New Sample of Low-Mass Black Holes in Active Galaxies." In: *ApJ* 670, pp. 92–104. DOI: 10.1086/522082.

Greene, J. E., L. C. Ho, and A. J. Barth (2008). "Black Holes in Pseudobulges and Spheroidals: A Change in the Black Hole-Bulge Scaling Relations at Low Mass." In: *ApJ* 688, pp. 159–179. DOI: 10.1086/592078.

Gregory, P. C. and T. J. Loredo (1992). "A new method for the detection of a periodic signal of unknown shape and period." In: *ApJ* 398, pp. 146–168. DOI: 10.1086/171844.

Grindlay, J. E., C. Heinke, P. D. Edmonds, and S. S. Murray (2001). "High-Resolution X-ray Imaging of a Globular Cluster Core: Compact Binaries in 47Tuc." In: *Science* 292, pp. 2290–2295. DOI: 10.1126/science.1061135.

Hainline, K. N., A. E. Reines, J. E. Greene, and D. Stern (2016). "Mid-infrared Colors of Dwarf Galaxies: Young Starbursts Mimicking Active Galactic Nuclei." In: *ApJ* 832, 119, p. 119. DOI: 10.3847/0004-637X/832/2/119.

Halpern, J. P. and E. V. Gotthelf (2010a). "Spin-Down Measurement of PSR J1852+0040 in Kesteven 79: Central Compact Objects as Anti-Magnetars." In: *ApJ* 709, pp. 436–446. DOI: 10.1088/0004-637X/709/1/436.

Halpern, J. P. and E. V. Gotthelf (2010b). "Two Magnetar Candidates in HESS Supernova Remnants." In: *ApJ* 710, pp. 941–947. DOI: 10.1088/0004-637X/710/2/941.

Harrison, Fiona A., William W. Craig, Finn E. Christensen, Charles J. Hailey, William W. Zhang, Steven E. Boggs, Daniel Stern, W. Rick Cook, Karl Forster, and Paolo Giommi (2013). "The Nuclear Spectroscopic Telescope Array (NuSTAR) High-energy X-Ray Mission." In: *ApJ* 770.2, 103, p. 103. DOI: 10.1088/0004-637X/770/2/103.

Hebbar, Pavan R., Craig O. Heinke, Gregory R. Sivakoff, and Aarran W. Shaw (2019). "X-ray spectroscopy of the candidate AGNs in Henize 2-10 and NGC 4178: likely supernova remnants." In: *MNRAS* 485.4, pp. 5604–5615. DOI: 10.1093/mnras/stz553.

Heinke, C. O., J. E. Grindlay, P. D. Edmonds, H. N. Cohn, P. M. Lugger, F. Camilo, S. Bogdanov, and P. C. Freire (2005). "A Deep Chandra Survey of the Globular Cluster 47 Tucanae: Catalog of Point Sources." In: *ApJ* 625, pp. 796–824. DOI: 10.1086/429899.

Heinke, C. O., G. B. Rybicki, R. Narayan, and J. E. Grindlay (2006). "A Hydrogen Atmosphere Spectral Model Applied to the Neutron Star X7 in the Globular Cluster 47 Tucanae." In: *ApJ* 644, pp. 1090–1103. DOI: 10.1086/503701.

Hester, J. J. (2008). "The Crab Nebula : an astrophysical chimera." In: *ARA&A* 46, pp. 127–155. DOI: 10.1146/annurev.astro.45.051806.110608.

Hill, A. B. et al. (2011). "The bright unidentifiedγ-ray source 1FGL J1227.9-4852: can it be associated with a low-mass X-ray binary?" In: *MNRAS* 415, pp. 235–243. DOI: 10.1111/j.1365-2966.2011.18692.x.

Ho, L. C., A. V. Filippenko, and W. L. Sargent (1995). "A search for 'dwarf' Seyfert nuclei. 2: an optical spectral atlas of the nuclei of nearby galaxies." In: *ApJS* 98, pp. 477–593. DOI: 10.1086/192170.

Ho, L. C., A. V. Filippenko, and W. L. W. Sargent (1997). "A Search for "Dwarf" Seyfert Nuclei. III. Spectroscopic Parameters and Properties of the Host Galaxies." In: *ApJS* 112, pp. 315–390. DOI: 10.1086/313041.

Ho, W. C. G. (2011). "Evolution of a buried magnetic field in the central compact object neutron stars." In: *MNRAS* 414, pp. 2567–2575. DOI: 10.1111/j.1365-2966.2011.18576.x.

Ho, W. C. G. and C. O. Heinke (2009). "A neutron star with a carbon atmosphere in the Cassiopeia A supernova remnant." In: *Nature* 462, pp. 71–73. DOI: 10.1038/nature08525.

Ho, W. C. G., D. L. Kaplan, P. Chang, M. van Adelsberg, and A. Y. Potekhin (2007). "Magnetic hydrogen atmosphere models and the neutron star RX J1856.5-3754." In: *MNRAS* 375, pp. 821–830. DOI: 10.1111/j.1365-2966.2006.11376.x.

Ho, Wynn C. G., Khaled G. Elshamouty, Craig O. Heinke, and Alexander Y. Potekhin (2015). "Tests of the nuclear equation of state and superfluid and superconducting gaps using the Cassiopeia A neutron star." In: *Phys. Rev. C* 91, 015806, p. 015806. DOI: 10.1103/PhysRevC.91.015806.

Ho, Wynn C. G., Alexander Y. Potekhin, and Gilles Chabrier (2008). "Model X-Ray Spectra of Magnetic Neutron Stars with Hydrogen Atmospheres." In: *ApJS* 178, pp. 102–109. DOI: 10.1086/589238.

Holt, S. S., E. V. Gotthelf, H. Tsunemi, and H. Negoro (1994). "ASCA observations of Cassiopeia A." In: *PASJ* 46, pp. L151–L155.

Hong, J., E. M. Schlegel, and J. E. Grindlay (2004). "New Spectral Classification Technique for X-Ray Sources: Quantile Analysis." In: *ApJ* 614, pp. 508–517. DOI: 10.1086/423445.

Hu, Chin-Ping, C. -Y. Ng, J. Takata, R. M. Shannon, and S. Johnston (2017). "Chandra Phase-resolved Spectroscopy of the High Magnetic Field Pulsar B1509-58." In: *ApJ* 838, 156, p. 156. DOI: 10.3847/1538-4357/aa67e3.

Hughes, John P., Cara E. Rakowski, David N. Burrows, and Patrick O. Slane (2000a). "Nucleosynthesis and Mixing in Cassiopeia A." In: *ApJ* 528.2, pp. L109–L113. DOI: 10.1086/312438.

Hughes, John P., Patrick O. Slane, and Paul P. Plucinsky (2000b). "Discovery of X-Ray Emission from G328.4+0.2, a Crab-like Supernova Remnant." In: *ApJ* 542.1, pp. 386–391. DOI: 10.1086/309532.

Hui, C. Y., C. P. Hu, S. M. Park, J. Takata, K. L. Li, P. H. T. Tam, L. C. C. Lin, A. K. H. Kong, K. S. Cheng, and C. Kim (2015). "Exploring the Intrabinary Shock from the Redback Millisecond Pulsar PSR J2129-0429." In: *ApJ* 801, L27, p. L27. DOI: 10.1088/2041-8205/801/2/L27.

Humphrey, Philip J., Wenhao Liu, and David A. Buote (2009). "χ^2 and Poissonian Data: Biases Even in the High-Count Regime and How to Avoid Them." In: *ApJ* 693.1, pp. 822–829. DOI: 10.1088/0004-637X/693/1/822.

Jahnke, K. and A. V. Macciò (2011). "The Non-causal Origin of the Black-hole-galaxy Scaling Relations." In: *ApJ* 734, 92, p. 92. DOI: 10.1088/0004-637X/734/2/92.

Jansen, F., D. Lumb, B. Altieri, J. Clavel, M. Ehle, C. Erd, C. Gabriel, M. Guainazzi, P. Gondoin, and R. Much (2001). "XMM-Newton observatory. I. The spacecraft and operations." In: *A&A* 365, pp. L1–L6. DOI: 10.1051/0004-6361:20000036.

Jansen, F., A. Smith, J. A. M. Bleeker, P. A. J. de Korte, A. Peacock, and N. E. White (1988). "EXOSAT Observations of the Cassiopeia A Supernova Remnant." In: *ApJ* 331, p. 949. DOI: 10.1086/166612.

Jiang, Y.-F., J. E. Greene, and L. C. Ho (2011). "Black Hole Mass and Bulge Luminosity for Low-mass Black Holes." In: *ApJ* 737, L45, p. L45. DOI: 10.1088/2041-8205/737/2/L45.

Jones, Eric, Travis Oliphant, Pearu Peterson, et al. (2001). *SciPy: Open source scientific tools for Python*. URL: http://www.scipy.org/.

Kalberla, P. M. W., W. B. Burton, D. Hartmann, E. M. Arnal, E. Bajaja, R. Morras, and W. G. L. Pöppel (2005). "The Leiden/Argentine/Bonn (LAB) Survey of Galactic HI. Final data release of the combined LDS and IAR surveys with improved stray-radiation corrections." In: *A&A* 440, pp. 775–782. DOI: 10.1051/0004-6361:20041864.

Kandel, D., Roger W. Romani, and Hongjun An (2019). "The Synchrotron Emission Pattern of Intrabinary Shocks." In: *ApJ* 879.2, 73, p. 73. DOI: 10.3847/1538-4357/ab24d9.

Kaplan, D. L., D. A. Frail, B. M. Gaensler, E. V. Gotthelf, S. R. Kulkarni, P. O. Slane, and A. Nechita (2004). "An X-Ray Search for Compact Central Sources in Supernova Remnants. I. SNRS G093.3+6.9, G315.4-2.3, G084.2+0.8, and G127.1+0.5." In: *ApJS* 153, pp. 269–315. DOI: 10.1086/421065.

Kaplan, D. L., B. M. Gaensler, S. R. Kulkarni, and P. O. Slane (2006). "An X-Ray Search for Compact Central Sources in Supernova Remnants. II. Six Large-Diameter SNRs." In: *ApJS* 163, pp. 344–371. DOI: 10.1086/501441.

Kargaltsev, O. and G. G. Pavlov (2008). "Pulsar Wind Nebulae in the Chandra Era." In: *40 Years of Pulsars: Millisecond Pulsars, Magnetars and More*. Ed. by C. Bassa, Z. Wang, A. Cumming, and V. M. Kaspi. Vol. 983. American Institute of Physics Conference Series, pp. 171–185. DOI: 10.1063/1.2900138.

Karpova, Anna V., Dmitry A. Zyuzin, and Yuriy A. Shibanov (2019). "X-ray studies of the gamma-ray pulsar J1826-1256 and its pulsar wind nebula

with Chandra and XMM-Newton." In: *MNRAS* 487.2, pp. 1964–1972. DOI: 10.1093/mnras/stz1387.

Kaspi, V. M. and A. M. Beloborodov (2017). "Magnetars." In: *ARA&A* 55, pp. 261–301. DOI: 10.1146/annurev-astro-081915-023329.

Kaspi, V. M. and D. J. Helfand (2002). "Constraining the Birth Events of Neutron Stars." In: *Neutron Stars in Supernova Remnants*. Ed. by P. O. Slane and B. M. Gaensler. Vol. 271. ASP Conf. Series, p. 3. eprint: astro-ph/0201183.

Kaspi, V. M., M. S. E. Roberts, and A. K. Harding (2006). "Isolated neutron stars." In: *Compact stellar X-ray sources*. Ed. by W. H. G. Lewin and M. van der Klis, pp. 279–339.

van Kerkwijk, M. H., R. P. Breton, and S. R. Kulkarni (2011). "Evidence for a Massive Neutron Star from a Radial-velocity Study of the Companion to the Black-widow Pulsar PSR B1957+20." In: *ApJ* 728, 95, p. 95. DOI: 10.1088/0004-637X/728/2/95.

Kewley, L. J., M. A. Dopita, R. S. Sutherland, C. A. Heisler, and J. Trevena (2001). "Theoretical Modeling of Starburst Galaxies." In: *ApJ* 556, pp. 121–140. DOI: 10.1086/321545.

Kirchhoff, G. and R. Bunsen (1860). "Chemische Analyse durch Spectralbeobachtungen." In: *Annalen der Physik* 186, pp. 161–189. DOI: 10.1002/andp.18601860602.

Klochkov, D., G. Pühlhofer, V. Suleimanov, S. Simon, K. Werner, and A. Santangelo (2013). "A non-pulsating neutron star in the supernova remnant HESS J1731-347/G353.6-0.7 with a carbon atmosphere." In: *A&A* 556, A41, A41. DOI: 10.1051/0004-6361/201321740.

Klochkov, D., V. Suleimanov, G. Pühlhofer, D. G. Yakovlev, A. Santangelo, and K. Werner (2015). "The neutron star in HESS J1731-347: Central compact objects as laboratories to study the equation of state of superdense matter." In: *A&A* 573, A53, A53. DOI: 10.1051/0004-6361/201424683.

Klochkov, D., V. Suleimanov, M. Sasaki, and A. Santangelo (2016). "Study of a new central compact object: The neutron star in the supernova remnant G15.9+0.2." In: *A&A* 592, L12, p. L12. DOI: 10.1051/0004-6361/201629208.

Kong, A. K. H. et al. (2012). "Discovery of an Unidentified Fermi Object as a Black Widow-like Millisecond Pulsar." In: *ApJ* 747, L3, p. L3. DOI: 10.1088/2041-8205/747/1/L3.

Koopmann, R. A. and J. D. P. Kenney (2004). "Hα Morphologies and Environmental Effects in Virgo Cluster Spiral Galaxies." In: *ApJ* 613, pp. 866–885. DOI: 10.1086/423191.

Kormendy, J. and L. C. Ho (2013). "Coevolution (Or Not) of Supermassive Black Holes and Host Galaxies." In: *ARA&A* 51, pp. 511–653. DOI: 10.1146/annurev-astro-082708-101811.

Koyama, K., R. Petre, E. V. Gotthelf, U. Hwang, M. Matsuura, M. Ozaki, and S. S. Holt (1995). "Evidence for shock acceleration of high-energy electrons in the supernova remnant SN1006." In: *Nature* 378.6554, pp. 255–258. DOI: 10.1038/378255a0.

Kumar, Pawan and Bing Zhang (2015). "The physics of gamma-ray bursts & relativistic jets." In: *Phys. Rep.* 561, pp. 1–109. DOI: 10.1016/j.physrep.2014.09.008.

Kunth, D., W. L. W. Sargent, and G. D. Bothun (1987). "A dwarf galaxy with Seyfert characteristics." In: *AJ* 93, pp. 29–32. DOI: 10.1086/114287.

Lai, Dong (2001). "Matter in strong magnetic fields." In: *Reviews of Modern Physics* 73, p. 629. DOI: 10.1103/RevModPhys.73.629.

Large, M. I., A. E. Vaughan, and B. Y. Mills (1968). "A Pulsar Supernova Association?" In: *Nature* 220, pp. 340–341. DOI: 10.1038/220340a0.

Larmor F.R.S. F.R.S.E D.C.L L.L.D, Joseph (1897). "On the theory of the magnetic influence on spectra; and on the radiation from moving ions." In:

The London, Edinburgh, and Dublin Philosophical Magazine and Journal of Science 44.271, pp. 503–512. DOI: 10.1080/14786449708621095.

Leahy, D. A., W. Darbro, R. F. Elsner, M. C. Weisskopf, P. G. Sutherland, S. Kahn, and J. E. Grindlay (1983). "On searches for pulsed emission with application to four globular cluster X-ray sources : NGC 1851, 6441, 6624 and 6712." In: *ApJ* 266, pp. 160–170. DOI: 10.1086/160766.

Lemons, S. M., A. E. Reines, R. M. Plotkin, E. Gallo, and J. E. Greene (2015). "An X-Ray Selected Sample of Candidate Black Holes in Dwarf Galaxies." In: *ApJ* 805, 12, p. 12. DOI: 10.1088/0004-637X/805/1/12.

Li, J., J. H. Kastner, G. Y. Prigozhin, N. S. Schulz, E. D. Feigelson, and K. V. Getman (2004). "Chandra ACIS Subpixel Event Repositioning: Further Refinements and Comparison between Backside- and Frontside-illuminated X-Ray CCDs." In: *ApJ* 610, pp. 1204–1212. DOI: 10.1086/421866.

Li, K. L., A. K. H. Kong, J. Takata, K. S. Cheng, P. H. T. Tam, C. Y. Hui, and Ruolan Jin (2014). "NuSTAR Observations and Broadband Spectral Energy Distribution Modeling of the Millisecond Pulsar Binary PSR J1023+0038." In: *ApJ* 797.2, 111, p. 111. DOI: 10.1088/0004-637X/797/2/111.

Li, X.-H., F.-J. Lu, and Z. Li (2008). "Nonthermal X-Ray Properties of Rotation-powered Pulsars and Their Wind Nebulae." In: *ApJ* 682, pp. 1166–1176. DOI: 10.1086/589495.

Liu, H.-Y., W. Yuan, X.-B. Dong, H. Zhou, and W.-J. Liu (2018). "A Uniformly Selected Sample of Low-mass Black Holes in Seyfert 1 Galaxies. II. The SDSS DR7 Sample." In: *ApJS* 235, 40, p. 40. DOI: 10.3847/1538-4365/aab88e.

Lovchinsky, I., P. Slane, B. M. Gaensler, J. P. Hughes, C.-Y. Ng, J. S. Lazendic, J. D. Gelfand, and C. L. Brogan (2011). "A Chandra Observation of Supernova Remnant G350.1-0.3 and Its Central Compact Object." In: *ApJ* 731, 70, p. 70. DOI: 10.1088/0004-637X/731/1/70.

de Luca, A. (2008). "Central Compact Objects in Supernova Remnants." In: *40 Years of Pulsars: Millisecond Pulsars, Magnetars and More*. Ed. by C. Bassa,

Z. Wang, A. Cumming, and V. M. Kaspi. Vol. 983. American Institute of Physics Conference Series, pp. 311–319. DOI: 10.1063/1.2900173.

de Luca, A. (2017). "Central compact objects in supernova remnants." In: *Journal of Physics Conference Series*. Vol. 932. Journal of Physics Conference Series, p. 012006. DOI: 10.1088/1742-6596/932/1/012006.

Luo, J., C. -Y. Ng, W. C. G. Ho, S. Bogdanov, V. M. Kaspi, and C. He (2015). "Hunting for Orphaned Central Compact Objects among Radio Pulsars." In: *ApJ* 808.2, 130, p. 130. DOI: 10.1088/0004-637X/808/2/130.

Lutz, D., D. Kunze, H. W. W. Spoon, and M. D. Thornley (1998). "Faint [O iv] emission from starburst galaxies." In: *A&A* 333, pp. L75–L78. eprint: astro-ph/9803314.

Lyne, A.G., F. Graham-Smith, and F. Graham-Smith (1990). *Pulsar Astronomy*. Cambridge Astrophysics. Cambridge University Press. ISBN: 9780521839549. URL: https://books.google.ca/books?id=AK9N3zxL4ToC.

Lyutikov, M. and F. P. Gavriil (2006). "Resonant cyclotron scattering and Comptonization in neutron star magnetospheres." In: *MNRAS* 368, pp. 690–706. DOI: 10.1111/j.1365-2966.2006.10140.x.

Manchester, R. N., G. B. Hobbs, A. Teoh, and M. Hobbs (2005). "The Australia Telescope National Facility Pulsar Catalogue." In: *AJ* 129.4, pp. 1993–2006. DOI: 10.1086/428488.

Manchester, R.N. and J.H. Taylor (1977). *Pulsars*. A Series of books in astronomy and astrophysics. W. H. Freeman. ISBN: 9780716703587. URL: https://books.google.ca/books?id=tcFlQgAACAAJ.

Manzali, A., A. de Luca, and P. A. Caraveo (2007). "Phase-resolved Spectroscopy of the Vela Pulsar with XMM-Newton." In: *ApJ* 669, pp. 570–578. DOI: 10.1086/521387.

Marshall, Herman L., Allyn Tennant, Catherine E. Grant, Adam P. Hitchcock, Stephen L. O'Dell, and Paul P. Plucinsky (2004). "Composition of the Chandra ACIS contaminant." In: *X-Ray and Gamma-Ray Instrumentation*

for Astronomy XIII. Ed. by Kathryn A. Flanagan and Oswald H. W. Siegmund. Vol. 5165. Society of Photo-Optical Instrumentation Engineers (SPIE) Conference Series, pp. 497–508. DOI: 10.1117/12.508310.

Maxwell F.R F.R.S., J. C. (1860a). "Illustrations of the dynamical theory of gases." In: *The London, Edinburgh, and Dublin Philosophical Magazine and Journal of Science* 20.130, pp. 21–37. DOI: 10.1080/14786446008642902.

Maxwell F.R F.R.S., J. C. (1860b). "Illustrations of the dynamical theory of gases.—Part I. On the motions and collisions of perfectly elastic spheres." In: *The London, Edinburgh, and Dublin Philosophical Magazine and Journal of Science* 19.124, pp. 19–32. DOI: 10.1080/14786446008642818.

Mereghetti, S., A. De Luca, P. A. Caraveo, W. Becker, R. Mignani, and G. F. Bignami (2002). "Pulse Phase Variations of the X-Ray Spectral Features in the Radio-quiet Neutron Star 1E 1207-5209." In: *ApJ* 581.2, pp. 1280–1285. DOI: 10.1086/344435.

Merloni, Andrea, Sebastian Heinz, and Tiziana di Matteo (2003). "A Fundamental Plane of black hole activity." In: *MNRAS* 345.4, pp. 1057–1076. DOI: 10.1046/j.1365-2966.2003.07017.x.

Miceli, M., S. Sciortino, E. Troja, and S. Orlando (2015). "Spatial Distribution of X-Ray Emitting Ejecta in Tycho's SNR: Indications of Shocked Tita-nium." In: *ApJ* 805, 120, p. 120. DOI: 10.1088/0004-637X/805/2/120.

Michael, E., S. Zhekov, R. McCray, U. Hwang, D. N. Burrows, S. Park, G. P. Garmire, S. S. Holt, and G. Hasinger (2002). "The X-Ray Spectrum of Supernova Remnant 1987A." In: *ApJ* 574, pp. 166–178. DOI: 10.1086/340591.

Mignani, R. P., A. de Luca, S. Zharikov, W. Hummel, W. Becker, and A. Pellizzoni (2019). "The nature of the infrared counterpart and of the optical nebula associated with the Central Compact Object in Vela Jr." In: *MNRAS*, p. 1145. DOI: 10.1093/mnras/stz1195.

von Mises, R. E. (1931). *Wahrscheinlichkeitsrechnung und ihre Anwendung in der Statistik und theoretischen Physik*. Vorlesungen aus dem Gebiete der angewandten Mathematik. Deuticke. URL: https://books.google.ca/books?id=T107OgAACAAJ.

Mori, Kaya and Wynn C. G. Ho (2007). "Modelling mid-Z element atmospheres for strongly magnetized neutron stars." In: *MNRAS* 377, pp. 905–919. DOI: 10.1111/j.1365-2966.2007.11663.x.

Morrison, R. and D. McCammon (1983). "Interstellar photoelectric absorption cross sections, 0.03-10 keV." In: *ApJ* 270, pp. 119–122. DOI: 10.1086/161102.

Moseley, H. G. J. (1913). "The high-frequency spectra of the elements." In: *The London, Edinburgh, and Dublin Philosophical Magazine and Jou-rnal of Science* 26.156, pp. 1024–1034. DOI: 10.1080/14786441308635052.

Moseley, H. G. J. (1914). "The high-frequency spectra of the elements. Part II." In: *The London, Edinburgh, and Dublin Philosophical Magazine and Journal of Science* 27.160, pp. 703–713. DOI: 10.1080/14786440408635141.

Motch, C., V. E. Zavlin, and F. Haberl (2003). "The proper motion and energy distribution of the isolated neutron star <ASTROBJ>RX J0720.4-3125</ASTROBJ>." In: *A&A* 408, pp. 323–330. DOI: 10.1051/0004-6361:20030802.

Murphy, E. J. et al. (2018). "The ngVLA Science Case and Associated Science Requirements." In: *Science with a Next Generation Very Large Array*. Ed. by E. Murphy. Vol. 517. Astronomical Society of the Pacific Conference Series, p. 3.

Ng, C. -Y., V. M. Kaspi, W. C. G. Ho, P. Weltevrede, S. Bogdanov, R. Shannon, and M. E. Gonzalez (2012). "Deep X-Ray Observations of the Young High-magnetic-field Radio Pulsar J1119-6127 and Supernova Remnant G292.2-0.5." In: *ApJ* 761.1, 65, p. 65. DOI: 10.1088/0004-637X/761/1/65.

Nyland, K. and K. Alatalo (2018). "Accreting Supermassive Black Holes in Nearby Low-Mass Galaxies." In: *Science with a Next Generation Very Large*

Array. Ed. by E. Murphy. Vol. 517. Astronomical Society of the Pacific Conference Series, p. 451.

Olausen, S. A. and V. M. Kaspi (2014). "The McGill Magnetar Catalog." In: *ApJS* 212, 6, p. 6. DOI: 10.1088/0067-0049/212/1/6.

Olausen, S. A., W. W. Zhu, J. K. Vogel, V. M. Kaspi, A. G. Lyne, C. M. Espinoza, B. W. Stappers, R. N. Manchester, and M. A. McLaughlin (2013). "X-Ray Observations of High-B Radio Pulsars." In: *ApJ* 764, 1, p. 1. DOI: 10.1088/0004-637X/764/1/1.

Ou, P.-S., Y.-H. Chu, P. Maggi, C.-J. Li, U. P. Chang, and R. A. Gruendl (2018). "X-Ray Luminosity and Size Relationship of Supernova Remnants in the LMC." In: *ApJ* 863, 137, p. 137. DOI: 10.3847/1538-4357/aad04b.

Padovani, P., D. M. Alexander, R. J. Assef, B. De Marco, P. Giommi, R. C. Hickox, G. T. Richards, V. Smolčić, E. Hatziminaoglou, and V. Mainieri (2017). "Active galactic nuclei: what's in a name?" In: *A&ARv* 25.1, 2, p. 2. DOI: 10.1007/s00159-017-0102-9.

Paerels, Frederik B. S. and Steven M. Kahn (2003). "High-Resolution X-Ray Spectroscopy with CHANDRA and XMM-NEWTON." In: *ARA&A* 41, pp. 291–342. DOI: 10.1146/annurev.astro.41.071601.165952.

Page, D., J. M. Lattimer, M. Prakash, and A. W. Steiner (2004). "Minimal Cooling of Neutron Stars: A New Paradigm." In: *ApJS* 155, pp. 623–650. DOI: 10.1086/424844.

Pan, Z., G. Hobbs, D. Li, A. Ridolfi, P. Wang, and P. Freire (2016). "Discovery of two new pulsars in 47 Tucanae (NGC 104)." In: *MNRAS* 459, pp. L26–L30. DOI: 10.1093/mnrasl/slw037.

Papitto, A. et al. (2013). "Swings between rotation and accretion power in a binary millisecond pulsar." In: *Nature* 501, pp. 517–520. DOI: 10.1038/nature12470.

Patruno, A. and A. L. Watts (2012). "Accreting Millisecond X-Ray Pulsars." In: *ArXiv e-prints*. arXiv: 1206.2727 [astro-ph.HE].

Pavlov, G. G., D. Sanwal, and M. A. Teter (2004). "Central Compact Objects in Supernova Remnants." In: *Young Neutron Stars and Their Environments*. Ed. by F. Camilo and B. M. Gaensler. Vol. 218. IAU Symposium, p. 239. eprint: astro-ph/0311526.

Pavlov, G. G., V. E. Zavlin, and D. Sanwal (2002). "Thermal Radiation from Neutron Stars: Chandra Results." In: *Neutron Stars, Pulsars, and Supernova Remnants*. Ed. by W. Becker, H. Lesch, and J. Trümper, p. 273. arXiv: astro-ph/0206024 [astro-ph].

Pavlov, G. G., V. E. Zavlin, D. Sanwal, V. Burwitz, and G. P. Garmire (2001a). "The X-Ray Spectrum of the Vela Pulsar Resolved with the Chandra X-Ray Observatory." In: *ApJ* 552, pp. L129–L133. DOI: 10.1086/320342.

Pavlov, George G., Divas Sanwal, Bülent Kızıltan, and Gordon P. Garmire (2001b). "The Compact Central Object in the RX J0852.0-4622 Supernova Remnant." In: *ApJ* 559.2, pp. L131–L134. DOI: 10.1086/323975.

Pearson, Karl (1900). "On the criterion that a given system of deviations from the probable in the case of a correlated system of variables is such that it can be reasonably supposed to have arisen from random sampling." In: *The London, Edinburgh, and Dublin Philosophical Magazine and Journal of Science* 50.302, pp. 157–175. DOI: 10.1080/14786440009463897.

Pellizzoni, A., S. Mereghetti, and A. de Luca (2002). "An Hα nebula possibly associated with the central X-ray source in the G 266.2-1.2 supernova remnant." In: *A&A* 393, pp. L65–L68. DOI: 10.1051/0004-6361:20021207.

Peterson, B. M. (1993). "Reverberation mapping of active galactic nuclei." In: *PASP* 105, pp. 247–268. DOI: 10.1086/133140.

Peterson, B. M. (2014). "Measuring the Masses of Supermassive Black Holes." In: *Space Sci. Rev.* 183, pp. 253–275. DOI: 10.1007/s11214-013-9987-4.

Peterson, B. M. et al. (2005). "Multiwavelength Monitoring of the Dwarf Seyfert 1 Galaxy NGC 4395. I. A Reverberation-based Measurement of the Black Hole Mass." In: *ApJ* 632, pp. 799–808. DOI: 10.1086/444494.

Planck, M. (1900). "Über eine Verbesserung der Wien'schen Spectralgleichung." In: pp. 202–204. URL: https://books.google.ca/books?id=yDfCnQEACAAJ.

Planck, M. and M. Masius (1914). *The Theory of Heat Radiation*. Blakiston. URL: https://books.google.ca/books?id=2PR%5C_AAAAMAAJ.

Plotkin, R. M. and A. E. Reines (2018). "Science with an ngVLA: Local Constraints on Supermassive Black Hole Seeds." In: *arXiv e-prints*. arXiv: 1810.06814 [astro-ph.HE].

Plucinsky, P. P., A. P. Beardmore, A. Foster, F. Haberl, E. D. Miller, A. M. T. Pollock, and S. Sembay (2017). "SNR 1E 0102.2-7219 as an X-ray calibration standard in the 0.5-1.0 keV bandpass and its application to the CCD instruments aboard Chandra, Suzaku, Swift and XMM-Newton." In: *A&A* 597, A35, A35. DOI: 10.1051/0004-6361/201628824.

Poisson, S.D. (1837). *Recherches sur la probabilité des jugements en matière criminelle et en matière civile: précédées des règles générales du calcul des probabilités*. Bachelier. URL: https://books.google.ca/books?id=uovoFE3gt2EC.

Potekhin, A. Y., G. Chabrier, and W. C. G. Ho (2014). "Opacities and spectra of hydrogen atmospheres of moderately magnetized neutron stars." In: *A&A* 572, A69, A69. DOI: 10.1051/0004-6361/201424619.

Radhakrishnan, V. and D. J. Cooke (1969). "Magnetic Poles and the Polarization Structure of Pulsar Radiation." In: *Astrophys. Lett.* 3, p. 225.

Rea, N., A. Borghese, P. Esposito, F. Coti Zelati, M. Bachetti, G. L. Israel, and A. de Luca (2016). "Magnetar-like Activity from the Central Compact Object in the SNR RCW103." In: *ApJ* 828, L13, p. L13. DOI: 10.3847/2041-8205/828/1/L13.

Rea, N. et al. (2013). "The Outburst Decay of the Low Magnetic Field Magnetar SGR 0418+5729." In: *ApJ* 770, 65, p. 65. DOI: 10.1088/0004-637X/770/1/65.

Reines, A. E. and A. T. Deller (2012). "Parsec-scale Radio Emission from the Low-luminosity Active Galactic Nucleus in the Dwarf Starburst Galaxy Henize 2-10." In: *ApJ* 750, L24, p. L24. DOI: 10.1088/2041-8205/750/1/L24.

Reines, A. E., J. E. Greene, and M. Geha (2013). "Dwarf Galaxies with Optical Signatures of Active Massive Black Holes." In: *ApJ* 775, 116, p. 116. DOI: 10.1088/0004-637X/775/2/116.

Reines, A. E., M. T. Reynolds, J. M. Miller, G. R. Sivakoff, J. E. Greene, R. C. Hickox, and K. E. Johnson (2016). "Deep Chandra Observations of the Compact Starburst Galaxy Henize 2-10: X-Rays from the Massive Black Hole." In: *ApJ* 830, L35, p. L35. DOI: 10.3847/2041-8205/830/2/L35.

Reines, A. E., G. R. Sivakoff, K. E. Johnson, and C. L. Brogan (2011). "An actively accreting massive black hole in the dwarf starburst galaxy Henize2-10." In: *Nature* 470, pp. 66–68. DOI: 10.1038/nature09724.

Reynolds, S. P., K. J. Borkowski, U. Hwang, I. Harrus, R. Petre, and G. Dubner (2006). "A New Young Galactic Supernova Remnant Containing a Compact Object: G15.9+0.2." In: *ApJ* 652, pp. L45–L48. DOI: 10.1086/510066.

Ridolfi, A. et al. (2016). "Long-term observations of the pulsars in 47 Tucanae - I. A study of four elusive binary systems." In: *MNRAS* 462, pp. 2918–2933. DOI: 10.1093/mnras/stw1850.

Roberts, M. S. E. (2011). "New Black Widows and Redbacks in the Galactic Field." In: *American Institute of Physics Conference Series*. Ed. by M. Burgay, N. D'Amico, P. Esposito, A. Pellizzoni, and A. Possenti. Vol. 1357. American Institute of Physics Conference Series, pp. 127–130. DOI: 10.1063/1.3615095.

Roberts, M. S. E. (2013). "Surrounded by spiders! New black widows and redbacks in the Galactic field." In: *Neutron Stars and Pulsars: Challenges and Opportunities after 80 years*. Ed. by J. van Leeuwen. Vol. 291. IAU Symposium, pp. 127–132. DOI: 10.1017/S174392131202337X.

Romani, R. W. and M. S. Shaw (2011). "The Orbit and Companion of Probable γ-Ray Pulsar J2339-0533." In: *ApJ* 743, L26, p. L26. DOI: 10.1088/2041-8205/743/2/L26.

Romani, Roger W. (1987). "Model Atmospheres for Cooling Neutron Stars." In: *ApJ* 313, p. 718. DOI: 10.1086/165010.

Romani, Roger W. and Nicolas Sanchez (2016). "Intra-binary Shock Heating of Black Widow Companions." In: *ApJ* 828.1, 7, p. 7. DOI: 10.3847/0004-637X/828/1/7.

Roy, J. et al. (2015). "Discovery of Psr J1227-4853: A Transition from a Low-mass X-Ray Binary to a Redback Millisecond Pulsar." In: *ApJ* 800, L12, p. L12. DOI: 10.1088/2041-8205/800/1/L12.

Ruderman, M. A. and P. G. Sutherland (1975). "Theory of pulsars - Polar caps, sparks, and coherent microwave radiation." In: *ApJ* 196, pp. 51–72. DOI: 10.1086/153393.

Russell, Stephen C. and Michael A. Dopita (1992). "Abundances of the Heavy Elements in the Magellanic Clouds. III. Interpretation of Results." In: *ApJ* 384, p. 508. DOI: 10.1086/170893.

Rybicki, George B. and Alan P. Lightman (1986). *Radiative Processes in Astrophysics*. A Wiley-Interscience publication. Wiley. ISBN: 9780471827597.

Sanchez, Nicolas and Roger W. Romani (2017). "B-ducted Heating of Black Widow Companions." In: *ApJ* 845.1, 42, p. 42. DOI: 10.3847/1538-4357/aa7a02.

Santangelo, A. and R. Madonia (2014). "Fifty years of X-ray astronomy: A look back and into the (near) future." In: *Astroparticle Physics* 53, pp. 130–151. DOI: 10.1016/j.astropartphys.2013.11.005.

Sanwal, D., G. G. Pavlov, V. E. Zavlin, and M. A. Teter (2002). "Discovery of Absorption Features in the X-Ray Spectrum of an Isolated Neutron Star." In: *ApJ* 574.1, pp. L61–L64. DOI: 10.1086/342368.

Satyapal, S., T. Böker, W. Mcalpine, M. Gliozzi, N. P. Abel, and T. Heckman (2009). "The Incidence of Active Galactic Nuclei in Pure Disk Galaxies: The Spitzer View." In: *ApJ* 704, pp. 439–452. DOI: 10.1088/0004-637X/704/1/439.

Satyapal, S., N. J. Secrest, W. McAlpine, S. L. Ellison, J. Fischer, and J. L. Rosenberg (2014). "Discovery of a Population of Bulgeless Galaxies with Extremely Red Mid-IR Colors: Obscured AGN Activity in the Low-mass Regime?" In: *ApJ* 784, 113, p. 113. DOI: 10.1088/0004-637X/784/2/113.

Schaerer, D. and G. Stasińska (1999). "On the origin of [O iv] emission in Wolf-Rayet galaxies." In: *A&A* 345, pp. L17–L21. eprint: astro-ph/9903430.

Secrest, N. J., S. Satyapal, M. Gliozzi, C. C. Cheung, A. C. Seth, and T. Böker (2012). "The Chandra View of NGC 4178: The Lowest Mass Black Hole in a Bulgeless Disk Galaxy?" In: *ApJ* 753, 38, p. 38. DOI: 10.1088/0004-637X/753/1/38.

Secrest, N. J., S. Satyapal, S. M. Moran, C. C. Cheung, M. Giroletti, M. Gliozzi, M. P. Bergmann, and A. C. Seth (2013). "A Multi-wavelength Analysis of NGC 4178: A Bulgeless Galaxy with an Active Galactic Nucleus." In: *ApJ* 777, 139, p. 139. DOI: 10.1088/0004-637X/777/2/139.

Seitenzahl, Ivo R., Frédéric P. A. Vogt, Jason P. Terry, Parviz Ghavamian, Michael A. Dopita, Ashley J. Ruiter, and Tuguldur Sukhbold (2018). "Integral Field Spectroscopy of Supernova Remnant 1E0102-7219 Reveals Fast-moving Hydrogen and Sulfur-rich Ejecta." In: *ApJ* 853, L32, p. L32. DOI: 10.3847/2041-8213/aaa958.

Seward, F. D. and M. Mitchell (1981). "X-ray survey of the Small Magellanic Cloud." In: *ApJ* 243, pp. 736–743. DOI: 10.1086/158641.

Smith, R. K. and J. P. Hughes (2010). "Ionization Equilibrium Timescales in Collisional Plasmas." In: *ApJ* 718, pp. 583–585. DOI: 10.1088/0004-637X/718/1/583.

Songsheng, Y.-Y. and J.-M. Wang (2018). "Measuring black hole mass of type I active galactic nuclei by spectropolarimetry." In: *MNRAS* 473, pp. L1–L5. DOI: 10.1093/mnrasl/slx154.

Staelin, D. H. and E. C. Reifenstein III (1968). "Pulsating Radio Sources near the Crab Nebula." In: *Science* 162, pp. 1481–1483. DOI: 10.1126/science.162.3861.1481.

Stappers, B. W. et al. (2014). "A State Change in the Missing Link Binary Pulsar System PSR J1023+0038." In: *ApJ* 790, 39, p. 39. DOI: 10.1088/0004-637X/790/1/39.

Stern, D. et al. (2012). "Mid-infrared Selection of Active Galactic Nuclei with the Wide-Field Infrared Survey Explorer. I. Characterizing WISE-selected Active Galactic Nuclei in COSMOS." In: *ApJ* 753, 30, p. 30. DOI: 10.1088/0004-637X/753/1/30.

Sukhbold, Tuguldur, T. Ertl, S. E. Woosley, Justin M. Brown, and H. -T. Janka (2016). "Core-collapse Supernovae from 9 to 120 Solar Masses Based on Neutrino-powered Explosions." In: *ApJ* 821.1, 38, p. 38. DOI: 10.3847/0004-637X/821/1/38.

Suleimanov, V. F., D. Klochkov, G. G. Pavlov, and K. Werner (2014). "Carbon Neutron Star Atmospheres." In: *ApJS* 210, 13, p. 13. DOI: 10.1088/0067-0049/210/1/13.

Tamagawa, T. et al. (2009). "Suzaku Observations of Tycho's Supernova Remnant." In: *PASJ* 61, S167–S174. DOI: 10.1093/pasj/61.sp1.S167.

Tendulkar, S. P. et al. (2014). "NuSTAR Observations of the State Transition of Millisecond Pulsar Binary PSR J1023+0038." In: *ApJ* 791, 77, p. 77. DOI: 10.1088/0004-637X/791/2/77.

Terlevich, Roberto, Guillermo Tenorio-Tagle, Jose Franco, and Jorge Melnick (1992). "The starburst model for active galactic nuclei - The broad-line region as supernova remnants evolving in a high-density medium." In: *MNRAS* 255, pp. 713–728. DOI: 10.1093/mnras/255.4.713.

The Chandra Proposers' Observatory Guide (2018). URL: http://cxc.harvard.edu/proposer/POG/pdf/MPOG.pdf.

The Lynx Team (2018). "The Lynx Mission Concept Study Interim Report." In: *arXiv e-prints*, arXiv:1809.09642, arXiv:1809.09642. arXiv: 1809.09642 [astro-ph.IM].

Thompson, C. and R. C. Duncan (1995). "The soft gamma repeaters as very strongly magnetized neutron stars - I. Radiative mechanism for out-bursts." In: *MNRAS* 275, pp. 255–300. DOI: 10.1093/mnras/275.2.255.

Thompson, C. and R. C. Duncan (1996). "The Soft Gamma Repeaters as Very Strongly Magnetized Neutron Stars. II. Quiescent Neutrino, X-Ray, and Alfven Wave Emission." In: *ApJ* 473, p. 322. DOI: 10.1086/178147.

Thomson O. M P.R.S, J. J. (1881). "On the electric and magnetic effects produced by the motion of electrified bodies." In: *The London, Edinburgh, and Dublin Philosophical Magazine and Journal of Science* 11.68, pp. 229–249. DOI: 10.1080/14786448108627008.

Thornton, C. E., A. J. Barth, L. C. Ho, R. E. Rutledge, and J. E. Greene (2008). "The Host Galaxy and Central Engine of the Dwarf Active Galactic Nucleus POX 52." In: *ApJ* 686, pp. 892–910. DOI: 10.1086/591519.

Torii, K., H. Uchida, K. Hasuike, H. Tsunemi, Y. Yamaguchi, and S. Shibata (2006). "Discovery of a Featureless X-Ray Spectrum in the Supernova Remnant Shell of G330.2+1.0." In: *PASJ* 58, pp. L11–L14. DOI: 10.1093/pasj/58.1.L11.

Tully, R. B. and E. J. Shaya (1984). "Infall of galaxies into the Virgo cluster and some cosmological constraints." In: *ApJ* 281, pp. 31–55. DOI: 10.1086/162073.

Tuohy, I. R. and M. A. Dopita (1983). "Ring ejection in type II supernovae : 1E 0102.2-7219 in the Small Magellanic Cloud." In: *ApJ* 268, pp. L11–L15. DOI: 10.1086/184020.

Ulvestad, J. S., K. E. Johnson, and S. G. Neff (2007). "A VLBI Search for Radio Supernovae in Wolf-Rayet Galaxies." In: *AJ* 133, pp. 1868–1873. DOI: 10.1086/512190.

Vacca, William D. and Peter S. Conti (1992). "Optical Spectrophotometry of Wolf-Rayet Galaxies." In: *ApJ* 401, p. 543. DOI: 10.1086/172085.

Verner, D. A., G. J. Ferland, K. T. Korista, and D. G. Yakovlev (1996). "Atomic Data for Astrophysics. II. New Analytic FITS for Photoionization Cross Sections of Atoms and Ions." In: *ApJ* 465, p. 487. DOI: 10.1086/177435.

Viganò, D. and J. A. Pons (2012). "Central compact objects and the hidden magnetic field scenario." In: *MNRAS* 425, pp. 2487–2492. DOI: 10.1111/j.1365-2966.2012.21679.x.

Viganò, D., N. Rea, J. A. Pons, R. Perna, D. N. Aguilera, and J. A. Miralles (2013). "Unifying the observational diversity of isolated neutron stars via magneto-thermal evolution models." In: *MNRAS* 434.1, pp. 123–141. DOI: 10.1093/mnras/stt1008.

Vogt, F. P. A., E. S. Bartlett, I. R. Seitenzahl, M. A. Dopita, P. Ghavamian, A. J. Ruiter, and J. P. Terry (2018). "Identification of the central compact object in the young supernova remnant 1E 0102.2-7219." In: *Nature Astronomy* 2, pp. 465–471. DOI: 10.1038/s41550-018-0433-0.

Volonteri, M. and P. Natarajan (2009). "Journey to the M_{BH}-σ relation: the fate of low-mass black holes in the Universe." In: *MNRAS* 400, pp. 1911–1918. DOI: 10.1111/j.1365-2966.2009.15577.x.

Wadiasingh, Zorawar, Christo Venter, Alice K. Harding, Markus Böttcher, and Patrick Kilian (2018). "Pressure Balance and Intrabinary Shock Stability in Rotation-powered-state Redback and Transitional Millisecond Pulsar Binary Systems." In: *ApJ* 869.2, 120, p. 120. DOI: 10.3847/1538-4357/aaed43.

Walter, R. et al. (2003). "INTEGRAL discovery of a bright highly obscured galactic X-ray binary source IGR J16318-4848." In: *A&A* 411, pp. L427–L432. DOI: 10.1051/0004-6361:20031369.

Weisskopf, Martin C., Harvey D. Tananbaum, Leon P. Van Speybroeck, and Stephen L. O'Dell (2000). "Chandra X-ray Observatory (CXO): overview." In: *X-Ray Optics, Instruments, and Missions III*. Ed. by Joachim E. Truemper and Bernd Aschenbach. Vol. 4012. Society of Photo-Optical Instrumentation Engineers (SPIE) Conference Series, pp. 2–16. DOI: 10.1117/12.391545.

Wien, Willy (1897). "On the division of energy in the emission-spectrum of a black body." In: *The London, Edinburgh, and Dublin Philosophical Magazine and Journal of Science* 43.262, pp. 214–220. DOI: 10.1080/14786449708620983.

Wijnands, R. and M. van der Klis (1998). "A millisecond pulsar in an X-ray binary system." In: *Nature* 394, pp. 344–346. DOI: 10.1038/28557.

Wijngaarden, M. J. P., Wynn C. G. Ho, Philip Chang, Craig O. Heinke, Dany Page, Mikhail Beznogov, and Daniel J. Patnaude (2019). "Diffusive nuclear burning in cooling simulations and application to new temperature data of the Cassiopeia A neutron star." In: *MNRAS* 484.1, pp. 974–988. DOI: 10.1093/mnras/stz042.

Williams, Brian J., John W. Hewitt, Robert Petre, and Tea Temim (2018). "A Deep X-Ray View of the Synchrotron-dominated Supernova Remnant G330.2+1.0." In: *ApJ* 855.2, 118, p. 118. DOI: 10.3847/1538-4357/aaadb6.

Willingale, R., J. A. M. Bleeker, K. J. van der Heyden, J. S. Kaastra, and J. Vink (2002). "X-ray spectral imaging and Doppler mapping of Cassiopeia A." In: *A&A* 381, pp. 1039–1048. DOI: 10.1051/0004-6361:20011614.

Wilms, J., A. Allen, and R. McCray (2000). "On the Absorption of X-Rays in the Interstellar Medium." In: *ApJ* 542, pp. 914–924. DOI: 10.1086/317016.

Woods, P. M. and C. Thompson (2006). "Soft gamma repeaters and anomalous X-ray pulsars: magnetar candidates." In: *Compact stellar X-ray sources*, pp. 547–586.

Xiao, T., A. J. Barth, J. E. Greene, L. C. Ho, M. C. Bentz, R. R. Ludwig, and Y. Jiang (2011). "Exploring the Low-mass End of the M_{BH} - σ_* Relation

with Active Galaxies." In: *ApJ* 739, 28, p. 28. DOI: 10.1088/0004-637X/739/1/28.

Zavlin, V. E. (2007). "First X-Ray Observations of the Young Pulsar J1357-6429." In: *ApJ* 665, pp. L143–L146. DOI: 10.1086/521300.

Zavlin, V. E., G. G. Pavlov, D. Sanwal, R. N. Manchester, J. Trümper, J. P. Halpern, and W. Becker (2002). "X-Radiation from the Millisecond Pulsar J0437-4715." In: *ApJ* 569, pp. 894–902. DOI: 10.1086/339351.